

911

Measuring Cosmic Microwave Background Radiation Anisotropy on Medium Angular Scales

by

Jason L. Puchalla

B.A., Hamline University (1987)

Submitted to the Department of Physics
partial fulfillment of the requirements for the degree of

Doctor of Philosophy

at the

MASSACHUSETTS INSTITUTE OF TECHNOLOGY

February 1995

©Massachusetts Institute of Technology 1995

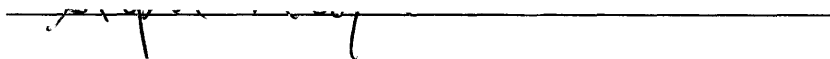
Signature of Author



Department of Physics

April 5, 1995

Certified by



Stephan Meyer

Associate Professor of Astrophysics at the University of Chicago

Thesis Supervisor

Accepted by



MASSACHUSETTS INSTITUTE
OF TECHNOLOGY

JUN 26 1995

George Koster
Chairman, Department Committee

LIBRARIAN

Measuring Cosmic Microwave Background Radiation Anisotropy on Medium Angular Scales

by

Jason L. Puchalla

Submitted to the Department of Physics
in March of 1995 in partial fulfillment of the requirements for the degree of
Doctor of Philosophy

Abstract

The Medium Scale Anisotropy Measurement flown in June of 1992 (MSAM I (1992)) is a balloon-borne, off-axis telescope designed to measure fluctuations in the Microwave Background Radiation (MBR) at 5.6, 9, 16.5, and 22.5 cm^{-1} . The telescope beam width is approximately 0.5° as measured in flight. Analysis of the 4.7 hours of sky observation near the North Celestial Pole shows statistically significant fluctuations in the MBR at the 0.5° angular scale. Using a Gaussian autocorrelation function analysis, the double difference demodulation is most sensitive at $\theta_c = 0.3^\circ$ and the single difference demodulation at $\theta_c = 0.5^\circ$. At these angles, the 90% single difference confidence interval is $1.8 \times 10^{-5} < \Delta T/T < 4.2 \times 10^{-5}$. For the double difference data, the interval at the most sensitive angle is $1.8 \times 10^{-5} < \Delta T/T < 3.5 \times 10^{-5}$. Much of the signal is due to two prominent regions of the sky binned data which are spectrally consistent with small but extended ($3' < \theta_{\text{diam}} < 20'$) MBR sources. They are not correlated with known foreground sources.

Thesis Supervisor: Stephan S. Meyer

Title: Associate Professor of Astronomy and Astrophysics at the University of Chicago

Acknowledgements

Like too many other physicists, I came to graduate school with the thought of researching particle physics. Fortunately, I instead met up with my advisor, Steve Meyer, while I was a TA for Junior Lab. I am grateful to Steve both for having introduced me to experimental cosmology as well as for sharing his insight into physics, computers and engineering (and, of course, for teaching me that knot that is so incredibly useful for packing trucks).

This project is, by design, a team effort. Each of these people has expended *alot* of effort, both at their respective institutions and in Palestine, Tx. As such, I would like to thank (in no particular order) the masses that have worked, suffered, and succeeded with this experiment: Ed (Hotel) Cheng, Dave (I'm sure DC knows) Cottingham, Dale ("can't it be lighter?") Fixsen, Walter (Camac) Folz, Casey (Pete's) Inman, Jeff ("time to lift?!") Jewell, Matt (useful plot) Kowitt, Steve ("the thing is...") Meyer, Lyman (gotta' keep working) Page, John (Gimmecap) Ruhl, and Bob (Gondola) Silverberg. A gold star to Casey for enduring with me the days of misery in the underheated GSFC high bay and for sharing her ever-expanding musical library of CD's. Much of the work on the "source-like features" is courtesy of Matt and Casey.

While in Boston, I was fortunate to run across a few special people. Thanks to: Betsy Baker for both her patience and lack of patience; Peggy Berkovitz in the graduate physics office and Susan Merullo in the Gravity Group for being immeasurably helpful and competent (unusual breaths of fresh air in the MIT bureaucracy); Bill Barnes for our bonding experience at MIT in the room without windows – memories are enough ... let's not do it again; and Julio Arrecis for both the fun and commiseration.

I also have had the fortune to spend time at the University of Chicago and enjoy the company of fellow students/post-docs/professors too numerous to name. Thanks to Lloyd Knox for theoretical cosmology tutorials and Arthur Kosowsky for calculating the MSAM window functions. Special thanks to Suzanne Staggs for being there in the 11th hour, thesis editing beyond the call of duty, and helping me to double the number of movies I've seen during my life. And, of course, thanks to my mom who has offered nothing but encouragement throughout the years.

This work, and my rent payments, were made possible by a NASA GSRP fellowship of which I was a recipient for the past three years. The National Scientific Balloon Facility also deserves praise for their assistance and, as DC phrased it, "can-do" spirit.

Contents

1	Introduction to the Standard Model and the Medium Scale Anisotropy Measurement	11
1.1	CMBR in the Standard Model	11
1.2	Current Microwave Background Radiation (MBR) Anisotropy Measurements	16
1.3	Overview of Thesis	16
2	The MSAM I (1992) Instrument	19
2.1	Introduction and Overview	19
2.2	Optics	21
2.2.1	Alignment	23
2.2.2	Detectors	25
2.2.3	Gondola	27
2.3	Electronics and Telemetry	30
3	Flight Characteristics	31
3.1	Introduction	31
3.2	Observation Scheme	31
3.3	Pointing	32
3.4	Planet Rasters and the Antenna Response	35
3.5	Systematic Error Sources	38
3.5.1	Sidelobe Response	38
3.5.2	Atmosphere	40
3.5.3	Other Sources of Spurious Signal	43
4	Data Analysis	48
4.1	Overview of Technique	48
4.2	The Transfer Function and Deglitching	48
4.3	Demodulation and Calibration	56
4.3.1	Noise Estimates	58
4.3.2	Gain Drift	59

4.4	Dealing with Other Systematic Systematic Error Sources	61
4.5	Binning of Data	61
4.6	Sensitivity	63
4.7	Quadrature Data	66
4.7.1	Expected Foreground Sources	66
4.8	Spectral Modeling	72
4.8.1	Dust Component	73
4.8.2	MBR Component	75
4.9	MBR Fluctuation Limits	75
4.10	Summary	80
5	Discussion of Results	81
5.1	MBR Source-like Features	81
5.2	Additional Observations and Recent Results	83
5.3	Summary and Future Plans	86
A	Conversion of MSAM's Demodulated Signal to a Rayleigh-Jeans Temperature Difference	87
A.1	Preliminaries	87
A.2	Ideal Demodulation	88
A.2.1	Assumptions	88
A.2.2	Demodulated Signal	89
A.3	Software Demodulation	90
A.4	Formulae for Temperature Conversion	92
B	1992 Flight Timeline	93
C	Flight Statistics for MSAM I 1992	98
D	Correlation Coefficients for MSAM I Sensors	99

List of Figures

1-1	Various eras in the history of the early universe. Borrowed from “The Early Universe” by G. Borner (1988)	12
1-2	Schematic of the radiation power spectrum in the Standard Model showing the contributions from the Sachs-Wolfe effect and acoustic oscillations (adapted from Hu and Sugiyama 1994). The spherical harmonic moment l represents the angular size on the size today where $l \sim 60/\theta_{degrees}$. The y-axis represents the amplitude of MBR temperature fluctuations. The largest peak is known as the first Doppler peak and is located near $l = 200$	15
1-3	Measured anisotropy for 12 experiments. The best-fitting amplitude Q_{flat} of a flat power spectrum quoted at the quadrupole. The vertical error bars are 2σ confidence intervals. Modified from D. Scott astro-ph 9502011.	17
2-1	The MSAM I (1992) gondola.	22
2-2	The normalized spectral responses to a 1000 K black body source. The harmonics are due to reflections in the measurement setup.	26
2-3	The dewar beam response approximately 45 inches from the front of the Winston cone. These profiles indicate the response over the plane which approximates the location of the secondary mirror surface. . . .	28
2-4	The refrigerator which houses the detectors and optics for MSAM I (1992). The detectors are mounted on the 300 mK ID.	29
3-1	33
3-2	The pointing achieved during MBR observations is demonstrated by the width of the line. Hours of RA are shown on the diagonals. The gap represents when MSAM I (1992) stopped to observe the Coma Cluster. The diagonals are RA hours. The squiggle is a commanding problem which lasted a few minutes.	34
3-3	The double difference antenna pattern measured from the rasters over Jupiter. Those made from Saturn are similar but have 1/5 the signal to noise.	35

3-4	The single difference antenna pattern measured from the rasters over Jupiter. Those made from Saturn are similar but have 1/5 the signal to noise.	36
3-5	The sensitivity of the single (W2) and double (W3) difference demodulations as a function of multipole moment l	37
3-6	During the 1994 Palestine campaign, we used a source nicknamed Gim-mecap to map the sidelobe response of MSAM I (1994) which has a new top configuration. The chopped MSAM AZ (azimuth) scan provides a <i>best case</i> scenario for the MSAM I 1992 design. The other data are not directly comparable to the MSAM I 1992 gondola.	41
3-7	Pressure variations throughout the MBR observations. A pressure of 3 mm corresponds to an altitude of ~ 35 km. The approximate conversion is $\text{Altitude} = -\text{Pres}/1.292 + 37.70$. Porpoising started well before reaching float. The vertical lines are telemetry dropouts. . . .	44
4-1	A linear plot of the modulus of the channel 2 model transfer function.	50
4-2	The glitch modeling results for a particular example. The residuals are at the approximately 10 percent level.	51
4-3	The global chopped offsets for the first half of the flight for each channel and referred to electronic gain 1. Each sample is a 1/8 second integration of a detector. Chopper cycle sample 0 is the integration for the first 1/8 second of the center position of the chopper cycle. The last four samples correspond to when the chopper has thrown the beam to the telescope's left.	53
4-4	Histograms of predemodulated data for each of the four channels. Line represents the best fit Gaussian.	54
4-5	Residuals of the Gaussian fit to the histograms of the predemodulated data for each of the four channels.	55
4-6	The lockin waveforms used for demodulation of the time stream. The vector comprised of the 16 samples of a detector in a chopper cycle (i.e. the average signal template) is dotted into the above waveforms to obtain the double and single difference demodulated data as well as the same in the quadrature phase.	57
4-7	The Pearson correlation coefficients for the demodulated data BEFORE drift removal.	58
4-8	Autocorrelation vectors for the four channels as a function of sample lag.	60
4-9	The Pearson correlation coefficients for the demodulated data AFTER drift removal.	62
4-10	The MSAM I (1992) single difference data binned in sky coordinates but smoothed and plotted in RA. Channel 1 (5.6cm^{-1}) is plotted first followed by the other channels. The y-axis is in units of Rayleigh-Jeans temperatures.	64

4-11	The MSAM I (1992) double difference data binned in sky coordinates but smoothed and plotted in RA . Channel 1 (5.6cm^{-1}) is plotted first followed by the other channels. The y-axis is in units of Rayleigh-Jeans temperatures.	65
4-12	The MSAM I (1992) single difference quadrature data binned in sky coordinates but smoothed and plotted in RA . Channel 1 (5.6cm^{-1}) is plotted first followed by the other channels. The y-axis is in units of Rayleigh-Jeans temperatures.	67
4-13	The MSAM I (1992) double difference quadrature data binned in sky coordinates but smoothed and plotted in RA . Channel 1 (5.6cm^{-1}) is plotted first followed by the other channels. The y-axis is in units of Rayleigh-Jeans temperatures.	68
4-14	The MSAM I (1992) single difference quadrature data shifted by 15 degrees binned in sky coordinates but smoothed and plotted in RA . Channel 1 (5.6cm^{-1}) is plotted first followed by the other channels. The y-axis is in units of Rayleigh-Jeans temperatures.	69
4-15	The MSAM I (1992) double difference quadrature data shifted by 15 degrees binned in sky coordinates but smoothed and plotted in RA . Channel 1 (5.6cm^{-1}) is plotted first followed by the other channels. The y-axis is in units of Rayleigh-Jeans temperatures.	70
4-16	Comparison of differential Planckian spectra (solid) to that of expected foreground sources. The boxes denote the radiometer bands of COBE/DMR , FIRS and MSAM I, MSAM II (the MSAM I (1992) gondola with a different radiometer), and TopHAT (a proposed Antarctic long duration balloon experiment).	71
4-17	The dust component in terms of optical depth D_k referred to 22.5 cm^{-1} . Data has been smoothed for this plot. The IRAS 100 micron data convolved with our beam pattern is superimposed. (a) Double Difference (b) Single Difference.	74
4-18	The MBR spectral component t_k smoothed and plotted in RA: (a) Double Difference (b) Single Difference. The beam pattern is also overplotted for scale.	76
4-19	Upper and lower bounds for a Gaussian auto correlation function (GACF) model as a function of the correlation angle θ_c for the entire flight. Shown are the 95% confidence upper and lower limits for double difference (solid) and single difference (dashed).	79
5-1	The sky fields associated with MSAM15+82 and MSAM19+82 in regressed to 1950 coordinates. The size of the symbol is proportional to its flux.	82
5-2	The measure flux density for MSAM15+82 at 5.6, 9.0, and 16.5cm^{-1} . Overplotted are four best fit models.	84

5-3 The measure flux density for MSAM19+82 at 5.6, 9.0, and 16.5cm⁻¹.
Overplotted are four best fit models. 85

List of Tables

1.1	Contributing factors to $\Delta T/T$ CMBR anisotropy.	13
2.1	Beam Sizes for MSAM I 1992	23
2.2	Radiometer Characteristics	25
3.1	Summary of Constant Chopped Offset	38
3.2	Summary of Variable Offset in Sky Binned Data	39
3.3	Results of Page atmospheric modeling using a computer model developed by Weiss (1979). The bandpass integrals for each channel are shown for an altitude of 35 Km and observing angle of 45° from zenith.	42
3.4	Zenith sky brightness at 29 Km	43
3.5	Power estimates (unchopped) from gondola top structure and beam spillover at secondary.	46
4.1	Summary of the flight-averaged constant chopped offsets (in mK) removed for channels 1-4 (c1,...,c4).	52
4.2	Characteristics of MSAM I (1992) calibration sources at the time of flight.	56
4.3	Sky Sensitivities ($\mu\text{Ksec}^{1/2}$)	66
4.4	Upper and lower bounds on MBR component anisotropy. Bounds are also placed on the isolated source-like regions.	78
5.1	χ^2 for the isolated source-like regions MSAM15+82 and MSAM19+82 before and after removal of a best fit PSF.	83

Chapter 1

Introduction to the Standard Model and the Medium Scale Anisotropy Measurement

1.1 CMBR in the Standard Model

It is possible to reconstruct a plausible sequence of events in the early universe with the expansion of the universe, described by a time dependent scale factor $R(t)$, as the principle assumption. This predicts an earlier time where the universe was significantly hotter and comprised of particles stable at high energy. Figure 1-1 represents the standard model timeline.

In its early stages, the universe existed in a radiation-dominated phase described by the scale factor $R \sim t^{\frac{1}{2}}$. About 500,000 years after the era of nucleosynthesis ($T \sim 4000 K$), a transition occurred where the matter energy density became the dominant factor and $R \sim t^{\frac{2}{3}}$.

Near a redshift of $z \sim 1100$ (perhaps a few hundred thousand years later), the continuing expansion reduced the temperature to around 3000 K ($\sim 0.3 \text{ eV}^1$). Photon collisional energies were insufficient to cause ionization. Charged particles combined to form neutral atoms and the photonic mean free path increased to horizon scales² decoupling the photons from matter. This era is known as *recombination* (this termi-

¹The large ratio of photons to matter causes this temperature to be less than 13.6 eV.

²Loosely speaking, the size of causally connected regions of space is known as the horizon size. The angular extent of causally connected regions at the time of recombination is $\sim 1^\circ$.

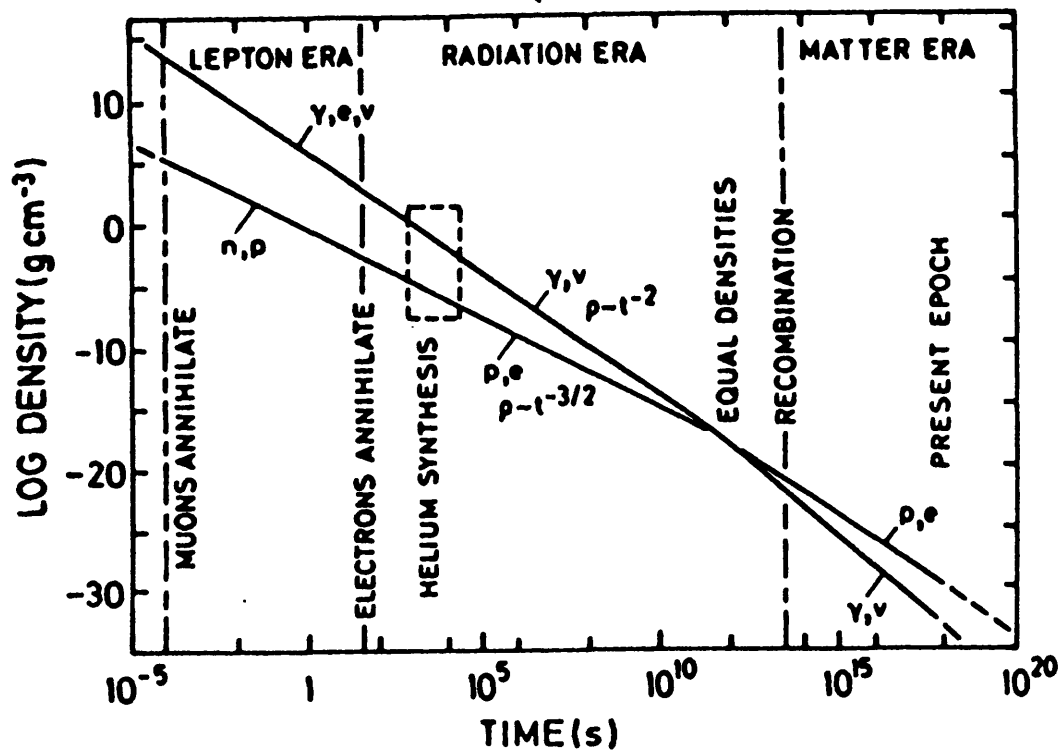


Figure 1-1: Various eras in the history of the early universe. Borrowed from "The Early Universe" by G. Borner (1988)

nology makes sense if one runs the events backwards in time). The duration of this epoch is approximately $\Delta z = 80$ with little dependence on the density parameters Ω_o and Ω_B or the Hubble parameter H_o . These photons are what make up the Cosmic Microwave Background Radiation (CMBR) today. Since the expansion continued for billions of years, the temperature of the this radiation field today is much smaller.

The CMBR is characterized through the frequency spectrum, polarization, and spatial distribution. Measurements by the Far InfraRed Absolute Spectrometer (FIRAS) have shown that the radiation is consistent with a blackbody emitter at $T=2.726$ K [32]. Measurements of spectral distortions provide insights into the nature of early structure-forming events. These events can also effect the isotropy of the CMBR by smoothing deviations which may have existed at the time of recombination. Polarization effects are predicted to be small; none have been detected to date. The spatial distribution, however, is now being characterized by several experiments.

There are several contributions to consider when measuring spatial fluctuations. Roughly in order of importance [54] :

Table 1.1: Contributing factors to $\Delta T/T$ CMBR anisotropy.

Source Description
dipole anisotropy; V_{\odot} is Sun motion relative to CMBR
gravitational potential (Sachs-Wolfe)
perturbation from adiabatic fluctuations
perturbation from isocurvature fluctuations
Doppler shifts at time of last scattering
Sunyaev-Zel'dovich fluctuations (inverse Compton scattering)

The dipole moment was the first measured deviation from isotropy. A possible explanation for most or all of the dipole is the motion of our Sun with respect to the CMBR radiation. An observer in motion through a radiation field will measure an angular temperature dependence given by

$$T_{\text{obs}}(\theta) = \frac{T_{\text{rest}}(1 - \beta^2)^{1/2}}{1 - \beta \cos(\theta)} \quad (1.1)$$

where θ is the angle between the observation and the direction of motion, and $\beta = v/c$. Measurements place the magnitude of the dipole around 3 mK. Higher order moments cannot be explained by our motion through the CMBR (since $\beta \sim 1/1000$) and are therefore considered intrinsic anisotropies. There is also an expected component of the dipole nearly 100 times smaller in magnitude due to intrinsic CMBR fluctuations.

Sachs-Wolfe fluctuations [42] are due to frequency shifts created by variations

in the gravitational potential. They may be responsible for the shape of the CMBR angular power spectrum for multipole moments $l < 100$. In Cold Dark Matter models, it is this effect which leads to the $\sim 20\mu\text{K}$ quadrupole detected by the Differential Microwave Radiometer on the COsmic Background Explorer (COBE/DMR) [45], [3].

Any initial perturbation can be described as a sum of adiabatic and isocurvature components. Inflationary models predict adiabatic density modes. These are variations in the energy density (number of particles) where the entropy remains constant for a given particle species i : namely $\delta(n_\gamma/n_i) \sim \text{Constant}$ where n_γ is the photon number density and n_i is the number density for a species i . In a perfect fluid, this is equivalent to a proportionality between the pressure and energy density variations. Adiabatic models favor early formation of large scale structure which subsequently fragments to form smaller structure. Isocurvature modes, on the other hand, involve changes in the number density of particles without affecting the total energy density. The energy density remains constant despite the fluctuations because any excess in one species is balanced by a deficit in another. This model predicts nearly a factor of 2 more large scale density power than the adiabatic scenario. It also predicts that smaller scale structure formed first then clustered later.

The simplest working models assume adiabatic perturbations. These models predict that acoustic density (compressional) and velocity fluctuations in the photon-baryon fluid lead to what are known as *Doppler peaks* (Figure 1-2). When the wavelength of a given mode falls below the Jeans length so that pressure no longer dominates over gravity, instability is enhanced. Near recombination the Jeans length is $\sim 2\pi c_s H^{-1}$ ($\sim 20,000 \text{ Mpc}$) where the sound speed c_s in an isentropic fluid is $c/\sqrt{3}$. During recombination the sound speed decreases by 4 orders of magnitude which decreases the Jeans length to the size of globular clusters.

The location of the first Doppler peak is near $l \sim 220/\sqrt{\Omega_{total}} \sim 200$, or about 0.5° . Anisotropy on this scale is enhanced over that at small l . The height of the Doppler peaks is augmented by several competing factors; a thorough account of the underlying physics of the expected power spectrum can be found in Hu and Sugiyama [27].

The degree to which Sunyaev-Zel'dovich (SZ) [48] [49] distortions play a role in measurable anisotropy is still being debated. The amplitude of inverse compton scattering off hot electrons is tied to the electron distribution during recombination and subsequent reionization. It has been shown that nearby rich clusters such as the Coma Cluster can produce $\Delta T/T \sim 10^{-5}$ on arcminute scales (for example, [22]). In addition, some SZ predictions [25] [47] point to possible mechanisms which can produce significant impact on the CMBR spectrum.

At small angular scales ($l > 1000$), photon diffusion (Silk Damping [44]) tends to reduce fluctuations of both the photon and baryon distributions. Figure 1-2 shows a schematic of a typical radiation power spectrum predicted by the Standard Model (taken from Steinhardt (1994) [46]). The sum of the various contributions described above determine the total power spectrum. A measure of the amount of anisotropy

at a particular angular scale is the spherical harmonical moment amplitude C_l times $l(l+1)$. The curve must be normalized to experimental data through free parameters.

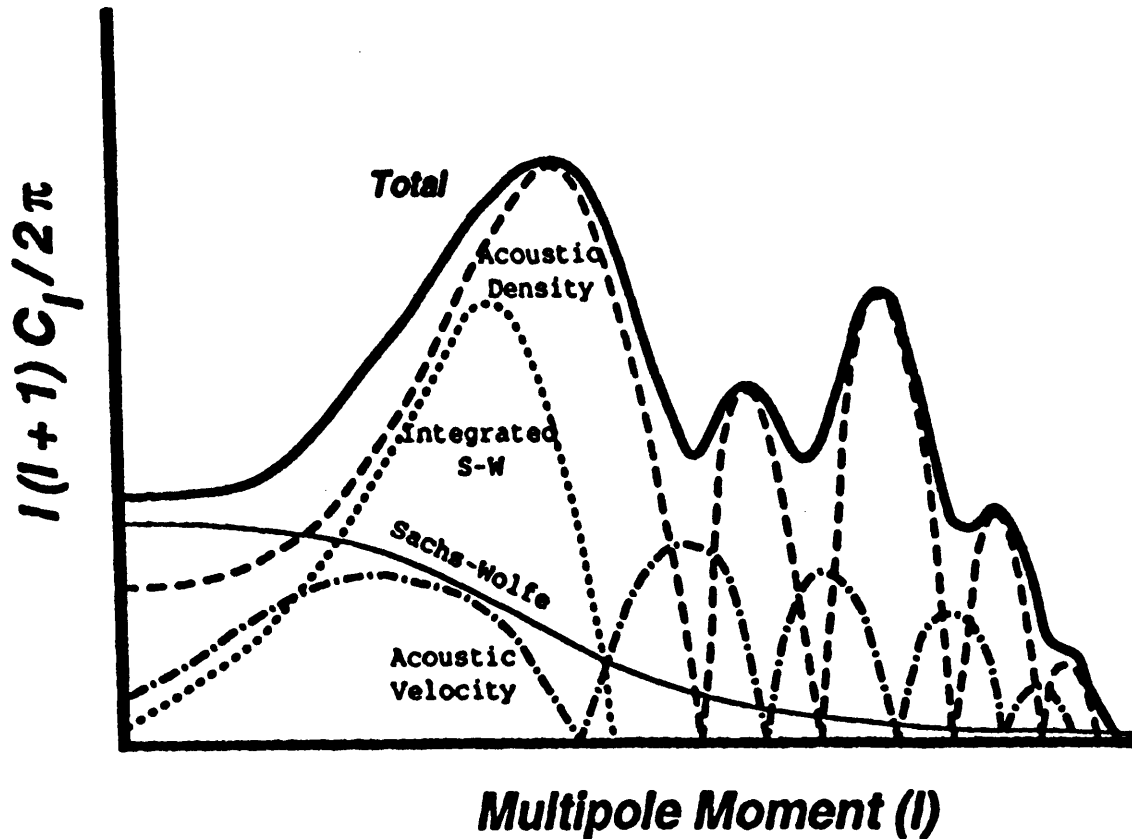


Figure 1-2: Schematic of the radiation power spectrum in the Standard Model showing the contributions from the Sachs-Wolfe effect and acoustic oscillations (adapted from Hu and Sugiyama 1994). The spherical harmonic moment l represents the apparent angular size today where $l \sim 60/\theta_{degrees}$. The y-axis represents the amplitude of MBR temperature fluctuations. The largest peak is known as the first Doppler peak and is located near $l = 200$.

1.2 Current Microwave Background Radiation (MBR) Anisotropy Measurements

There are more than a dozen experiments³ working towards measurement of spatial anisotropy in the CMBR⁴. Figure 1-3 summarizes the anisotropy limits measured by many of these experiments. To facilitate comparison, the data is referred to the best fitting amplitude at the quadrupole Q_{flat} of a flat power spectral model. Q_{flat} is related to $l(l+1)C_l$ by

$$l(l+1)C_l = \frac{24\pi}{5}Q_{flat}^2 = Constant \quad (1.2)$$

To relate C_l to the power $(\Delta T)^2$ measured by an experiment with a window function⁵ W_l , use

$$(\Delta T)^2 = \sum_l \frac{2l+1}{4\pi} C_l W_l \quad (1.3)$$

Large scale satellite projects (MAP, FIRE, COBRAS/SAMBA,PSI) and long duration balloon-borne (TopHAT,Boomerang) experiments represent the future of this research. The principle goal of these measurements in the next decade is to map a large portion of the angular power spectrum.

1.3 Overview of Thesis

This thesis focuses on the design, usage and results of the MSAM I (1992). Although some integration time was devoted to observing the Coma Cluster, these data will not be discussed. Chapter 2 describes the MSAM I (1992) instrument and flight procedures. Chapter 3 will focus on the details of the flight as well as possible systematic errors. Chapter 4 presents the analysis of the data. Chapter 5 summarizes the current investigation of the measured MBR fluctuations. The four appendices

³MSAM I (1992) [8], Big Plate [56], Tenerife [21], ACME-SP91 [18] [43], ACME-SP89 [33], Python [17], ACME-MAX [12] [15], ACME-SP94 [20], White Dish [51]), ARGO [14], OVRO [41], CAT, IAB [39]

⁴It is within the assumption of the Standard Model that these experiments claim to measure *cosmic* signal.

⁵The window function W_l is the sensitivity of the telescope at multipole l due to its observation scheme.

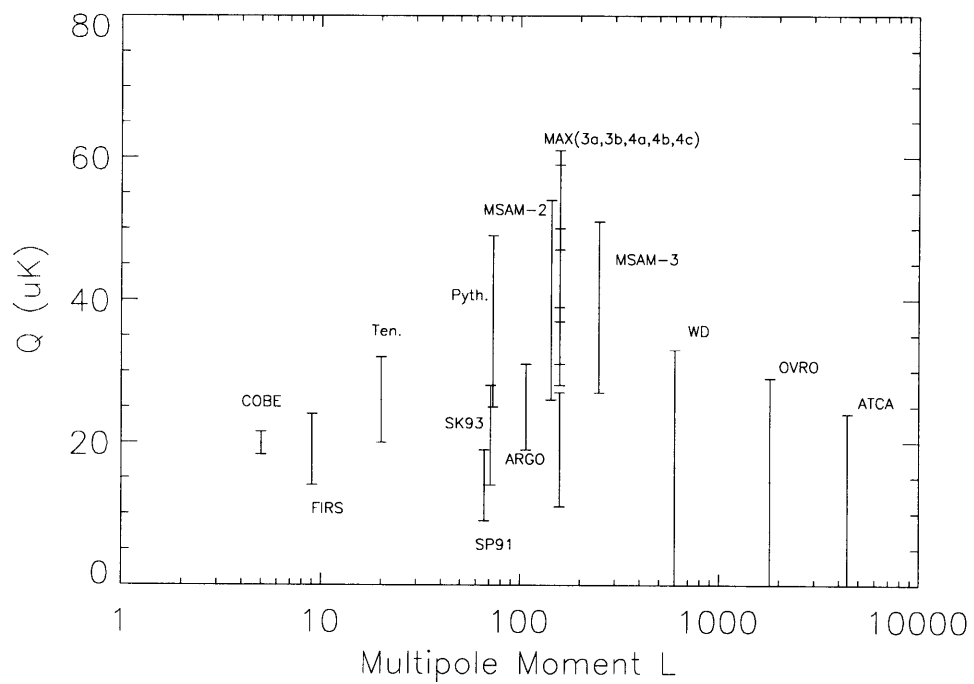


Figure 1-3: Measured anisotropy for 12 experiments. The best-fitting amplitude Q_{flat} of a flat power spectrum quoted at the quadrupole. The vertical error bars are 2σ confidence intervals. Modified from D. Scott astro-ph 9502011.

outline details of the calibration, event timeline, flight statistics, and correlations between MSAM I (1992) sensors and the demodulated data.

Chapter 2

The MSAM I (1992) Instrument

2.1 Introduction and Overview

MSAM I (1992) is a balloon-borne, four spectral-channel telescope mounted on a pointing platform gondola. There are several factors which drive the design of the MSAM I experiment. The principle considerations and the manner in which MSAM I deals with these concerns are:

- (1) *It is advantageous to observe in several frequencies to provide a means of spectral decomposition. Many of the foreground radiation sources have an expected frequency dependence which is different from the MBR and thus can be differentiated.*

The four channels chosen are optimized to provide a handle on expected foreground sources (see Chapter 4). The lowest frequency channels (168 and 270 GHz) are sensitive to the MBR while the highest frequency channels (495 and 675 GHz) are sensitive to $T=20$ K dust and atmosphere. The IRAS sky survey which measured infrared galactic and extra-galactic emission at 100, 60, 25, and 12 μm provides an important check of what is measured in our high frequency channels. A region of low dust emission is chosen when measuring the MBR to minimize confusion which would result if the dust is improperly modeled.

- (2) *Spurious signals such as those due to telescope sidelobe pickup or atmosphere should be minimized. Well designed optics and ground shielding are essential. In addition, various levels of signal modulation, such as chopping the telescope beam on the sky, provide significant rejection of signal which does not originate from the sky.*

The principle level of modulation for MSAM comes from chopping the secondary mirror of the telescope at 2 Hz in a 3 position, square wave pattern. This discriminates against slow variations in the atmosphere as well as slower thermal variations of the telescope itself. The choice of a 3 position chop¹ allows for two types of measurement after each cycle of the secondary mirror: (1) the difference in signal between the outer-most secondary mirror positions and (2) the average of the outer-most signals subtracted from the average of the middle signals. A second level of slow (1 minute) modulation is provided by the motion of the gondola which moves the telescope beam on the sky along the same line as does the secondary mirror. Thus, once the data is synchronously demodulated with the motion of the secondary mirror, it needs to be binned according to gondola position (i.e. the position of the beam on the sky). Details of these methods are covered in Chapter 3.

Since emission from the atmosphere, Earth, Moon, balloon, and gondola can mimic sky signal to varying degrees, MSAM I is designed with these specific considerations in mind. Our experiment is flown on a 40 million cubic foot balloon at 35 km where the atmospheric pressure is a factor of 250 less than at sea level. The launch takes place at night and is chosen to coincide with a time when the moon is not near our observation region. Aluminized shielding around the telescope prevents most spurious emission from the Earth, Moon and balloon from entering the field of view.

Although there are regions of less dust than the one which we observe, to track these areas as the sky rotates requires viewing through varying amounts of atmosphere. Atmospheric emission seen by the telescope increases as the amount of atmosphere through which is observed increases. A reasonable compromise takes advantage of both a low dust region at a declination of 82° ² as well as the rotation of the sky. By centering our telescope antenna pattern on the meridian, tracking the sky rotation for 20 minutes, then returning to the meridian, we can maintain an observation of a low dust area without significantly changing the amount of atmosphere through which is viewed.

- (3) *The telescope beam size and beam throw determines what scale processes are measured. For example, large scale structure in the universe corresponds to a beam size of $\sim 1^\circ$. Larger beams, such as that of COBE, probe effects causally disconnected the time of recombination.*

To characterize perturbations which give rise to observable large scale structure and to explore the power spectrum near the predicted first Doppler peak, MSAM I (1992) measures the spatial anisotropy of the MBR on 0.5° angular

¹The motion of the secondary mirror moves the telescope beam between three adjacent positions on the sky at 2 Hz. The resulting spatial response of the telescope is called the *antenna pattern*.

² 8° above the North Celestial Pole (NCP) as viewed from the Earth

scales. The telescope beam diameter is approximately 0.5° and each move of the secondary mirror throws the beam 0.7° on the sky. The beam size also drives the size of the optics used by MSAM I since smaller beams require larger mirrors.

- (4) *The data should be calibrated against a known thermal source during the observations.*

Jupiter acts as our primary calibration. Its brightness temperature is known to better than 10% in each of the spectral bands. Sweeping the telescope beam over Jupiter (effectively a point-source on our beam) allows for a measurement of the telescope response as modulated by the secondary mirror. A demodulation scheme designed around the observation of a point source is then applied to the MBR data. Figures 3-3 and 3-4 show the antenna patterns.

- (5) *During the above maneuvers, there should be a way to confirm where the telescope is pointed as well as to monitor the position of the gondola and the secondary mirror.*

Pointing position is determined from a star camera, gyroscopes, magnetometers, and inclinometers. Viewing of stars near the NCP with the star camera provides the main pointing reference as well as a way to trim the gyroscopes. The secondary mirror position is monitored to within a few arcseconds throughout the flight.

The details of the design and operation of MSAM I (1992) will be discussed in the rest of this chapter, including the telescope optics, detectors, gondola, and electronics. The specifics of the observation strategy will be covered in Chapter 3.

2.2 Optics

MSAM I (1992) is a 51° off-axis Cassegrain telescope on an altitude-azimuth mount with a 1.37×1.53 meter primary mirror. The focal length is 1.47 m. The secondary is a warm (room temperature) 0.27×0.31 m convex hyperbolic mirror. A $T \sim 5$ K elliptical concentrator Winston cone of length 275 mm matches the internal optics of the dewar to the telescope. The primary and secondary mirrors have a surface roughness of about $\sigma < 10\mu \sim 0.024\lambda$. Based on calculations of Piccirillo et al. [38], this surface roughness means that a single difference signal from the earth at 1 mm wavelength would be $< 1 \times 10^{-5}$ at a 45° elevation angle without ground shielding.

The telescope components are fixed to a frame, called the *strongback*, which rotates in altitude. The strongback is held by the gondola frame. See figure 2-1.

The secondary mirror is held ~ 45 inches in front of the dewar by trussed arms attached to the sides of the strongback. These arms also support the chopper drivers,

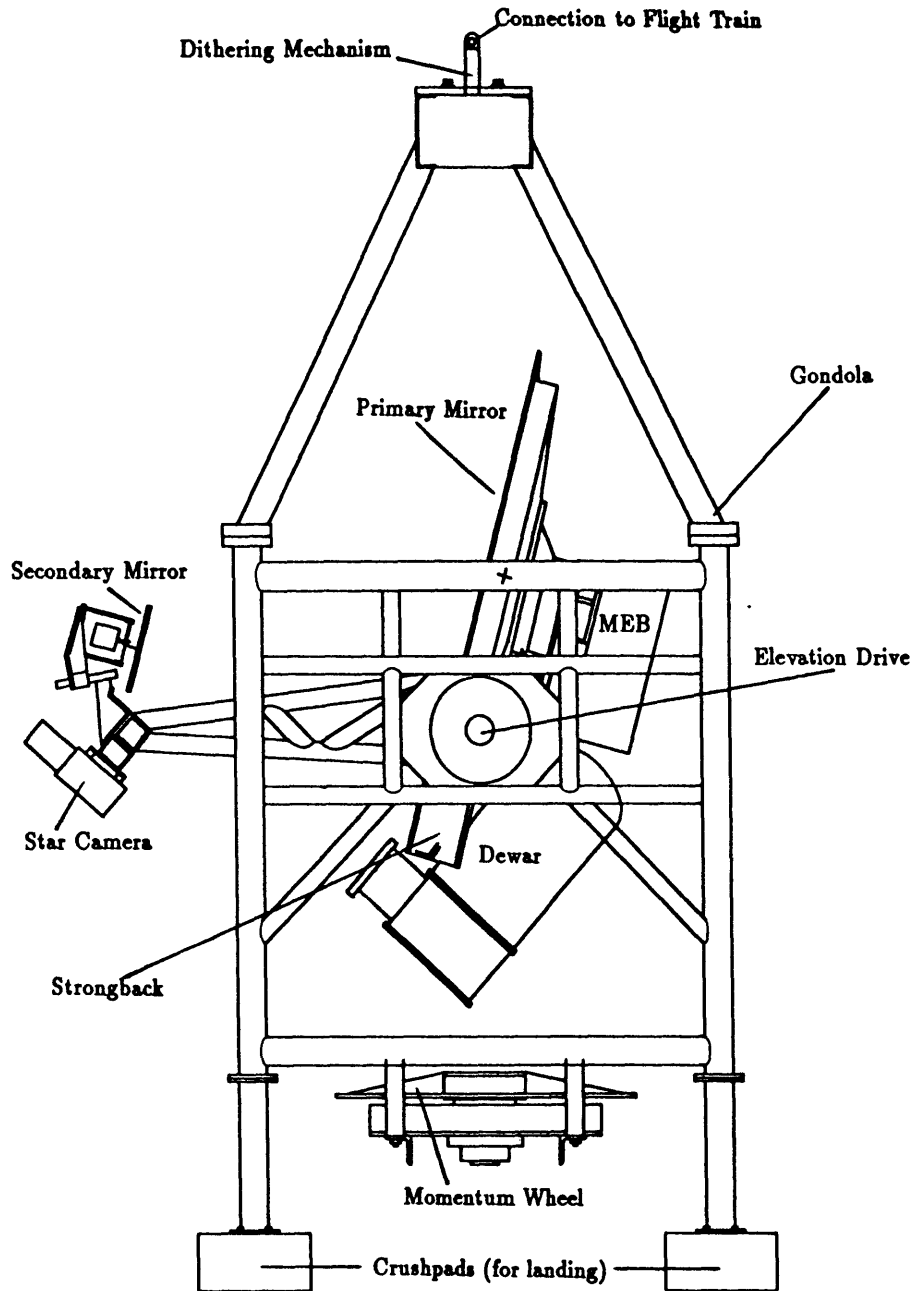


Figure 2-1: The MSAM I (1992) gondola.

their power amplifier, and a star camera used as a visual pointing reference. Since the frame is sensitive to resonances near 45 Hz, small amounts of imbalance in the chopper can feed microphonics to the dewar. The chop rate was modified until integrations of 20 minutes showed no signs of microphonic pickup from the chopper motion.

Modulation of the beam on the sky is accomplished by chopping the secondary mirror servoed to a reference waveform. The mirror (chopper) executes a 3-position symmetric square wave chop at 2 Hz. The time of transition (90%) is 23 ms which leaves 102 ms for integration in each position. The detectors are sampled synchronously with the chop cycle. Chopper motion is monitored by a Linear Variable Differential Transformer (LVDT) sampled at 8 Hz, which is once per chopper position. A Linear Velocity Transformer (LVT) monitors the velocity. Both position and velocity information along with a reference signal are included in the analog servo loop. Both the offset and amplitude of the chopper position are stable to 4 arcseconds throughout the flight. Linear actuators (Gearing and Watson GWV4) drive the mirror. The cycle-averaged power usage is 35 W, most of which is needed to displace the centering flexure springs.

During the chop, mirror rotation is 1.7° about its principle axis and leads to a sky motion of ~ 40 arcminutes. Beam size on the sky depends slightly on chopper position. Coma and optical misalignment of the telescope broaden the left (L) and right (R) beams with respect to the central (C) beam. Table 2.1 shows the approximate beam widths as determined from flight observations of Jupiter where the telescope's measured solid angle is $\Omega = \int B d\Omega$ and $\theta_{\text{diam}} = 2\sqrt{\Omega/\pi}$.

Table 2.1: Beam Sizes for MSAM I 1992

	$\theta_{\text{diam}}(\text{arcminutes})$		
	L	R	C
Ch 1 :	28.7	30.0	26.3
Ch 2 :	29.6	29.5	27.3
Ch 3 :	28.7	28.8	27.4
Ch 4 :	27.9	27.7	26.0

2.2.1 Alignment

The MSAM I (1992) internal radiometer optics are maintained in a rigid configuration. However, the beam emerging from the dewar needs to be referred to the secondary mirror and the subsequent reflected beam to a location on the primary.

The alignment procedure is complicated by several factors. First, the MSAM I (1992) gondola does not provide an efficient way to adjust the position of the dewar. Second, the position of the secondary mirror can not be adjusted horizontally: this means the dewar must be adjusted to point toward the secondary. Since the primary and secondary are nearly of optical quality, visual sighting can aid in alignment.

The following procedure was followed to align the MSAM I (1992) telescope:

- (1) While off the gondola, the dewar beam map was measured 45 inches away (the design distance from the secondary to the dewar horn). This checked that the dewar optics were functioning as well as giving a reference map.
- (2) The dewar was mounted on the gondola such that it pointed toward the secondary. The distance from the dewar horn to the optical center (OC) of the primary was measured to be within 1 cm of the design length.
- (3) The secondary was mounted on the gondola in the design position.
- (4) The dewar beam was mapped from the left, right and top edges of the secondary outward. Eccosorb prevented reflections within the ground shield.
- (5) From the full dewar map, we determined how much the dewar must be moved to make the integrated spillover be the same on all sides of the secondary and moved the dewar appropriately.
- (6) We stood on a ladder about 30 ft from the telescope and visually aligned the secondary and primary mirrors' OCs³. The OCs, when superimposed by eye, were centered on the dewar horn. Shims were used to tilt the secondary so that the left and right offset positions produced the same displacement of the OCs on the ruler.
- (7) Primary edge response was checked by moving cold (LN₂ cooled) eccosorb into the beam from the edge of the primary. For a given distance from the center of the primary, the response was the same.
- (8) Lastly, a beam map of the entire telescope was constructed outdoors using a blackbody source of approximately 1000 K in the telescope's far field. Since the blackbody also emits visible light, this test was used to refer the infrared telescope beam to the star camera's field of view. An optical theodolite served as a pointing reference.

This procedure lacks one critical bit of information: the beam profile on the primary mirror. For the 1995 campaign we will cover the primary with eccosorb and

³Note the secondary and dewar horn look large due to telescope magnification. A ruler provided a visible scale at the dewar horn.

measure the beam at the primary with the secondary in its unchopped and chopped positions. It is expected that the beam will move on the primary by a few inches, however, the primary has a 4 inch flat region around its perimeter so that the edges of the beam are still reflected to the sky. We will shim the secondary as needed to center the beam on the primary while maintaining the OC alignment described above.

2.2.2 Detectors

Table 2.2: Bandpass Characteristics of MSAM I (1992) Radiometer

Characteristic	Channel 1	Channel 2	Channel 3	Channel 4
ν_{center}, cm^{-1}	5.5	8.5	15.8	22.5
$\Delta\nu, FWHM, cm^{-1}$	1.3	2.4	1.6	1.2
$\Delta\nu/\nu$	0.23	0.26	0.1	0.05

The radiometer was constructed at MIT and is the same one used for the Far InfraRed Survey (FIRS) experiment [36], [37], [34]. Radiation is monitored in four bandpasses (see Table 2.2.2). The detectors are monolithic silicon bolometers doped with Bismuth and Phosphorous [16]. The Noise Equivalent Power (NEP) is $\approx 3 \times 10^{-16}$ Watts/ $\sqrt{\text{Hz}}$. A combination of Fluorogold and aluminized mylar filters determines the characteristics of the high and low frequency spectral response. The first three channels use etched aluminized mylar capacitive mesh filters in a double half-wave configuration (Cunningham 1983; Holan et al. 1979; Dragovan 1984). The fourth channel uses a Cochise Instruments inductive mesh filter. The filter responses measured after the flight are shown in figure 2-2.

In the limit that there are no optical losses in the dewar, the étendue of this system is conserved and can be determined from the the detector size $A_{\text{det}} = 0.159\text{cm}^2$ as:

$$A\Omega = \int_0^{2\pi} \int_0^{\frac{\pi}{2}} A_{\text{det}} \cos \theta \sin \theta d\theta d\phi = 0.5\text{cm}^2\text{str} \quad (2.1)$$

Maps of the beam profile of the dewar indicate a possible problem not anticipated during the design (see Figure 2-3). A geometrical ray trace code was used to predict the beam width and aberration. Results from this ray trace indicate that not only do the measured beam maps exhibit significant unexpected structure at the 10% level but also the effective widths are larger than the design specification. This larger width translates to beam spillover at the secondary mirror of 11%, 6%, 3%, 4% in the four bands. A major concern is whether the radiometer is sensitive to stray signal

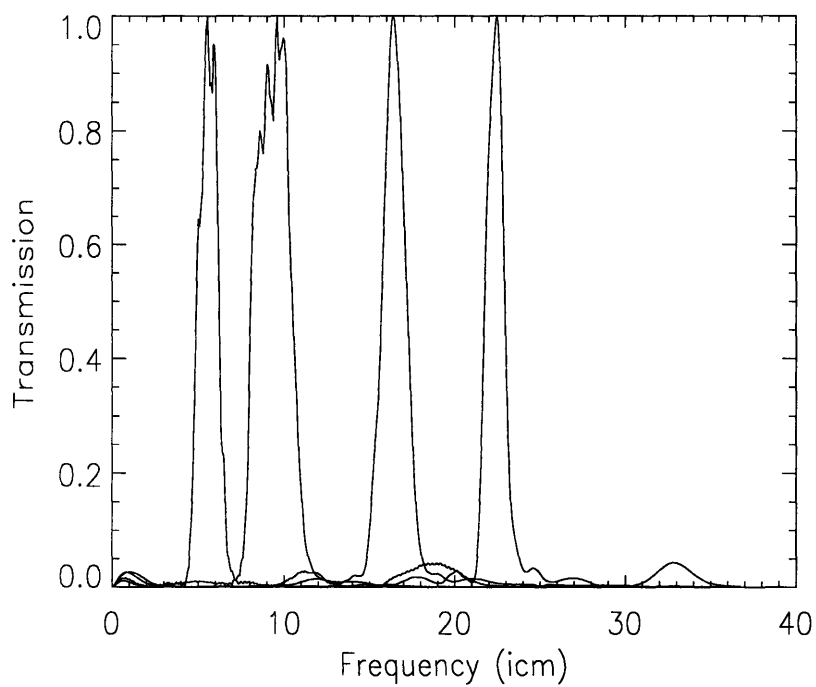


Figure 2-2: The normalized spectral responses to a 1000 K black body source. The harmonics are due to reflections in the measurement setup.

not directly in the beam. Great care was taken to try to ensure that any spillover was directed toward the sky. Sidelobe sensitivity is discussed in detail in Chapter 3.

A $^3\text{He} / ^4\text{He}$ refrigerator cools the detectors to 300 mK. With the cold detectors subjected to room temperature loading, the ^4He lasts for approximately 18 hours before a transfer becomes necessary. The ^4He has a hold time of one week after which a 24 hour recycling procedure can return the optics to 300 mK. Details of the design and operation of this refrigerator are given in Cheng et al. [9]. A cut-away view of the dewar is shown in Figure 2-4.

2.2.3 Gondola

The MSAM I (1992) gondola is constructed primarily of aluminum, stands nearly 15 feet tall and weighs about 3500 pounds. Azimuthal rotation is accomplished by spinning up a large mass momentum wheel located at the base of the system. Pointing is stable to a few arcminutes on 20 minute time scales. Two elevation drives rotate the strongback about the telescope center of gravity on an axis parallel to the horizon.

MSAM I (1992) is endowed with several position monitors. The azimuth is referenced to two independent magnetometers. First, there is a two-axis magnetometer which rests on the external gondola frame and is part of the servo loop controlling the gondola. Second, a three-axis magnetometer mounted on the strongback provides telescope tilt information. Magnetometers, however, do not provide enough accuracy for fine pointing. MSAM I (1992) also has two sets of gyroscopes. The first gyroscope, again on the strongback, has arcsecond accuracy and sub-arcminute drift in 20 minutes. One rotation axis points along the optical axis of the telescope. This gyroscope is part of the attitude control of the gondola. The second gyroscope pair, mounted on the gondola, is used to monitor the pitch and roll of the whole platform.

Pointing position is also determined from a Charge Integrating Device (CID) star camera located under the chopper but outside of the ground shield. The camera can view objects down to 6th magnitude which is sufficient to allow viewing of Gamma Ursa Minoris near our observation field. The field of view is 4° by 8° with a resolution of ~ 4 arcminutes. The integration required for 6th magnitude images is about 10 seconds. Hence, the gondola must remain stationary while acquiring a faint image. Jupiter is, however, bright enough to see while being scanned. A confirmation of the alignment between the infrared beam and the star camera is performed during the flight.

Angular momentum acquired by the momentum wheel is removed with a frictional torque mechanism between the top of the gondola and the balloon flight train. Since the flight train is quite long (about 360 ft), it accommodates a substantial twist. The torque mechanism is also included in the pointing servo loop. When the lower momentum wheel attains high enough angular velocity, the upper mechanism torques against the flight train, transferring the angular momentum to the balloon. The mechanism is covered with a conical shield to prevent reflected radiation from being

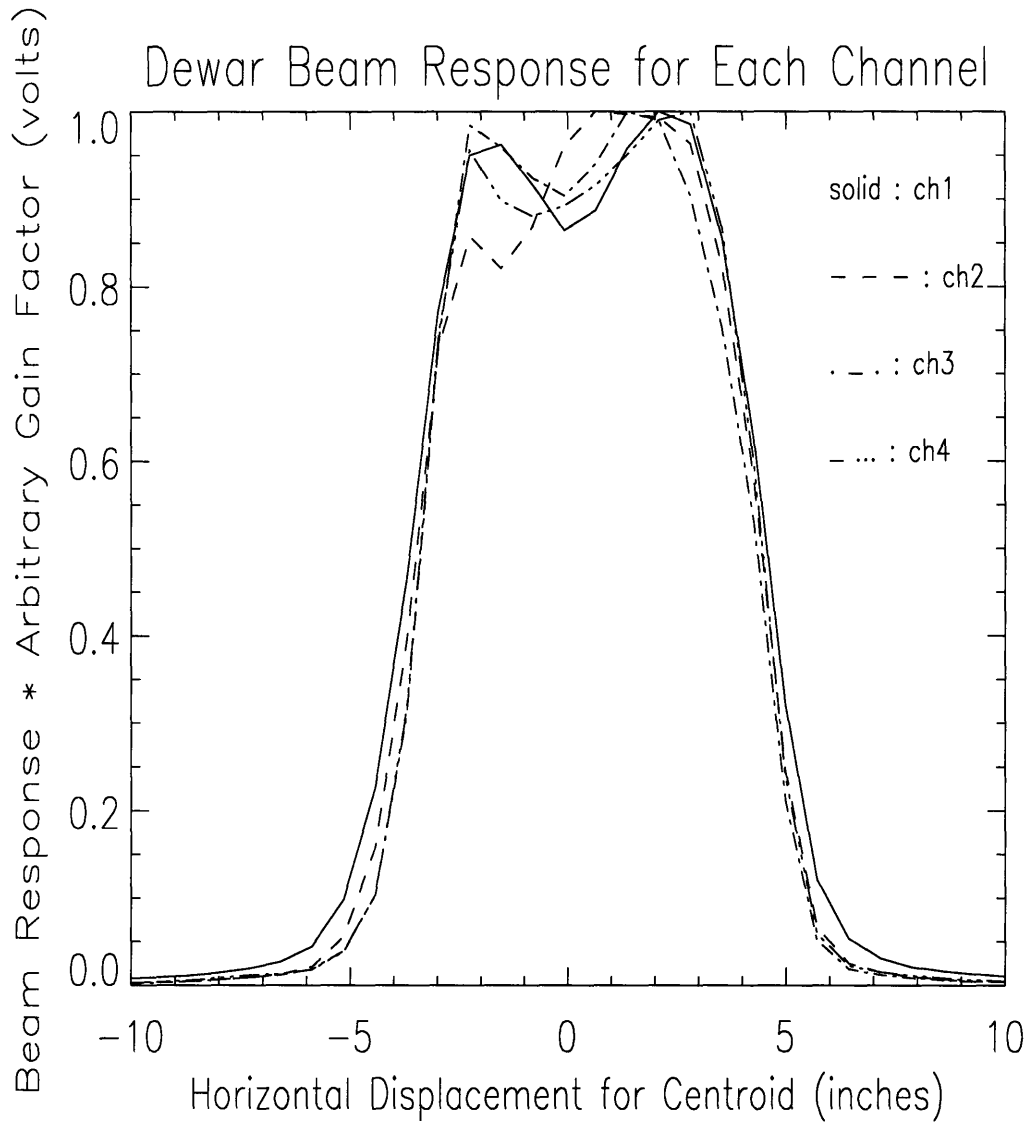


Figure 2-3: The dewar beam response approximately 45 inches from the front of the Winston cone. These profiles indicate the response over the plane which approximates the location of the secondary mirror surface.

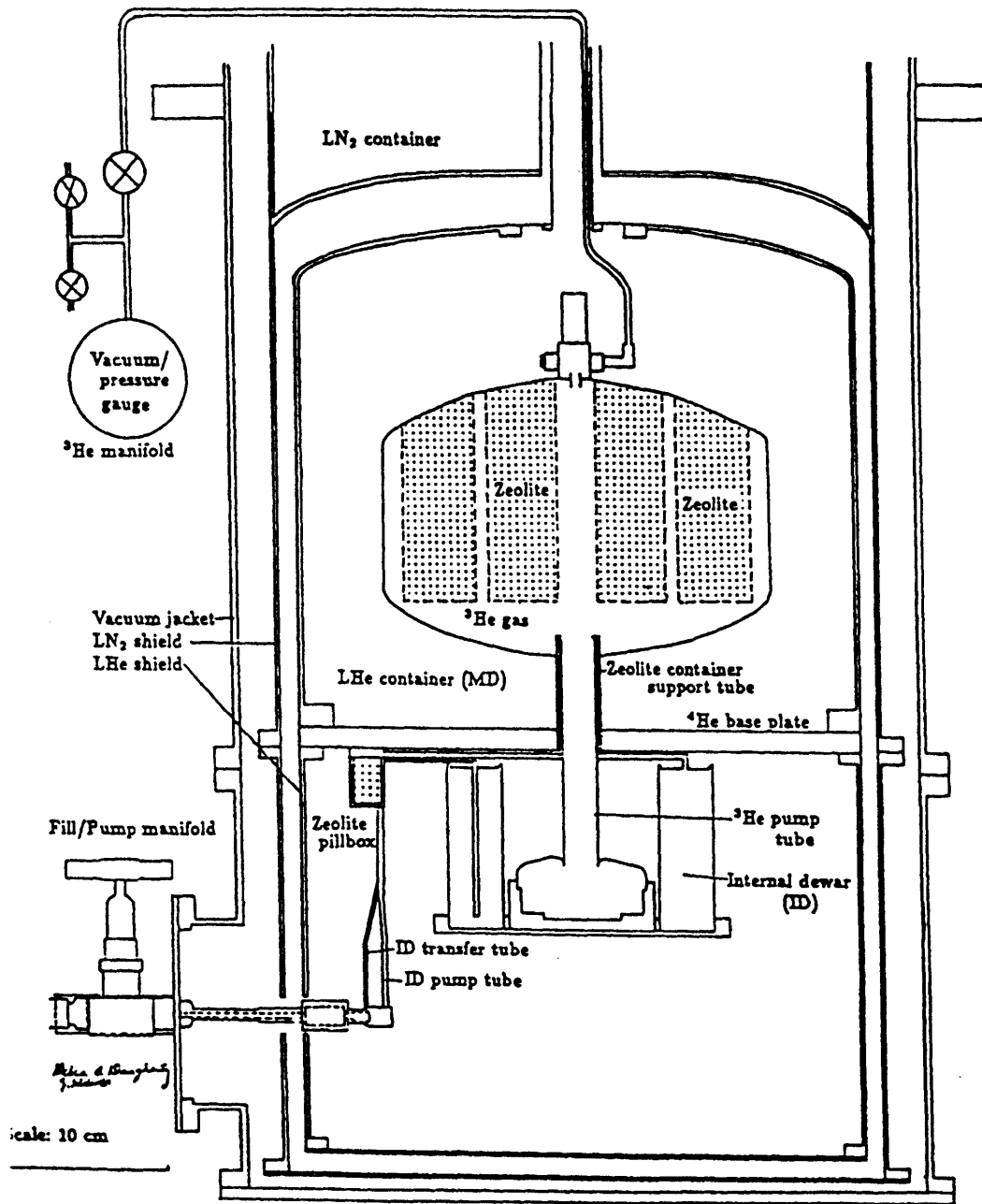


Figure 2-4: The refrigerator which houses the detectors and optics for MSAM I (1992). The detectors are mounted on the 300 mK ID.

modulated by its movement.

2.3 Electronics and Telemetry

Much of the electronics specific to the radiometer is the same as that used in the FIRS experiment. The details of the electronics and telemetry system specific to the radiometer are described in detail in Lyman Page's 1989 PhD thesis [36]. Below I describe the detector signal path.

Upon leaving the detector, the manganin wire signal leads are thermally sunk to 4.2 K on the way to an internal preamplifier. This preamplifier uses 2N4867A Siliconix JFETs in a gain 15, class A configuration. The temperature of the JFETs is regulated at 80 K since they do not work well below 67 K. From here, the signal goes to the external preamplifier. Its metal shield connects directly to the dewar and encloses its electronics in the same Faraday shield as the electronics internal to the dewar. The external preamplifier imparts an additional gain of ~ 15 . It is temperature regulated to 270 K. The signal is highpassed with a 3 dB frequency of 0.3 Hz. Pi filters are used between this preamplifier and the Main Electronics Box (MEB) to block RF leakage into the dewar.

In the MEB, a commandable gain from approximately 1 to 700 can be applied. A V/f converts the voltage into a frequency. The signal is then integrated over 1/4 of a chopper position (1/32 second). The phase of the integrations relative to the secondary mirror transitions is also commandable.

The MEB converts the detector signals as well as other radiometer statistics into digital words. The gondola monitors are digitized in a similar fashion but using separate electronics. All MSAM I (1992) flight data is telemetered to a ground station by a Consolidated Instrument Package (CIP) supplied by the National Scientific Balloon Facility (NSBF). The CIP acts as a receiver and transmitter for experiment data and commands. It contains subcarrier oscillators, a command decoder, equipment for the determination of altitude and position, and batteries. We transmit both discrete (on/off) and 12 bit digital commands. The information is sent via standard IRIG SCO channels B (Camera), E (MEB), HH (gondola). Transmission range is limited to the horizon distance which is about 335 nautical miles at 100,000 feet [35].

The ground station is a μ Vax Workstation II with a custom-designed interface board. Information is relayed from the package to the ground station in bi-phase format. All information received from the gondola as well as a record of commands sent are logged in an archive for future reference. It is also possible to retrieve information from the archive in realtime. This allows for in-flight viewing of our calibration sources and checks that the detectors are functioning properly.

Chapter 3

Flight Characteristics

3.1 Introduction

MSAM I (1992) was successfully launched on June 5th from Palestine, TX. The flight provided 11.6 hours of data, 4.5 hours of which were specifically MBR observation. Many of the specifics for this launch and flight are summarized in Appendix C. What follows is a description of flight characteristics directly relevant to the subsequent analysis. This includes (1) the observation scheme, (2) the pointing behavior of the gondola, (3) the telescope antenna response achieved in flight, and (4) a detailed discussion of systematic effects both observed and considered. The entire flight event schedule can be found in Appendix B.

3.2 Observation Scheme

The telescope can operate in either *acquisition* or *inertial* mode. Acquisition mode uses the magnetometers for pointing reference. In this mode, the telescope remains stationary with respect to the Earth; the instrument performs a drift scan. Inertial mode uses the gyroscopes for pointing reference. The sky motion is tracked so that a single spot on the sky can be observed. Motion of the sky beam is always parallel to the horizon which means the beam pattern twists on the sky as the sky rotates.

Chop refers to the movement of the secondary mirror (or *chopper*). The mirror executes a three position square wave cycle as described in the previous chapter. The axis of mirror rotation is approximately perpendicular to the horizon and inclined to the axis defined by the radiometer horn by $\sim 20^\circ$. The movement of the beam on the sky is then also a three-lobed pattern whose major axis is along a line of cross-

elevation. There are some distortions of the side beams due to the rotation of the secondary. The chopper is in motion throughout the entire flight.

MSAM I (1992) observes (in inertial mode) the microwave background in 20 minute blocks of time called *scans*. A scan consists of nodding the gondola back and forth in azimuth by about 1.4° at constant elevation with a period of one minute. The gondola nods in azimuth while the chopper throws the main beam $\pm 0.7^\circ$ in cross elevation. Sky rotation is followed for 20 minutes for one scan. At the start of the scan, the center¹ of the middle lobe of the beam pattern is placed on the local meridian passing through the North Celestial Pole. The intent was to have the center beam start 0.7° east of the meridian but the camera was misaligned by ~ 25 arcminutes. See figure 3-1.

To produce a map of the telescope response in flight, a motion known as a *raster* is used. The raster is a series of 9 azimuth sweeps each at a different elevation. Raster data allows determination of the infrared (IR) beam center with respect to the gondola coordinates in real time. An offset correction can then be sent to the gondola where upon the IR center should be at the center of the map. This requires getting the pointing approximately right before the first raster. The size of the raster map produced is about 3° by 1.5° . It takes 7 minutes to execute a raster.

To determine the sensitivity of the telescope to variations in atmospheric column density as well as other possible elevation-dependent signals, MSAM I (1992) also performs elevation scans. The entire scan from 40° down to 8° and back up takes 45 seconds. There is also an azimuth spin where elevation is held constant while the gondola completes one turn per minute.

3.3 Pointing

Absolute pointing is known during the flight to 20 arcminutes and the relative pointing to 2.5 arcminutes. The position of the infrared beam center in the camera was different during the flight from its position measured prior to the flight by ~ 5.6 pixels (21 arcminutes). The origin of this discrepancy is probably a shift in the camera position during ground tests before the launch. Fortunately, the in-flight planet observations allow us to fix the IR beam center with respect to the camera image during the flight.

The images taken every 20 minutes with the star camera were used to trim the gyroscopes. Corrections of about 2 arcminutes were required every 20 minutes. Figure 3-2 details the IR beam pointing throughout the flight in radial coordinates about the North Celestial Pole. A short (2 minute) commanding problem occurred near an RA of 15 hours. The gap near 17 hours RA corresponds to an observation of the Coma Cluster.

¹It was intended that the left lobe begin centered on the meridian but a star camera offset caused a shift of nearly one beam width.

MSAM Overlapping Scan Method

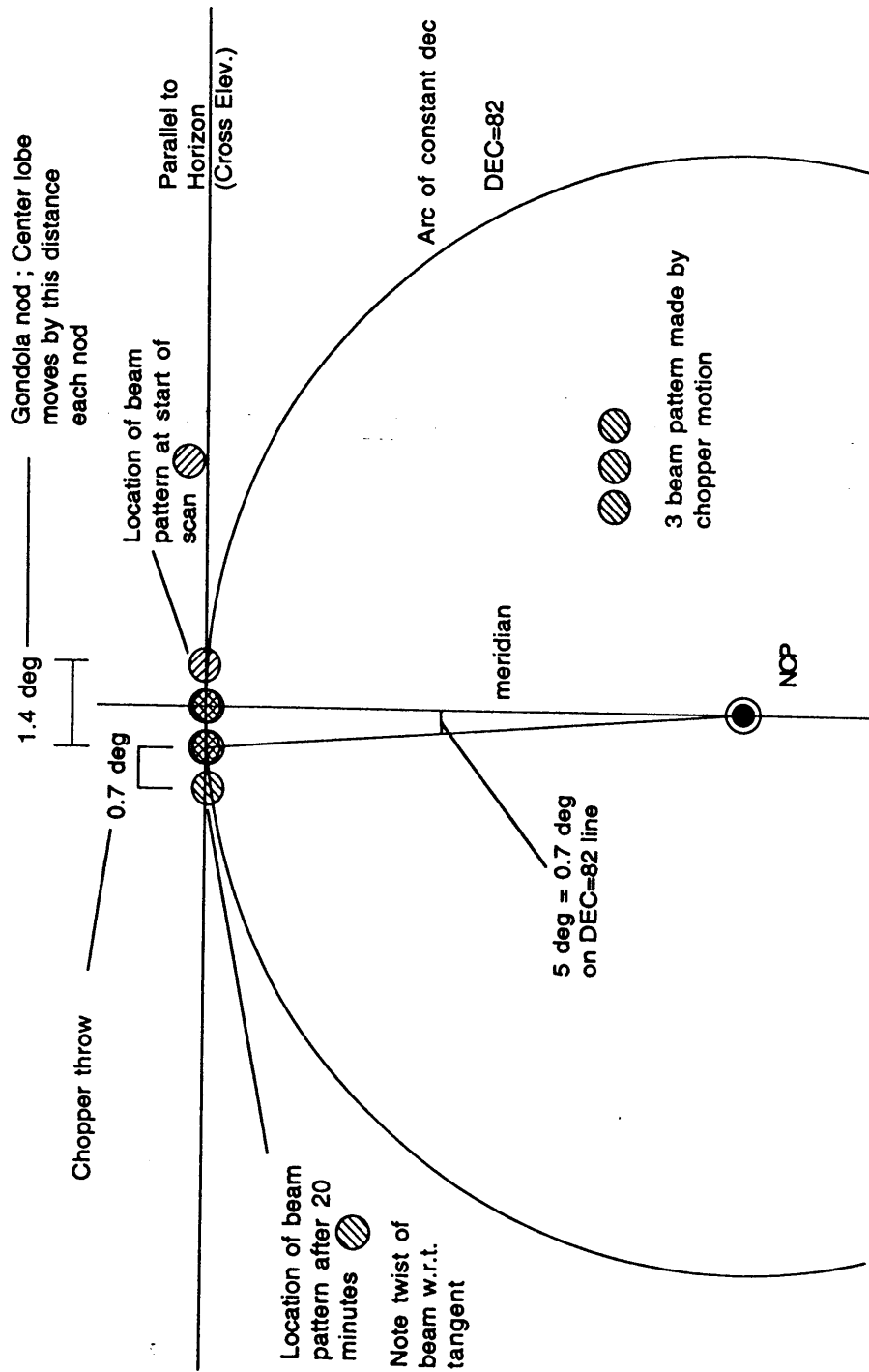


Figure 3-1:

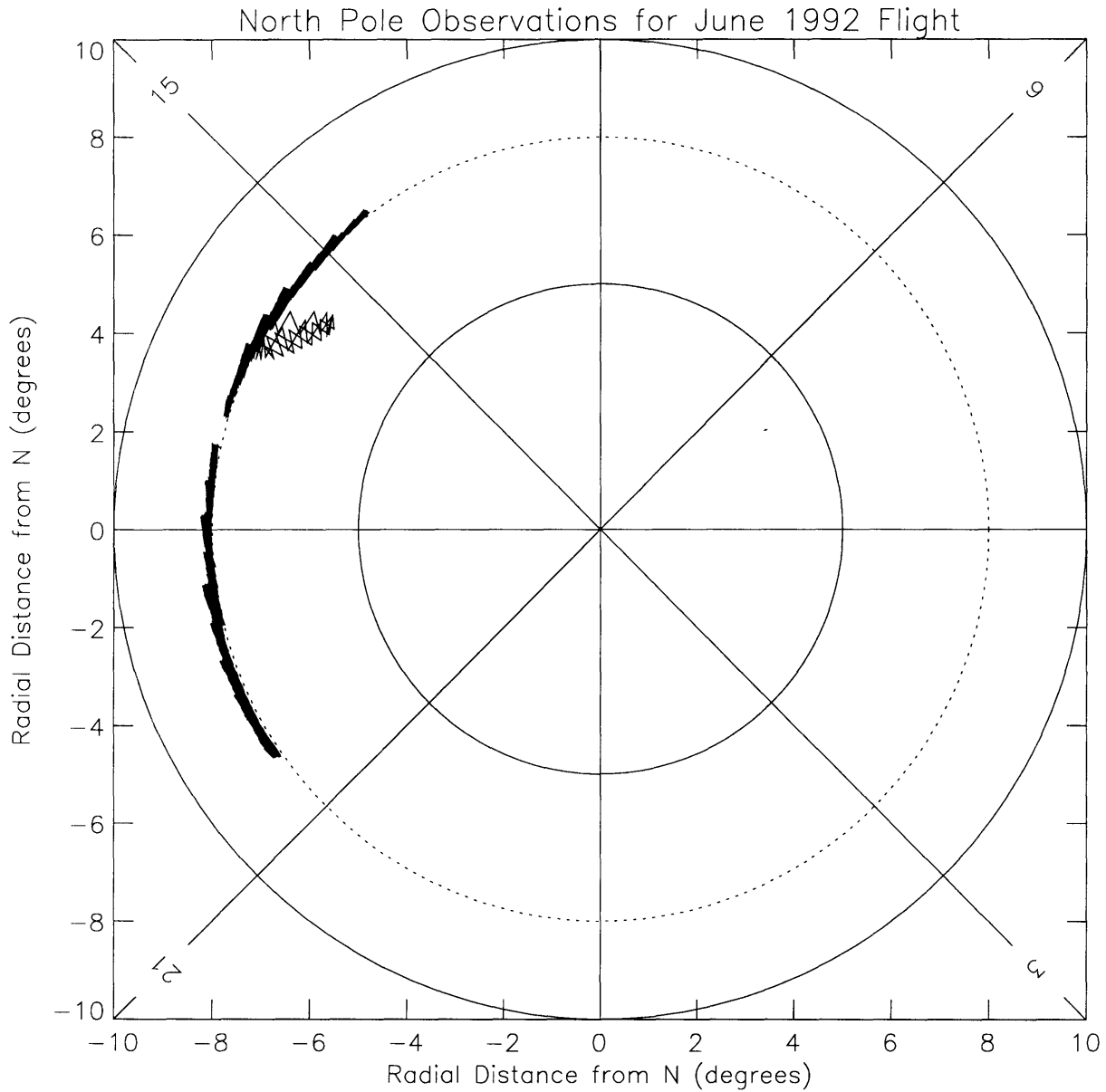


Figure 3-2: The pointing achieved during MBR observations is demonstrated by the width of the line. Hours of RA are shown on the diagonals. The gap represents when MSAM I (1992) stopped to observe the Coma Cluster. The diagonals are RA hours. The squiggle is a commanding problem which lasted a few minutes.

Gondola position relative to the Earth is monitored via GPS (Global Positioning System) and LORAN. When redundant information was available, agreement between measurements of latitude and longitude is consistently offset by nearly 0.02° ; the GPS data are used in our analysis. In addition, a pressure sensor monitors elevation changes while at float.

3.4 Planet Rasters and the Antenna Response

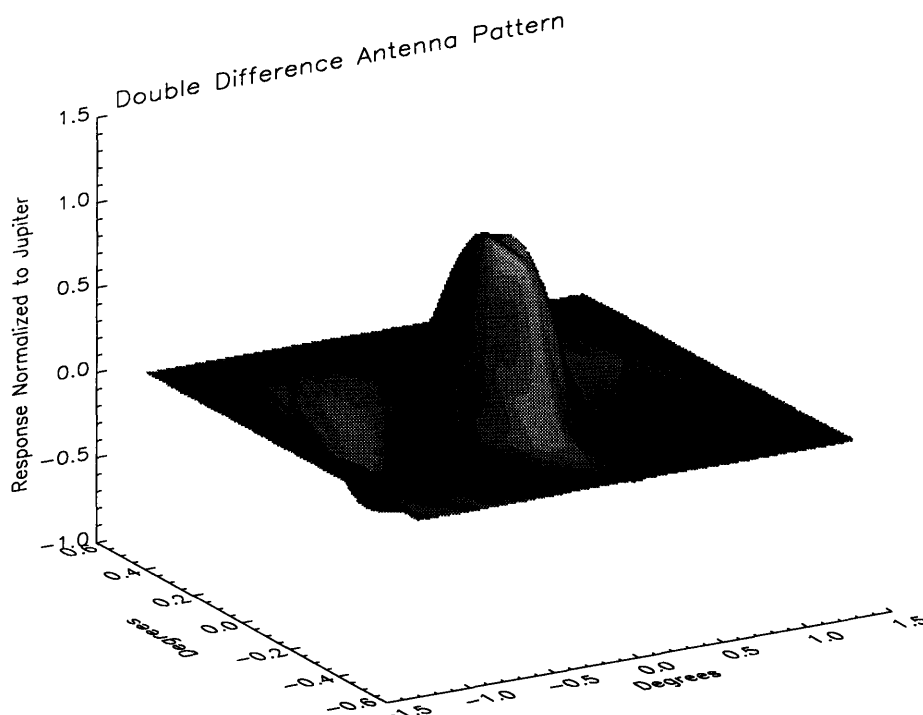


Figure 3-3: The double difference antenna pattern measured from the rasters over Jupiter. Those made from Saturn are similar but have $1/5$ the signal to noise.

To check for gradient drifts in the calibration, pointing and offset, observations include a raster of a planet at both the beginning and the end of the flight. These planet observations took place when the objects were at nearly the same elevation as the MBR scans ($\sim 39.5^\circ$). Rastering on a planet of known brightness temperature makes it possible to determine the in-flight antenna response. Since Jupiter has fairly well established brightness temperatures between 5 and 25 cm^{-1} , we are confident of our calibration to 10%.

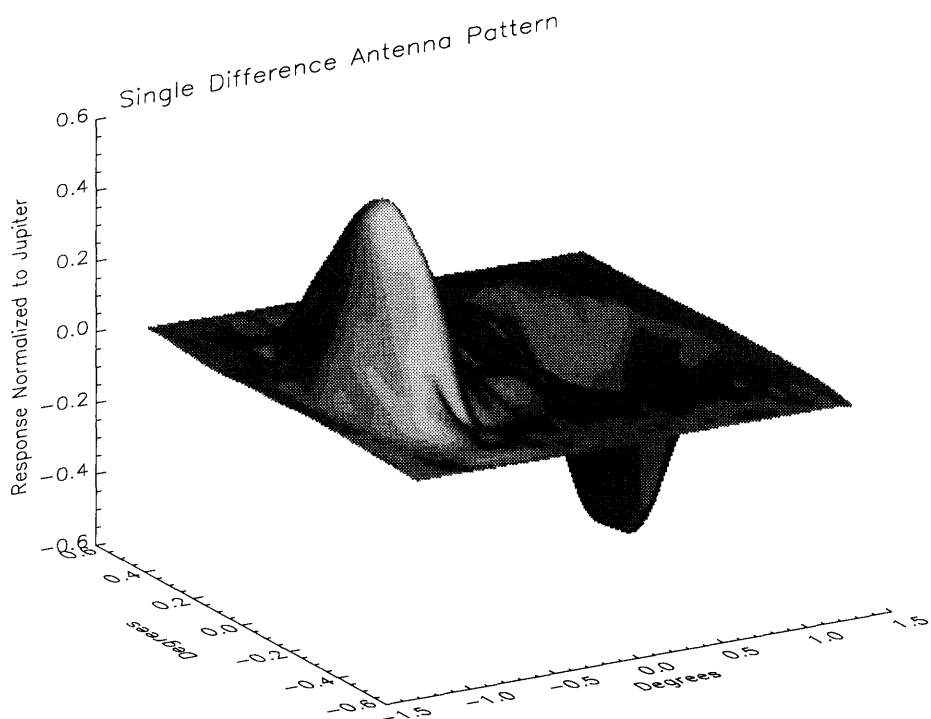


Figure 3-4: The single difference antenna pattern measured from the rasters over Jupiter. Those made from Saturn are similar but have 1/5 the signal to noise.

A planet raster is carried out in the following fashion. The gondola nods back and forth in azimuth by 3° with a period of ~ 45 seconds. The elevation decreases by 10 arcminutes after each half cycle. A two dimensional picture is created of the antenna response as a function of sky position centered on the planet. The figures 3-3 and 3-4 demonstrate the chopped point source response of MSAM I (1992) for the double and the single difference demodulation techniques. Normalization is described in Appendix A. The window functions for these two demodulation types are shown in Figure 3-5.

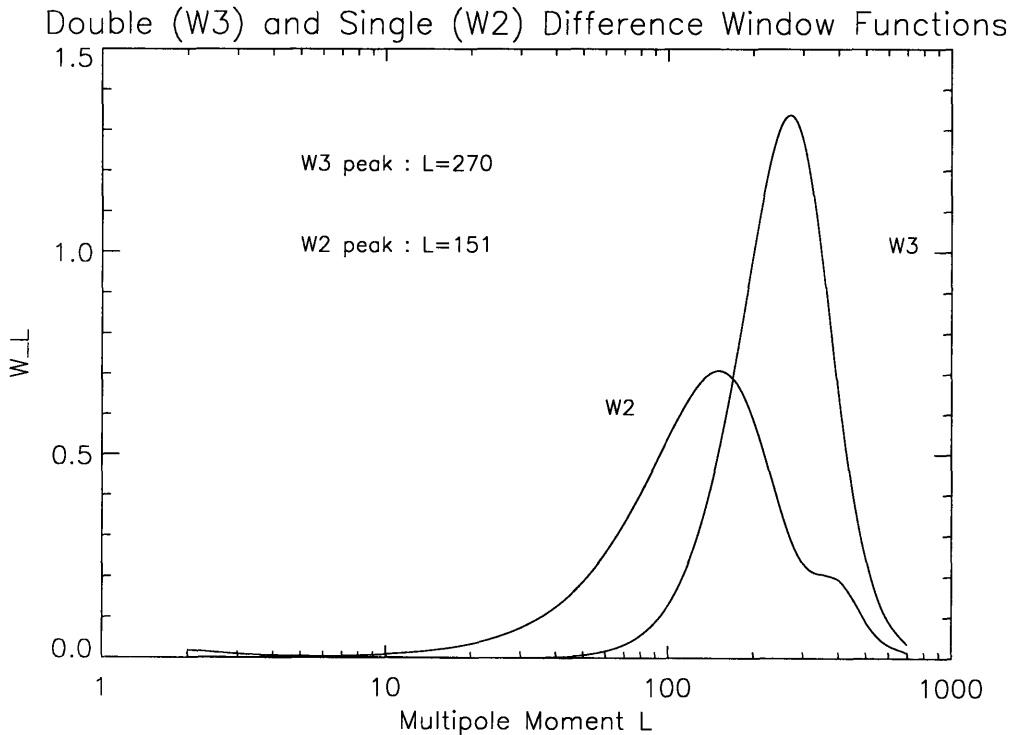


Figure 3-5: The sensitivity of the single (W2) and double (W3) difference demodulations as a function of multipole moment l .

While the full beam maps are not used for demodulating the data, they are used when generating the Maximal Likelihood Statistic. Thus, asymmetries in the beam are included in the Monte Carlo simulations of the experiment. Calibration will be discussed in more detail in the next chapter.

3.5 Systematic Error Sources

Offsets in the chopped response on the telescope can be either constant or variable in time. The contribution of sidelobe pickup, atmosphere, and microphonics needs to be considered. MSAM I (1992) experienced a nearly constant offset in the chopped response of approximately 10 mK. In addition, there was a slowly varying component to this offset which was $< 400\mu\text{K}$. Below I consider spurious sources of both the constant and time variable chopped signal. Tables 3.1 and 3.2 summarize the results which are explained in detail below. Table 4.1 in Chapter 4 shows the measured constant chopped offsets for the two demodulation schemes and for the two quadrature demodulations.

Table 3.1: Summary of Constant Chopped Offset

Type	Description	Amount
Sidelobe	Top Structure	2.5 mK
	Balloon	$20\mu\text{K}$
Microphonics	Chopper	? in flight
		Undetectable on ground w/ 20 minutes integration
Other	Primary ΔT and $\Delta\epsilon$	few mK

3.5.1 Sidelobe Response

Chopped anisotropy experiments need, on average, about 70 dB of sidelobe rejection at 0.5° to ensure an uncontaminated measurement of the sky signal. This number comes from the following rough estimate. The Earth is approximately a 300 K black-body emitter which fills 2π steradians as seen from the telescope. Since there are about 10^5 beams in 2π , for an absolute experiment to measure *a few* $\times 10^{-6}$ K, sidelobe rejection must be nearly 12 orders of magnitude. Relative (chopped) experiments gain about 40 dB of rejection through the modulation of a mirror and the gondola if it is assumed that the Earth's surface temperature is a random field.

The ground shielding of MSAM I prevents any direct illumination of the primary, secondary, or the dewar horn by emission from the Earth. However, Earthshine can reflect into the beam from the gondola upper structure.

Table 3.2: Summary of Variable Offset in Sky Binned Data

Type	Description	Amount
Sidelobe	Earth Horizon	$< 30 \mu\text{K}$
	Top Structure	$25 \mu\text{K}$
	Balloon	$< 25 \mu\text{K}$
Atmosphere	Scan Overlap	$< 50 \mu\text{K}$
	Other	
	Primary ΔT and $\Delta\epsilon$	$< 30 \mu\text{K}$
	Glitches	$< 30 \mu\text{K}$
		(from averaging)

To place constraints on off-axis response of the telescope in channel 1, a 180 GHz source (comprised of a 60.6 GHz Gunn diode with a Millitech tripler) was pointed at several locations on the MSAM I (1992) instrument. Signals from the source, pointed from locations corresponding to the Earth's horizon angle, were attenuated by 55 dB or better in the chopped response (neglecting gondola nod). Approximately, 25% of the regions tested had a -55 dB response. Regions lower than the horizon were diffraction limited by the ground shield and had a rejection of better than 70 dB (the limit of the test sensitivity).

The contrast between Earth and space is effectively 250 K. We can estimate the contribution from the Earth's horizon by assuming 1% temperature contrast on the 0.5° scale. There are about 720 beams in the horizon ring. Since the temperature field is most likely random and the chopped antenna pattern is nearly symmetric, it is the rms signal which matters. This implies $\Delta T = 250 \text{ K} \times 0.01 \times \sqrt{720} \times -55 \text{ dB} \times 25\% \sim 50 \mu\text{K}$. The gondola nod averages horizon regions as well so that the sidelobe contribution to the signal is less than $30 \mu\text{K}$ (the 1σ experimental error bars).

A limit to the MSAM I (1994) far sidelobe response from near the Earth horizon was placed in 1994 with ground-based measurements using Gimme-cap, an on-axis telescope configured in broadcast mode with a 150 GHz diode. Since there was far less upper structure in the 1994 configuration, this measurement is a lower limit to the MSAM I (1992) response. By pointing Gimme-cap at MSAM I (1992) from a distance of 800 m, a significant portion of the azimuthal sidelobe response of MSAM I 1994 was mapped (see figure 3-6). To produce this map, the MSAM I (1992) telescope was pointed up at 45° and rotated in azimuth while the Gimme-cap optical axis was approximately parallel to the ground. The chopped sidelobe response of the MSAM I (1992) telescope remains near -80 dB for the entire rotation. These results confirm that the dominant signal from the 1992 180 GHz measurements came from

reflections off the top structure.

The scattering of the telescope's sidelobes off the gondola structure will contribute to a time-independent signal offset. Most of the signal will come from structure close to the beam. The in-flight antenna maps indicate < -20 dB response 2° above the beam. Assuming 10% contrast between beam positions, 1% emissivity, and 250 K for the top structure, we might expect a constant offset of around $250 K \times 0.01 \times 0.01 \times 0.1 \sim 2.5$ mK. The rms gondola temperature variation seen by each beam is likely to be less than 1% (supported by the gondola temperature sensor data). Thus, the time variable component to this signal will be $\sim 25\mu\text{K}$.

3.5.2 Atmosphere

Atmospheric contamination can be a significant factor when observing from the ground. Lines of H_2O , O_2 , and O_3 contribute emission over the range of our radiometer. Rotational transitions account for the majority of emission lines.

Spurious signal can be added in two ways: (a) as the column density of the atmosphere through which the telescope views changes, the power emitted by the atmosphere will change and (b) spatial or temporal variations in atmospheric density will cause fluctuations in the measured signal. Since we know that the package height oscillates by a few hundred meters (changes in pressure of ~ 0.2 mm) with a period of 6 minutes (a motion called *porpoising*, also seen in the FIRS data), we expect there to be some component of signal due to this effect.

Page [36] devotes a large section to the atmospheric contribution in the FIRS experiment which uses the same radiometer. He considers only the column density mechanism. To summarize Page's results, he finds that O_3 is the principle contributor to the integrated power over our bandpasses for all channels. Table 3.3 lists model results.

From Table 3.3, rough estimates of the 6 minute variation in antenna temperatures during porpoising are $28\mu\text{K}$, $70\mu\text{K}$, $640\mu\text{K}$, and $600\mu\text{K}$ for channels 1 through 4 respectively. Since the MSAM I (1992) secondary has a period much shorter than 6 minutes, we expect very little contribution to our demodulated signal from porpoising. However, a power spectral analysis of the pressure sensor shows power at two additional frequencies: 0.036 Hz ($t=27.8$ seconds) and 0.087 Hz ($t=11.5$ seconds). The integrated power is at least a factor of 100 less than that due to porpoising.

MSAM's observing technique can also place constraints on atmospheric contamination. Since the same region of sky is viewed approximately every minute and then again in 20 minutes, inconsistency of overlapping regions may indicate atmospheric variation. Such regions rule out variations on the 20 minute scale of greater than $50\mu\text{K}$ on average in the lowest frequency channels.

It is possible to make a measurement of the atmospheric brightness temperature from the elevation scans performed during the flight at an altitude of 29 Km. Assuming a simple planar model of the atmosphere, the intensity $I(\nu) \sim T_z \csc(\theta)$ where θ

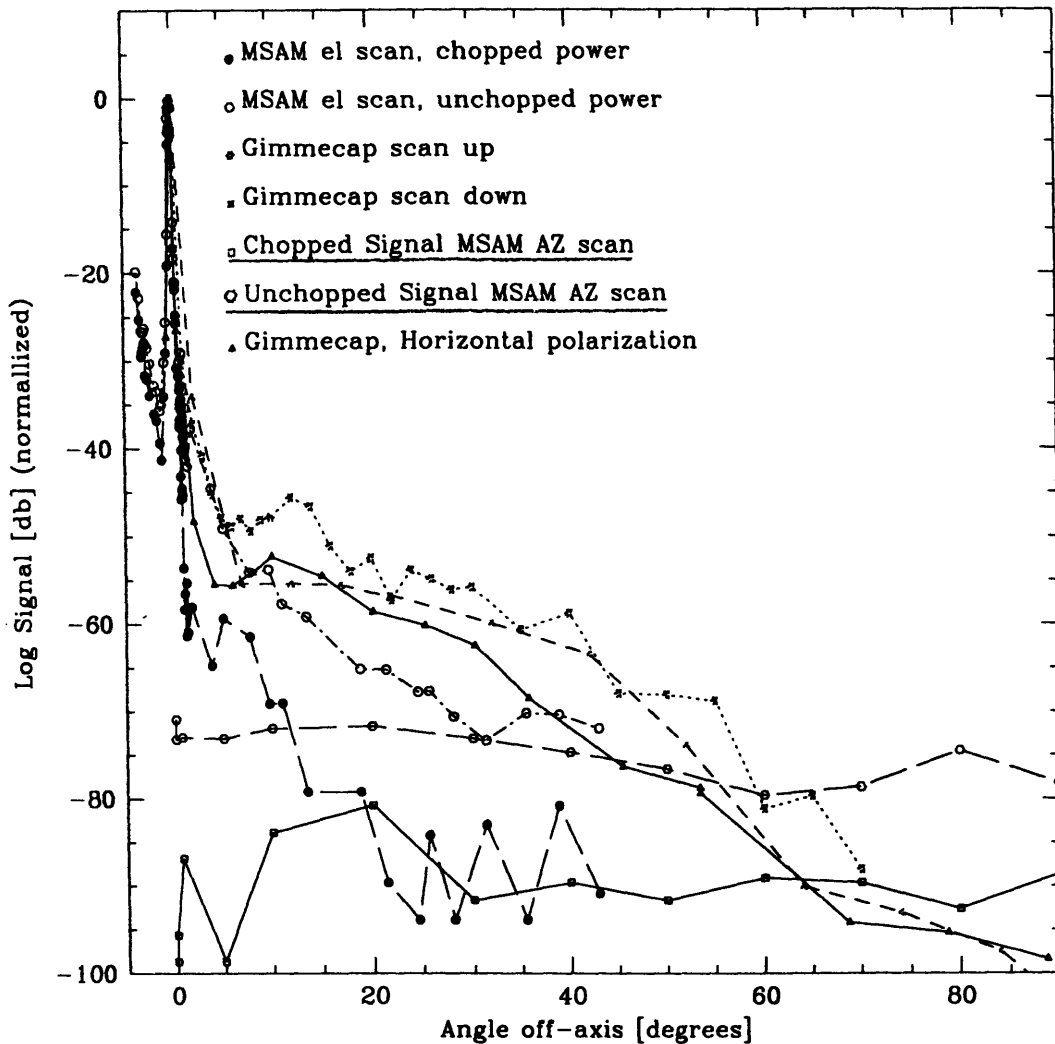


Figure 3-6: During the 1994 Palestine campaign, we used a source nicknamed Gimme-cap to map the sidelobe response of MSAM I (1994) which has a new top configuration. The chopped MSAM AZ (azimuth) scan provides a *best case* scenario for the MSAM I 1992 design. The other data are not directly comparable to the MSAM I 1992 gondola.

Table 3.3: Results of Page atmospheric modeling using a computer model developed by Weiss (1979). The bandpass integrals for each channel are shown for an altitude of 35 Km and observing angle of 45° from zenith.

Channel	1	2	3	4
H₂O				
$\frac{\text{Watts}}{\text{cm}^2\Omega}$	2.3×10^{-13}	3.4×10^{-14}	4.2×10^{-11}	6.0×10^{-12}
O₂				
$\frac{\text{Watts}}{\text{cm}^2\Omega}$	5.1×10^{-14}	5.9×10^{-14}	1.0×10^{-10}	6.9×10^{-12}
O₃				
$\frac{\text{Watts}}{\text{cm}^2\Omega}$	1.9×10^{-12}	2.7×10^{-11}	4.1×10^{-10}	6.3×10^{-10}
dPower/dPres_{atm}				
$\frac{\text{Watts}}{\text{mmcm}^2\Omega}$	5.1×10^{-13}	6.3×10^{-12}	1.3×10^{-10}	1.5×10^{-10}
Passband Int.				
$\frac{\text{W}}{\text{cm}^2\Omega\text{K}}$	3.59×10^{-11}	1.80×10^{-10}	4.03×10^{-10}	5.04×10^{-10}
$\delta\nu(\text{cm}^{-1})$	1.32	2.39	1.80	1.20
Predic.dT_{rij}/dPres_{atm}				
$\frac{\mu\text{K}}{\text{mm}}$	142 ± 300	350 ± 300	3200 ± 300	3000 ± 300

is the angle from horizontal and T_z is the zenith temperature. Since the detectors are highpassed, we fit the derivative of a cosecant to the bolometer signal. The measured sky temperatures are in Table 3.4.

Table 3.4: Zenith sky brightness at 29 Km

Channel	1	2	3	4
Sky Temp	350 mK	590 mK	580 mK	740 mK

Altitude Changes

Estimates of the altitude from the pressure sensors indicate that the majority of the flight took place at an altitude of 35 ± 0.15 km. However, the first 45 minutes (first two scans) of the MBR observations were taken while rising the last kilometer. Porpoising caused periodic variations ($\tau \sim 6$ minutes) with an amplitude of ~ 100 meters. Figure 3-7 shows pressure variations throughout the MBR observations.

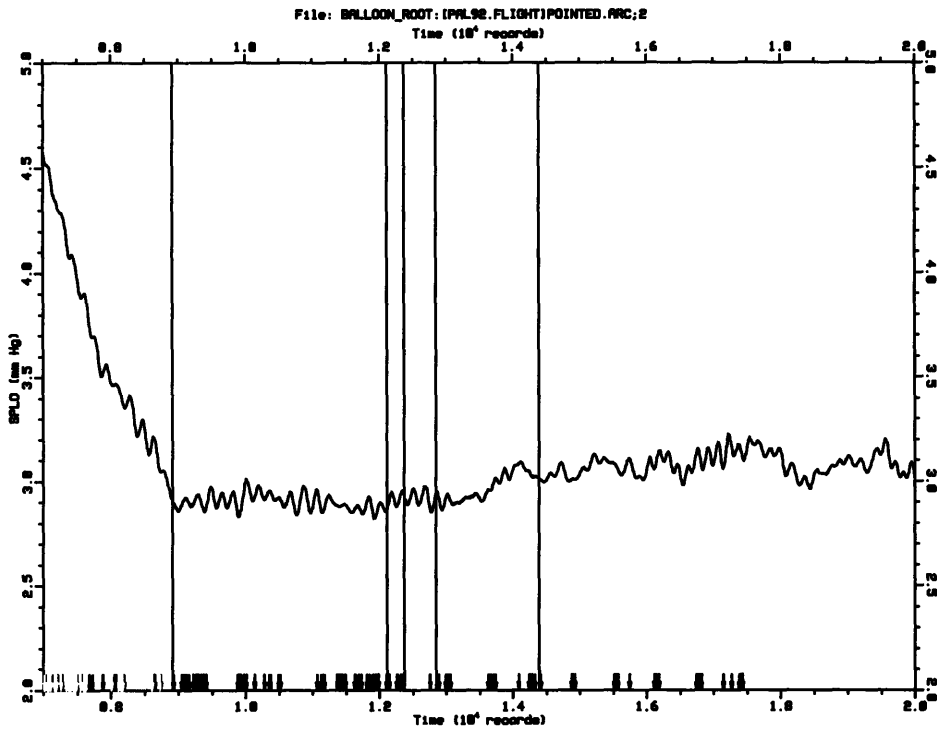
The dynamics of the balloon during flight are described by three oscillation periods seen in the gyroscopes (6 minutes, 27.8 seconds, and 11.5 seconds). The flight line is 330 feet, and a 40 million cubic foot balloon is about 200 feet in radius, so the simple pendulum mode of the balloon and payload is ~ 26 seconds if one assumes the fulcrum is near the center of the balloon. This suggests that as the balloon rises, the swinging modulates the lift rate, and hence, the pressure as a function of time. It is harder to understand the 11.5 second oscillation. It is a much broader resonance implying that it is not just a simple pendulation. It also couples to the pressure sensor and thus may effect the rise rate of the balloon.

A recent test package flown on top of a balloon has demonstrated that the balloon may rock as a simple pendulum with an amplitude of $\sim 0.1^\circ$. However, the MSAM I (1992) magnetometer information leads us to believe the amplitude of the pendulation on the 1992 flight was less than 0.1° .

3.5.3 Other Sources of Spurious Signal

Chopper

The chopper behavior at the low temperature (~ 250 K) and low pressure (~ 3 torr) conditions of float was studied before the flight. A gain change in the position sensor (the LVDT) was observed with decreasing temperature. Since the effect is reproducible, a software correction is implemented in flight and verified with the



27-JAN-93 17:49:24

Figure 3-7: Pressure variations throughout the MBR observations. A pressure of 3 mm corresponds to an altitude of ~ 35 km. The approximate conversion is $\text{Altitude} = -\text{Pres}/1.292 + 37.70$. Porpoising started well before reaching float. The vertical lines are telemetry dropouts.

planet rasters. A suitable gain correction for a particular operating temperature was found from lab tests. In flight, the average mirror temperature as monitored by two Analog Device AD592 temperature sensors determines the correction to any commanded amplitude. The correction is necessary because as the mirror gets colder, the amplitude increases. For a commanded sky throw of 0.7° , the actual amplitude would be 0.75° which is beyond the limits of the actuators.

If the secondary is not balanced, microphonics will become severe when executing a square wave chop. The transition rate for the chopper motion was slowed until 20 minutes of ground integration did not show a detectable microphonic signal. The radiometric loading in flight is smaller, and thus the chopper microphonics are a more significant contribution to the constant offset than on the ground. The observed constant offset is not phase shifted with respect to the chop; that is, maximizing the offset also maximizes the signal. We can not rule out chopper microphonics as the source of our large constant offset.

The chopper moves the beam on the primary by several centimeters. Emissivity and temperature variations on the surface of the primary will lead to an offset in the demodulated data. Estimates of emissivity variation offset are approximately the same as the temperature variation offset. Temperature variations lead to an offset signal of

$$\Delta T_{\text{signal}} = \epsilon_\nu \delta T_{\text{mir}} \times \frac{\Delta x}{\Delta L} \quad (3.1)$$

where ϵ_ν is the mirror emissivity at a frequency ν , δT_{mir} is the change in temperature across the mirror, Δx is the displacement of the beam on the primary, and L is the diameter of the primary. Choosing pessimistic values for the emissivity of 1%, a mirror gradient of 1 K (the largest measured in flight), $\Delta x = 5$ cm, and $L = 1.4$ m the estimated offset is about $400 \mu\text{K}$. The gondola nod modulates the sky signal and reduces this offset in the final data set by about a factor of 10. Averaging adjacent scans will additionally reduce this effect. The contribution to the sky binned data is expected to be less than $< 30 \mu\text{K}$.

Temperature Drifts

Eighteen temperature sensors (Analog Device AD590) are used to monitor the drifts and gradients in the surface temperature of the primary mirror, secondary mirror and ground shield. Their relative accuracy is 0.1 K while the absolute is 1 K. Since the MSAM I ground shields cover many square meters, the long thermal diffusion time can lead to significant temperature gradients. To reduce these gradients in the ground shield, the polyisocyanurate foamboard frame is covered in 0.012 inch aluminum. At float the air temperature was 235 K. The package cooled at a nearly uniform rate of 1.25 K/hr having reached float at $T \sim 250$ K.

The temperature variations which are synchronous with the chopper are removed from the demodulated data with a slow spline. This procedure as well as the simple correlation coefficients between these temperature data and the demodulated data are discussed in the next chapter.

Upper Structure

Reflection and emission from the upper structure of the gondola is a concern in this flight. Tests with a sighting laser indicate no direct reflections from the top structure, off the secondary, and into the dewar, as was the design intention. It was necessary to design the ground shield with a trough between the dewar and the secondary to prevent single bounce reflections from the upper structure.

The total power contributed by the top structure is estimated by integrating the signal which is in excess of the best fit cosecant found from the elevation scan. These power estimates, Figure 3.5, follow the same pattern as beam spillover at the secondary.

Table 3.5: Power estimates (unchopped) from gondola top structure and beam spillover at secondary.

Channel	1	2	3	4
Top Power	4100 mK	490 mK	50 mK	200 mK
Spill %	11%	6%	3%	4%

Although the balloon is far from the main beam, it will contribute a small constant offset. The balloon fills ~ 0.114 steradians as seen by the telescope whereas the beam size is about 5×10^{-5} steradians. Assuming 1% contrast of the half degree scale, an emissivity of 1%, and that the balloon surface temperature is randomly distributed, an antenna response of -50 dB leads to a $20 \mu\text{K}$ offset.

The balloon could also contribute a time variable offset to the final data set. One can imagine a case where one of the balloon vent tubes remains stationary with respect to the sky. These fill tubes are the part of the balloon vent that would have been closest to the gondola. The tubes fill 1.5×10^{-3} str as seen from the telescope. It would be impossible to account for spatial features smaller than our beam in this way. In addition, the vent tubes are nearly 18° from the main beam. If the balloon is 1% emissive then only 50 dB of rejection is required – this is likely 18° from the mirror. If, on the other hand, there is 5% reflection off a small strip of vent tube about the same size as the beam (e.g. the edge), a -60 dB response would be necessary. We have no way to rule this possibility out since the appropriate sidelobe information is lacking; however, it seems unreasonable to expect phase synchronous motion between

the balloon and the gondola. Furthermore, in the 1994 reflight of MSAM, the vent tubes were tied back and similar spatially small structure was seen.

Cosmic Ray Strikes

A large number of protons and alpha particles strike the Earth's upper atmosphere with typical energies below 1 GeV/nucleon. There are about $30 \frac{\text{gram}}{\text{cm}^2}$ of metal above the bolometers to impede cosmic rays. This will cause secondary production consisting mostly of electrons and photons. Typical flux rates from the empirical models [50], [7] for particles $> 200 \text{ MeV/amu}$ are predicted at about $2 \times 10^3 \frac{\text{events}}{\text{m}^2 \text{sec} \Omega}$. Typical solar flares may increase this to 3.5×10^3 . The MSAM I (1992) detectors are 5 mm x 5 mm which implies a primary particle flux rate from the sky of about one glitch every 4 or 5 seconds. Production of secondaries will increase this rate.

Analysis of the data yields a rate of one event every few seconds. There is no lower cutoff seen in the level of hits. Since they occur at random and the larger strikes are easily removed from the data, the result is an increase in noise.

Glitches

In addition to cosmic ray hits, MSAM I (1992) experienced *glitches* which had the signature of popcorn noise. These glitches are correlated to events in the pressure sensor suggesting that there was an electronic problem contributing to the detector signal. Unfortunately, neither the sensitivity nor the sampling rate of the pressure sensor make it possible to reliably remove a model.

The severity of the strikes decreases with increasing channel frequency. Also, the glitches occur in clumps rather than randomly in time. Both cosmic ray hits and these glitches are dealt with in a similar fashion which is described in the next chapter. After *deglitching*, the distribution of samples is approximately Gaussian with truncated ends, implying that the removal of both types of glitches is satisfactory.

Chapter 4

Data Analysis

4.1 Overview of Technique

In the June, 1992 flight of MSAM I, there are 4.7 hours of MBR data covering a range of RA from 14.44 to 20.33 (J1992.5) hours at a declination of approximately 82 degrees. The first six scans and the last eight scans are analyzed separately since they were separated by the Coma observation and thus the offset may differ. The natural way to view the data within a 20 minute scan is to form groups in time according to the secondary mirror's chopping cycle. Each full 0.5 second period of the chopping secondary is comprised of 16 bolometer samples. Any group of 16 data points comprising a chopper cycle is denoted as a *template*. A group of four secondary chopper periods (4 templates) is called as a *record*. Analysis of the data beginning with the raw time stream proceeds as follows: (1) remove model transfer function from raw data (2) remove average chopped offset from the time stream (3) perform iterative RMS cuts on data to remove glitches (4) demodulate at chopper frequency and chosen phase (5) remove slowly varying drifts in time (6) bin data by position on the sky (7) spectrally decompose signal using a two component model (8) set model dependent limits on amplitude of fluctuations using a likelihood statistic. The following pages will describe these steps in detail.

4.2 The Transfer Function and Deglitching

This section describes the procedure for removing cosmic ray strikes (and other glitches) from the data with minimal cutting of the data and minimal introductions of correlation between samples. The top plot of Figure 4-2 shows what a typical cosmic

ray strike looks like in the time series data. Since cosmic ray strikes occurs on time scales much less than time constant of our detectors ($\sim 50 \text{ ms}$), they can be used to measure the response of the electronics to a delta function in power received at the bolometers. The Fourier transform of a cosmic ray strike gives what is called the electronic transfer function. The shape of this function is described below.

The parameters of the transfer function for each channel are determined by fitting to the Fourier transform of the time data containing a single cosmic ray strike¹. This fit is performed for several typical cosmic ray strikes. Once determined, the transfer function for each channel is removed from all of the data in a flight half by dividing it out of the Fourier transform of the raw time series. The data are subsequently returned to the time series. Most cosmic ray strikes which previously affected 10 or more adjacent samples, now contaminate only three or four adjacent samples and are easily removed.

The following transfer model is assumed for signals originating at the bolometer:

$$T = \frac{1}{1 + i\omega\tau_l} \times \frac{i\omega\tau_h}{1 + i\omega\tau_h} \times (\text{EllipticFilter}), \quad (4.1)$$

where the parameters τ_l and τ_h are low and highpass time constants and *Elliptic Filter* denotes the transfer function of the elliptic lowpass filter described below. A plot of the power spectrum of T is shown in Figure 4-1.

The transfer function is the result of combining a highpass and lowpass RC filter, the elliptic lowpass filter, and a phase shift described below. The RC lowpass is due to the thermal time constant of the bolometers. An AC coupling stage in the external preamplifier gives a highpass filter on the bolometer signal. There is a four pole elliptic lowpass filter in the Main Electronics Box which removes high frequency microphonics to which the detectors are sensitive. The filter is specified by the passband edge, the stopband edge, maximum passband attenuation, and minimum stopband attenuation and does not have a convenient analytic form. For more information see [30], and [26].

To model a specific glitch, the data is fit to:

$$\tilde{T} = T \times A \times e^{i\phi}. \quad (4.2)$$

where A is the amplitude of the glitch and the phase shift term accounts for the fact that an impulse strikes at some time δ into the sample integration. T has 6 filter related parameters, so the fit to \tilde{T} has 8 parameters. The third plot in Figure 4-2 shows the time series residuals from a best fit model subtracted from a typical glitch. It is assumed that the electronics-induced glitches and the cosmic ray strikes are both

¹Each half of the flight is analyzed independently at first, but only one transfer function is assumed for each channel throughout the flight.

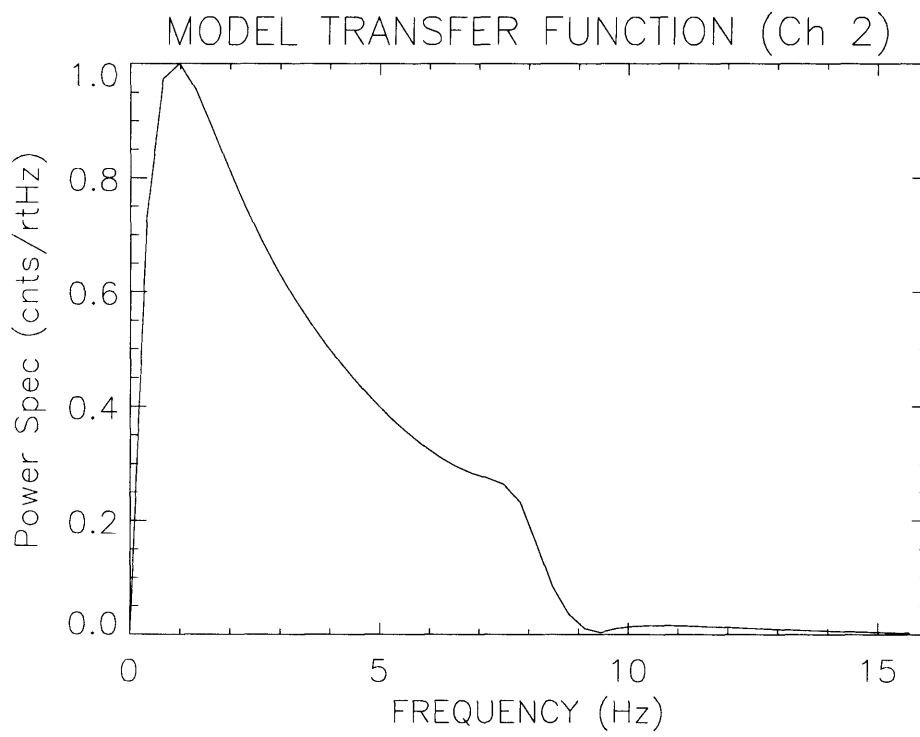


Figure 4-1: A linear plot of the modulus of the channel 2 model transfer function.

fit with the same model.

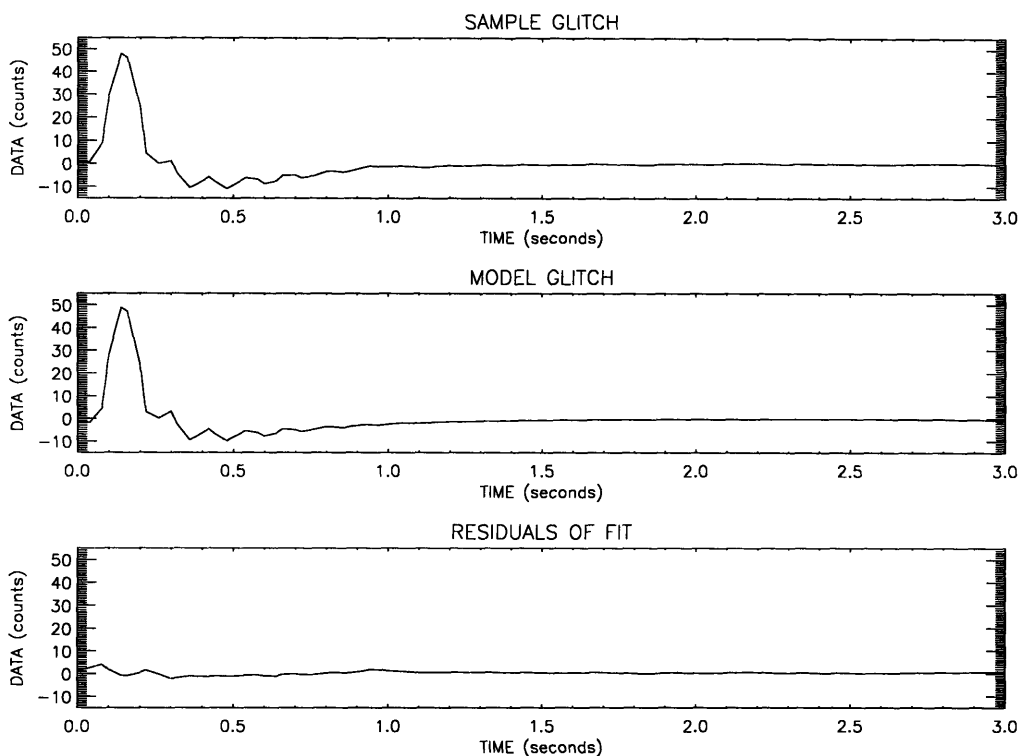


Figure 4-2: The glitch modeling results for a particular example. The residuals are at the approximately 10 percent level.

The elliptic lowpass filter attenuates 20 dB after 10 Hz. Although a white spectrum is obtained from the data after removal of the transfer function, the information beyond 10 Hz is dominated by amplified instrument noise. The first pole of the filter is at ~ 9.2 Hz. Information in the region near this pole is lost. For these reasons, all information above 8 Hz is discarded in the analysis by truncating in frequency space with a soft edge filter at 8 Hz.

The rms cutting occurs on the data with the model transfer function removed. In this space, a moderate size glitch occupies approximately one quarter of the samples it did before the model was removed. Due to the 8 Hz resolution of the model, there is a characteristic high frequency ringing which can be seen in the data about a glitch. This effect can be significant in large amplitude strikes and leads to the cutting of a much larger region of data for such strikes.

A consequence of removing the transfer function is that there are singularities at 0 and 16 Hz. A flat top window function with Gaussian tapered ends is used to smoothly unweight the singularities without changing the spectrum near the demodulation frequencies. The width of the Gaussian near 0 Hz is less than 0.3 Hz (as determined by the AC coupling in the electronics) and the width near 16 Hz is 1 Hz (but arbitrary).

Removal of the transfer function also removes the arbitrary DC level of the time stream. To facilitate the search for cosmic ray strikes, it is useful to remove a global constant offset template from the data. The telescope sees different but nearly constant signal at a given telescope elevation for each of the 16 chopper phases throughout the flight. The size of the chopped offset ranges from 18 mK in channel 1 to 7 mK in channel 4. Possible sources of this offset are discussed in Chapter 3.

Table 4.1 summarizes the global constant offsets removed (both halves of the flight are comparable in magnitude). Listed are the results for the double (*dd*) and single (*sd*) difference demodulation as well as the same for the quadrature (90°) demodulation. The results are consistent with the left beam of the telescope viewing more power than the right beam. Figure 4-3 shows the global constant offsets removed for the first half of the flight for all four channels. The offset templates look rounded since deglitching lowpasses the data at 8 Hz.

Table 4.1: Summary of the flight-averaged constant chopped offsets (in mK) removed for channels 1–4 (c1,...,c4).

	dd	sd	dd 90°	sd 90°
C1	16	18	0.02	0.16
C2	8	8	0.32	0.12
C3	7	8	0.25	0.01
C4	7	8	0.06	0.06

To calculate the template, two iterative 2.5σ cuts are performed on all of the data from each of the 16 chopper cycle samples (or *phases*). These cuts simply flag the data as not to be used in calculating the average but do not discard the data for later use. The average template is then removed from the time stream. After removal of this constant offset template, the global averages of the data from each of the 16 samples of the chopper are zero.

Once this template is removed, two iterative 3.5σ cuts are performed on the time series. Here, σ is calculated from the entire time series of the data. This time, the cut data are flagged (i.e. set the weight to zero) so as not to be used in future analysis. For each cut point, the two adjacent points are also cut to account for the broadness of a glitch.

Channel 1 is affected the most due to the severity of the electronic glitches. The data loss is highest for channel 1 at 7% and decreases with channel to $\sim 3\%$ for channel 4. Figure 4-4 shows the histograms of the predemodulated data after deglitching as well as the best fit Gaussian model assuming uniform weighting. The spectra are approximately white. The residuals to the fits are shown in Figure 4-5.

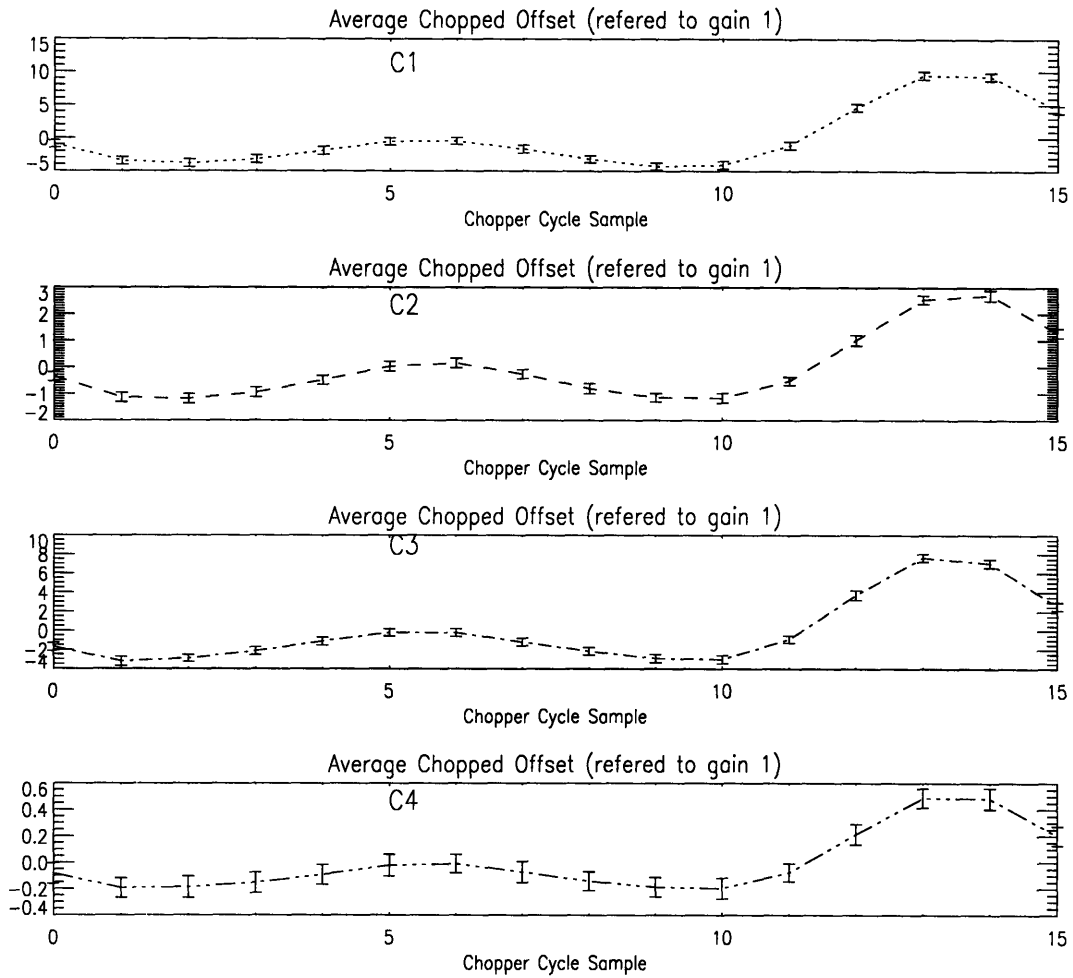


Figure 4-3: The global chopped offsets for the first half of the flight for each channel and referred to electronic gain 1. Each sample is a 1/8 second integration of a detector. Chopper cycle sample 0 is the integration for the first 1/8 second of the center position of the chopper cycle. The last four samples correspond to when the chopper has thrown the beam to the telescope's left.

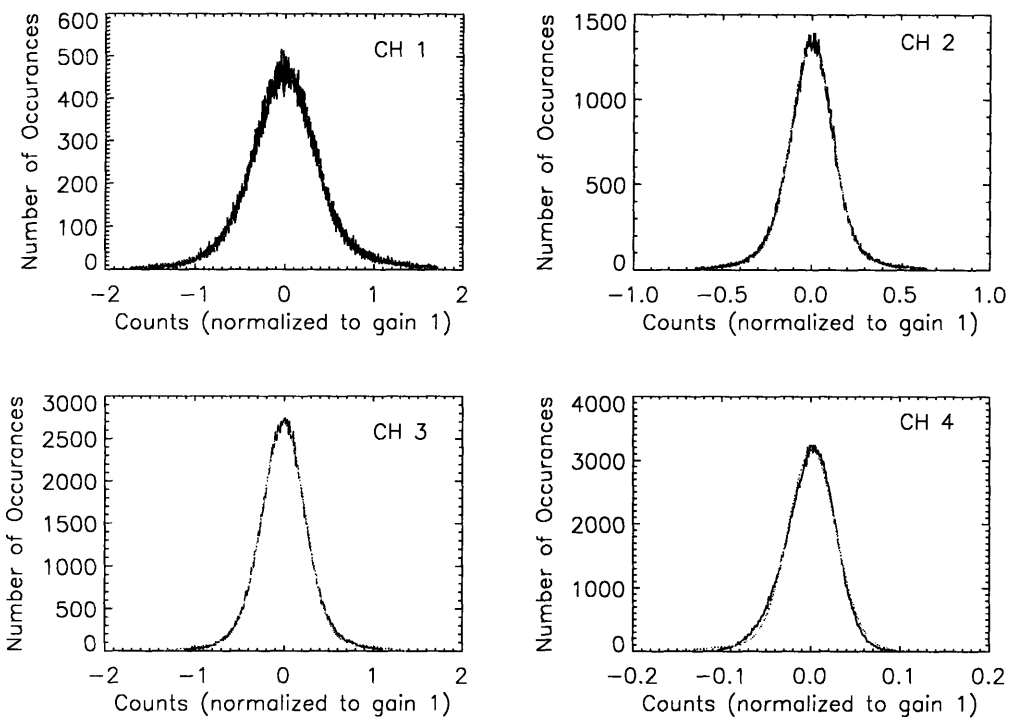


Figure 4-4: Histograms of predemodulated data for each of the four channels. Line represents the best fit Gaussian.

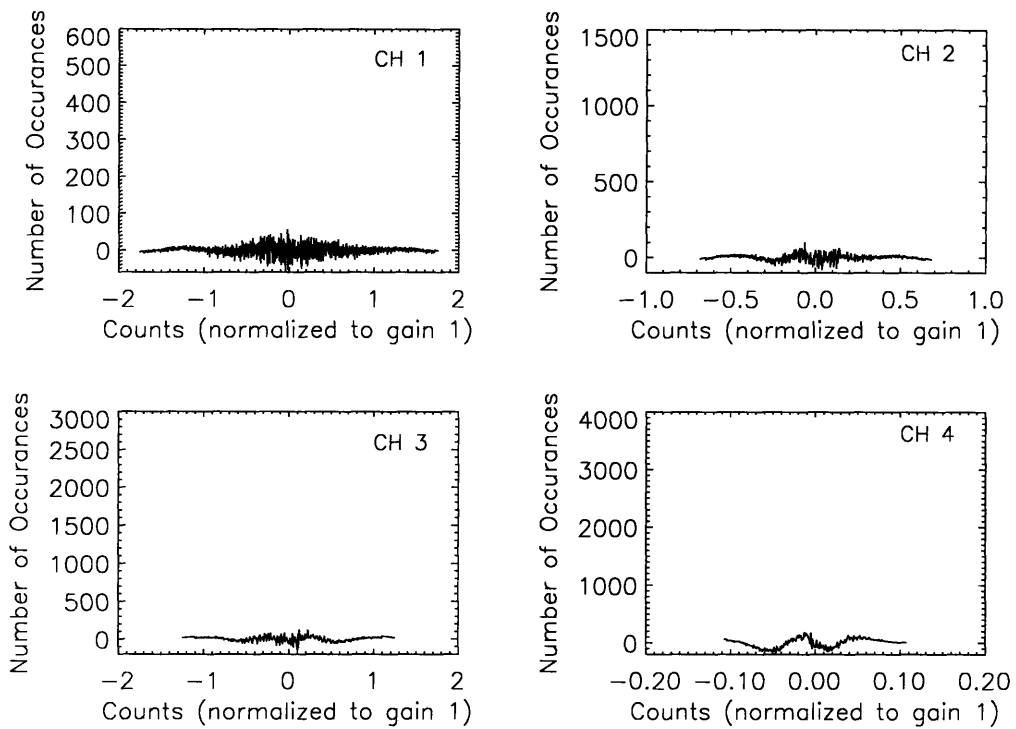


Figure 4-5: Residuals of the Gaussian fit to the histograms of the predemodulated data for each of the four channels.

4.3 Demodulation and Calibration

After deglitching, analysis continues on the data with the model transfer function removed. The advantage is that correlations within the demodulation bandwidth are reduced. This simplifies error analysis and demodulation by reducing the dependence on the covariance matrix.

MSAM I (1992) relies on Jupiter as its primary calibration source. Jupiter was 36 arcseconds at the time of the flight and is small enough to be considered a point source in our half degree beam. Saturn, whose brightness temperature in our bandpasses is not as well known, acts as a secondary calibration. The inclination of the rings is thought to make up to a 15% difference in the brightness temperature of Saturn. Table 4.2 shows the characteristics of both planets ² [19],[23]. Data from the observations of Jupiter are used to construct two *demodulation templates* as described below. Details on the conversion from time series counts to kelvin is given in Appendix A.

Table 4.2: Characteristics of MSAM I (1992) calibration sources at the time of flight.

Planet	Brightness Temperature (Kelvin)				
	Ch 1	Ch 2	Ch 3	Ch 4	Angular Size
Jupiter	172.5 ± 1.4	169.9 ± 5.1	147.5 ± 5.8	148.5 ± 4.9	2.254×10^{-8} str
Saturn	unknown	135 ± 4	130 ± 5.8	112 ± 3	5.33×10^{-9} str

The demodulation templates are constructed as follows. Four 16 point data templates are measured where Jupiter is either in the center of one of the three antenna lobes or not present in any lobe. These templates are denoted as J_c , J_l , J_r , and J_o where the last letter means *center*, *left*, *right*, or *off*, corresponding to the position of Jupiter with respect to the antenna pattern. The double difference dd and single difference sd templates are created as follows:

$$\begin{aligned}
 dd &= (J_c - J_o) - (J_l - J_o) - (J_r - J_o) \\
 &= J_c + J_o - J_l - J_r
 \end{aligned}
 \tag{4.3}$$

and

$$\begin{aligned}
 sd &= (J_r - J_o) - (J_l - J_o) \\
 &= J_r - J_l
 \end{aligned}$$

From dd , all antisymmetric components are removed in the Fourier domain only that signal synchronous with the secondary chop is included. The zeroed components are

²Data from measurements at NRAO, UKIRT, IRTF, and IRIS.

less than 1% of the signal at 4 Hz for the double difference, and are less than 1% of the sum of signals at 2 and 6 Hz for single difference demodulation. The DC component is already zero. The quadrature templates are created by shifting dd by 2 points and sd by 4 points corresponding to a 90° shift in each. No sky signal should appear in the data demodulated with the quadrature templates. Thus, there are 2 statistically independent demodulation schemes. The templates (i.e the lockin waveforms) for channel 1 are shown in Figure 4-6.

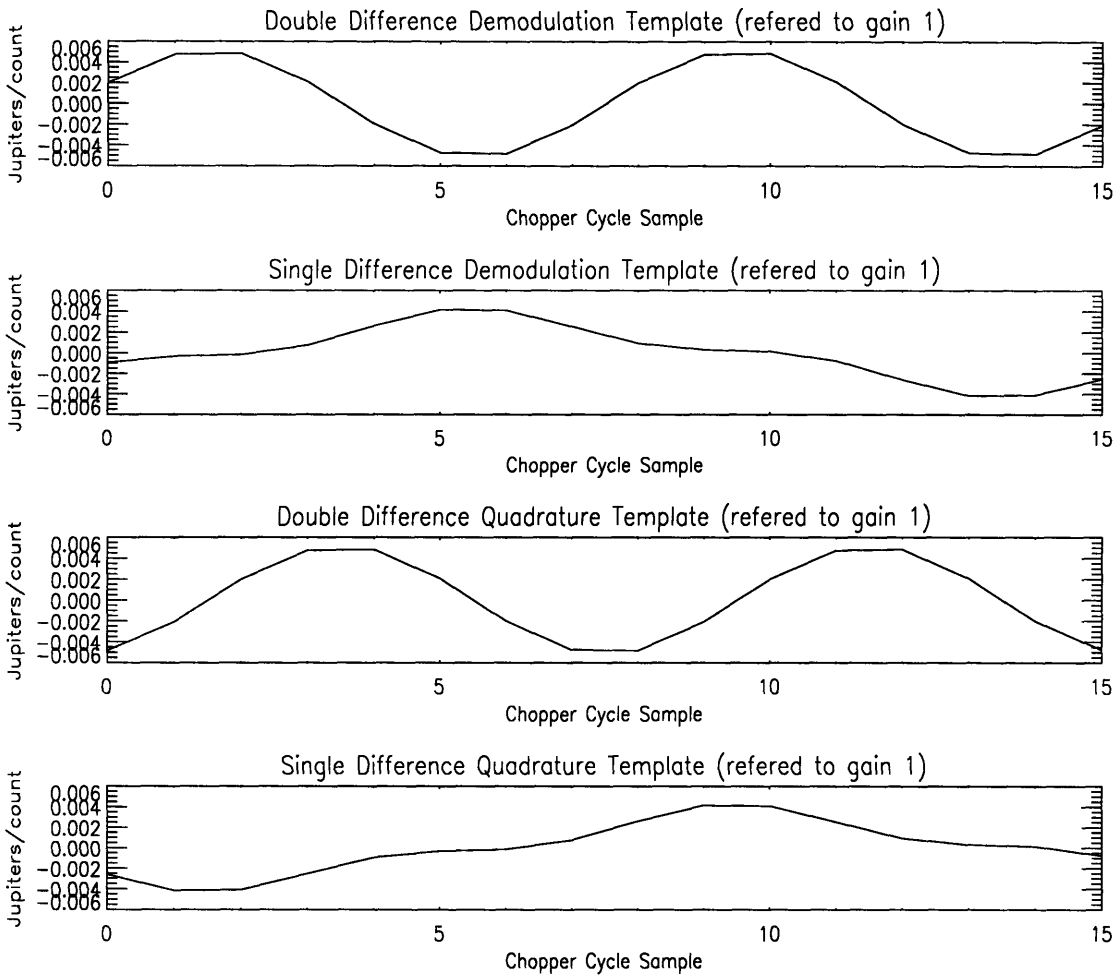


Figure 4-6: The lockin waveforms used for demodulation of the time stream. The vector comprised of the 16 samples of a detector in a chopper cycle (i.e. the average signal template) is dotted into the above waveforms to obtain the double and single difference demodulated data as well as the same in the quadrature phase.

Raster resolution, the uncertainty of the brightness temperature of Jupiter, and the instrument noise mean the calibration uncertain to 10%.

The first step toward demodulating the data set after deglitching is to phase average the four chopper cycles in a record, producing one 16 point vector per record (the *average signal template* – see Equation 4.4). If any phase of the average signal template contains more than 3 flagged points or if the entire record has more than 25% of the data flagged, then the entire record is cut. This prevents ringing near large glitches from dominating the resultant average. The *dd* or *sd* template is then dotted into each average signal template a_k (Equation 4.5). The correlation matrix for the in-phase single and double difference data is shown in Figure 4-7. The small correlations between *sd* and *dd* data demonstrate the statistical independence of the two demodulation schemes.

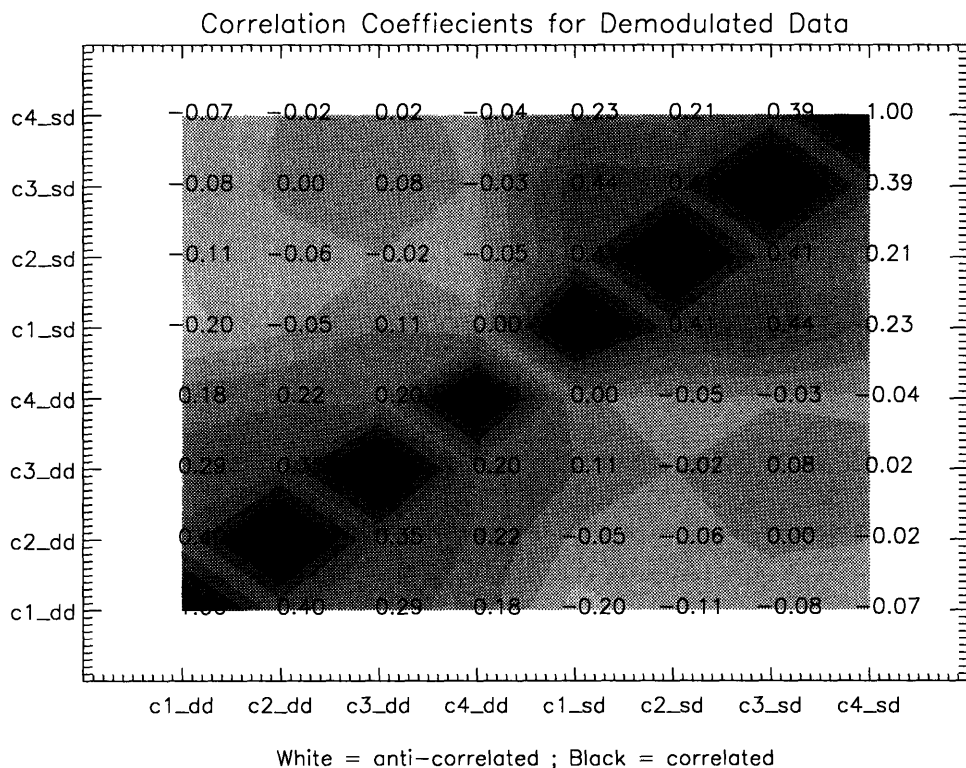


Figure 4-7: The Pearson correlation coefficients for the demodulated data BEFORE drift removal.

4.3.1 Noise Estimates

The variance on the demodulation dot product is found by contracting over the covariance of the data. First, the average 16×16 covariance matrix $C_{k,l} = \langle x_k, x_l \rangle$ of the raw data is found from 100 record long (200 seconds) regions of data containing

no cut even after deglitching. The average signal template a_k is formed by the sum

$$a_k = \sum_{i=0}^3 \frac{x_{k+16i}}{n_k} \quad (4.4)$$

where n_k is the number of points used in the average. A demodulated value d for a record is the dot product between the average signal template and either the single or double difference demodulation template. Using J to represent a demodulation template:

$$d = \sum_{k=0}^{15} J_k a_k \quad (4.5)$$

The variance of d is

$$\langle d^2 \rangle = \sum_k \sum_l J_k J_l \langle a_k a_l \rangle \quad (4.6)$$

$$= \sum_k \sum_l \frac{J_k J_l}{n_k n_l} \sum_{i=0}^3 \sum_{j=0}^3 C_{k+16i, l+16j} \quad (4.7)$$

Again, this is a restricted sum where flagged points are not included. The demodulation templates J are assumed noise free. Since correlation for lags greater than 16 is generally less than a few percent, when $|k - l| > 16$, C is set to zero. Figure 4-8 shows the autocorrelation vectors used.

If the phase of the data with respect to the chopper is incorrect, sky signal is lost during the demodulation. The planet rasters are used to phase-up the data with respect to the demodulation templates. For each channel, a phase is found which maximizes χ^2 of the demodulated response when rastering over the planets. An equivalent condition is that the χ^2 of the quadrature demodulated response is minimized. No phase shift was required to achieve this condition for either the Jupiter or Saturn rasters. Phasing during these times is better than 2%.

4.3.2 Gain Drift

The ratio of the demodulated response to Jupiter to the demodulated response to Saturn indicates a gain drift in channel 2 during the course of the flight. The response ratios are consistent with previous literature values in all channels except for channel 2 where a factor of 1.81 is present. This factor is consistent with a linear gain decrease in both the rms noise level and the change in the chopped offset template (i.e. J_o).

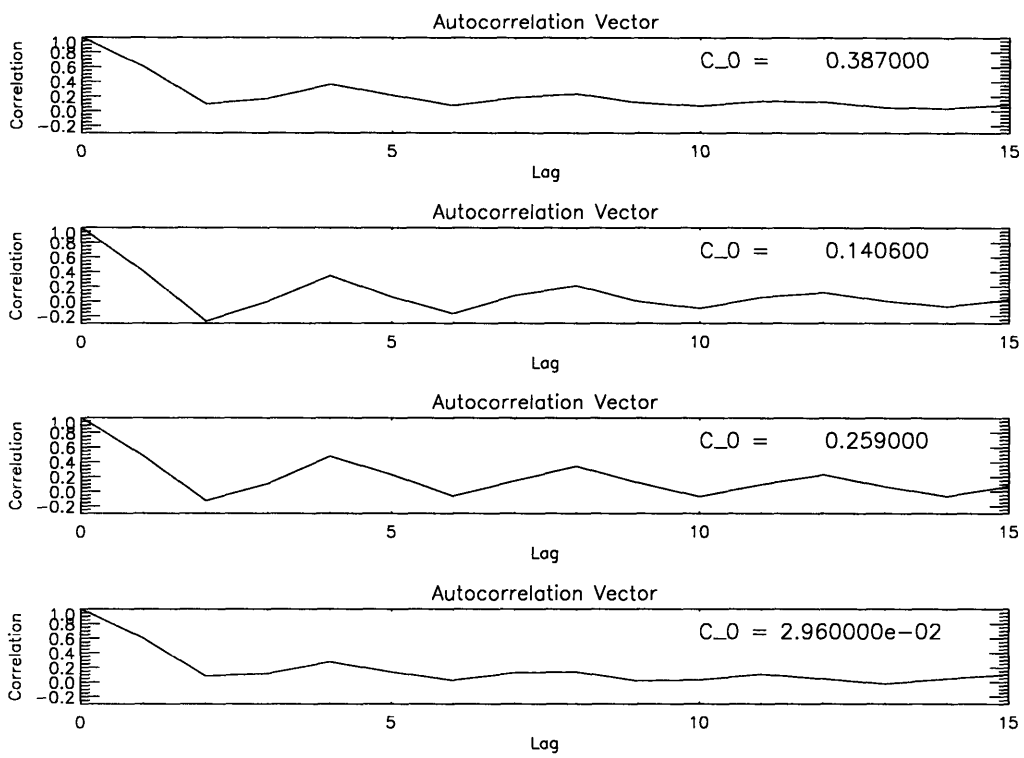


Figure 4-8: Autocorrelation vectors for the four channels as a function of sample lag.

A multiplicative gain factor, linear in time, is applied to the channel 2 time stream before demodulation to remove this effect. The origin of the gain drift is not known.

4.4 Dealing with Other Systematic Error Sources

To assess the degree of correlation between the demodulated data and the pressure, temperature and position sensors mounted on the experiment, a best fit regression is performed. Fitting is done with an IDL routine based on the multiple linear regression program outlined in Bevington [5].

Correlation is mainly in the form of long term (i.e. greater than 20 minutes) drifts which are expected from elevation changes. To remove long term drifts from the data, a piecewise continuous spline which minimizes the variance within each sky bin is subtracted. That is, since we expect the signal on the sky not to vary with time, we remove the signal in the data which drifts slowly in time at a fixed sky coordinate. The subtracted function is a cubic spline with knots every 2.5 minutes. Each channel and demodulation is treated separately as is each half of the flight. The drift is significant at the 3 to 8σ level. The χ^2 per degree of freedom for these fits ranges from 0.92 to 1.21. The statistics for the regression before and after dedrifting (i.e. removal of the slow splines) are shown in Appendix D. The effect of dedrifting on the correlation coefficients of the demodulated data is shown in figure 4-9.

4.5 Binning of Data

The RA, declination, time of day, and gondola position are used to project the sky observation location of each demodulated data point onto a flat, rectangular coordinate system centered where the telescope was observing at that time. Each demodulated point is then labeled by an x , y and $twist$ coordinate in this new coordinate system. The conversion is as follows.

Each data point has a right ascension α and declination δ associated with the location of the infrared beam center as determined from the star camera and gyroscope information. To convert to approximately flat sky coordinates we use

$$\begin{aligned} x &= \cos(\delta) \cos(\alpha) \\ y &= \cos(\delta) \sin(\alpha) \end{aligned} \tag{4.8}$$

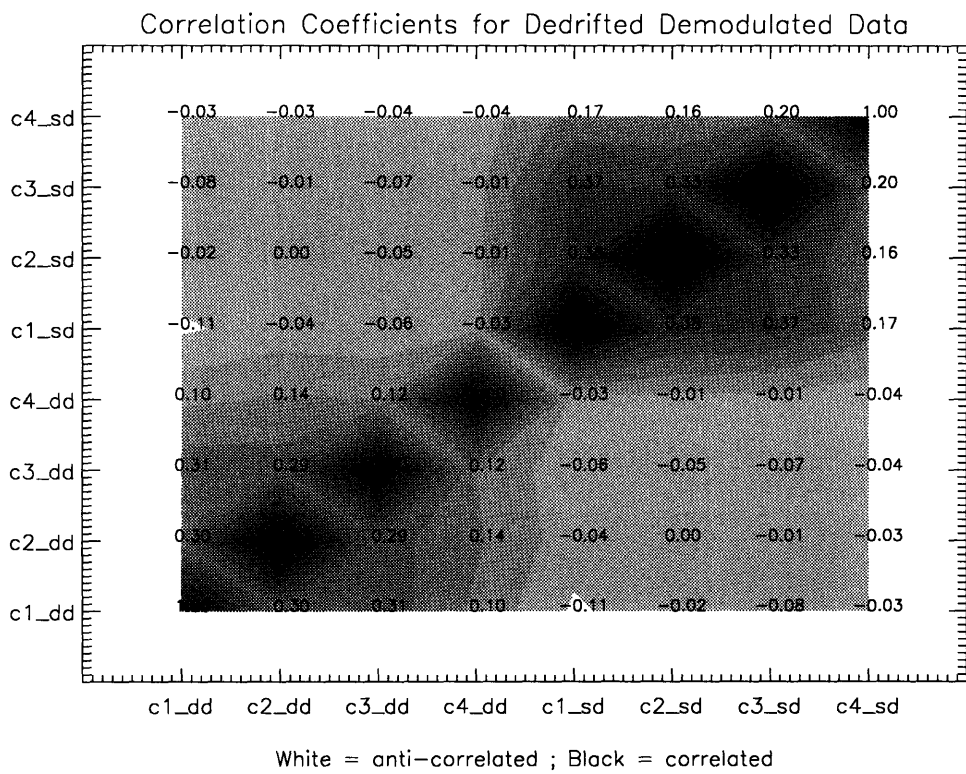


Figure 4-9: The Pearson correlation coefficients for the demodulated data AFTER drift removal.

$$twist = s + \arctan\left(\frac{\sin(\lambda) \cos(\delta) \cos(l) - \cos(\lambda) \sin(\delta)}{\cos(\delta) \sin(l) \sin(\lambda)}\right) \quad (4.9)$$

where s is the local sidereal time, λ is the latitude, and l is the local hour angle. Twist represents the rotation of the antenna pattern on the sky as the sky rotates. Specifically, it is the angle between the line through the centroids of the antenna pattern lobes and the local tangent to the circle of constant declination at the infrared center.

The data bin size is 0.12° in x and y , and 10° in twist orientation. Records whose signal value differs from the median value in that bin by more than 3σ are removed. All bins contain 10 or more records. To check the consistency of overlapping regions from different scans, we check the χ^2 of the binned data with each bin mean subtracted. The reduced χ^2 are between 0.88 and 1.04 for all channels and both demodulations. This implies that scan overlap is consistent with noise and is not greatly contaminated by atmospheric changes on the 20 minute time scale. A total of 14% of the data have been cut as of this point.

Figures 4-10 and 4-11 show the binned data plotted in RA for both demodulation schemes after smoothing by a factor of 4. All subsequent analysis is carried out on the data without smoothing. The cut level has a slow effect on the data. If, for example, the rms cutting which involves two 3.5σ cuts were increased to two 4σ cuts, the overall structure remains largely the same but the error bars are $\sim 10\%$ larger. Making iterative cuts progressively less than 3σ reduces the total variance as a slow function of σ . The current cut level was chosen by determining where the number of cut points became a moderately fast function of σ in channel one (our most cut-sensitive channel due to the glitches).

4.6 Sensitivity

Table 4.3 lists the achieved and theoretical sky sensitivity based on a bolometer model developed at MIT for the MSAM I (1992) and first FIRS flight. Since the detectors and filters have changed little³, a direct comparison is possible. Generally, MSAM I (1992) should be a factor of two more sensitive than FIRS. The apparent loss in sensitivity in channel 1 and 2 may be due to the excess electronic glitches. Channels 3 and 4 are predicted to be dominated by atmospheric noise in both experiments. Channels 1 and 2 were dominated by offset variation due to altitude changes in the FIRS flight. In MSAM I (1992), glitches are a dominant noise source for the first two channels.

³The cryogenic chopper in FIRS was replaced with a 10 cm^{-1} lowpass filter.

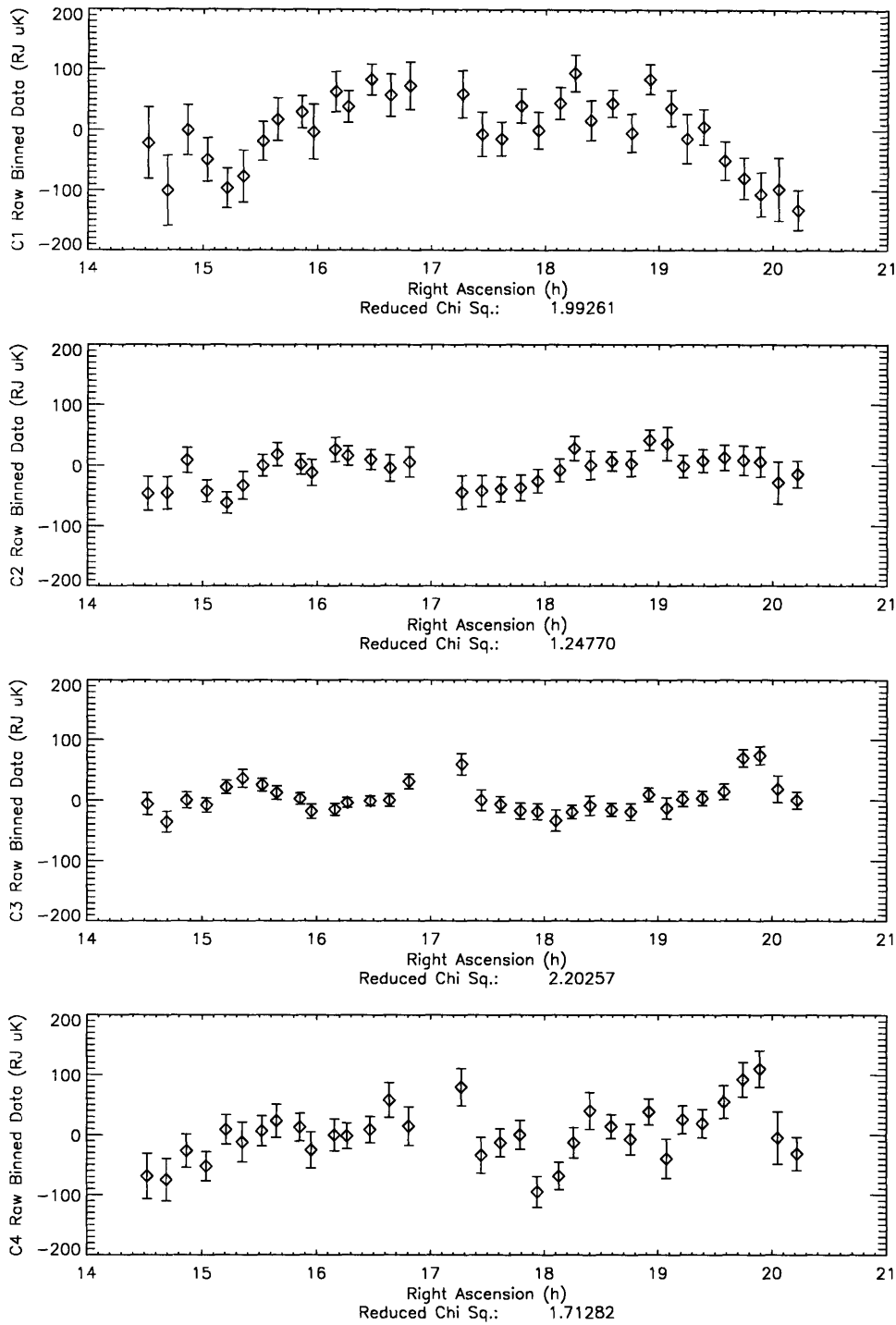


Figure 4-10: The MSAM I (1992) single difference data binned in sky coordinates but smoothed and plotted in RA . Channel 1 (5.6cm^{-1}) is plotted first followed by the other channels. The y-axis is in units of Rayleigh-Jeans temperatures.

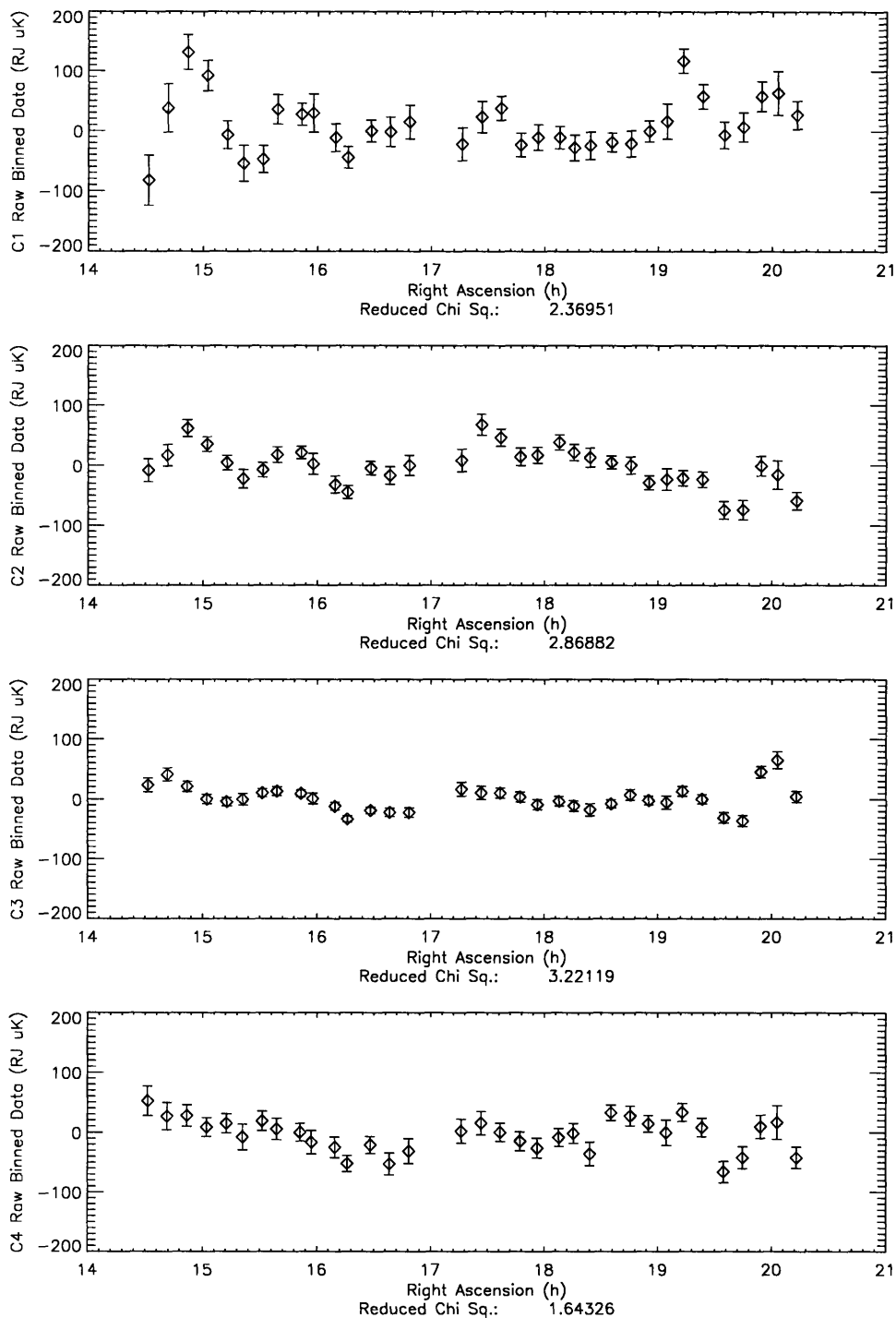


Figure 4-11: The MSAM I (1992) double difference data binned in sky coordinates but smoothed and plotted in RA . Channel 1 (5.6cm^{-1}) is plotted first followed by the other channels. The y-axis is in units of Rayleigh-Jeans temperatures.

Table 4.3: Sky Sensitivities ($\mu\text{Ksec}^{1/2}$)

FIRS				
Channel	1	2	3	4
Ideal RJ w/o atmosphere	330	160	27	180
Achieved (1st flight)	600	280	580	1300
MSAM I (1992)				
Achieved	400	210	140	330

4.7 Quadrature Data

A check of the analysis pipeline as well as the phasing during MBR scans is performed by analyzing the quadrature data (i.e. the time stream shifted by 90° with respect to the demodulation template). A 15° shift removes some of the correlation between the channel 1 in-phase data and the quadrature data. In no channel is a shift larger than 15° required. This amount is well within the accuracy of the previous phasing technique. Constructing quadrature beam maps of Jupiter and Saturn show that all channels and demodulations are phased-up to better than 2%. There is no evidence of chopper phase or offset wander. There is also no indication that the constant offset is changing phase by this amount. Since a 15° shift amounts to less than 4% signal loss, we choose to not use this shift in further analysis. Given the evidence, however, we cannot be sure of long term phase stability to better than 15% over the flight. The smoothed quadrature data is plotted in Figure 4-12 and 4-13. The smoothed quadrature data but phase shifted by 15° is plotted in Figure 4-14 and 4-15.

The range of reduced χ^2 for the sky binned quadrature data is between 0.83 and 1.3 for all demodulations and channels. The largest values are in the channel 2 and 4. These numbers are slightly deceiving since there is point to point signal correlation in the binned quadrature data. This correlation is mostly apparent in the single difference data. This drift could be a symptom of a problem with sidelobe response. However, the recent reflight of MSAM I in June of 1994 (with much less upper gondola structure) measured the same region of the sky and also shows significant correlation between the in-phase binned data sets even with similar drift and offset problems.

4.7.1 Expected Foreground Sources

The placement of the MSAM I (1992) channels allows us to see the spectral rollover of the MBR signal at 6 cm^{-1} . The power from a $T=2.7\text{ K}$ black body signal will dominate in the 5.6 cm^{-1} channel. Warm ($T=20\text{ K}$) dust and atmosphere will dominate the 16.5

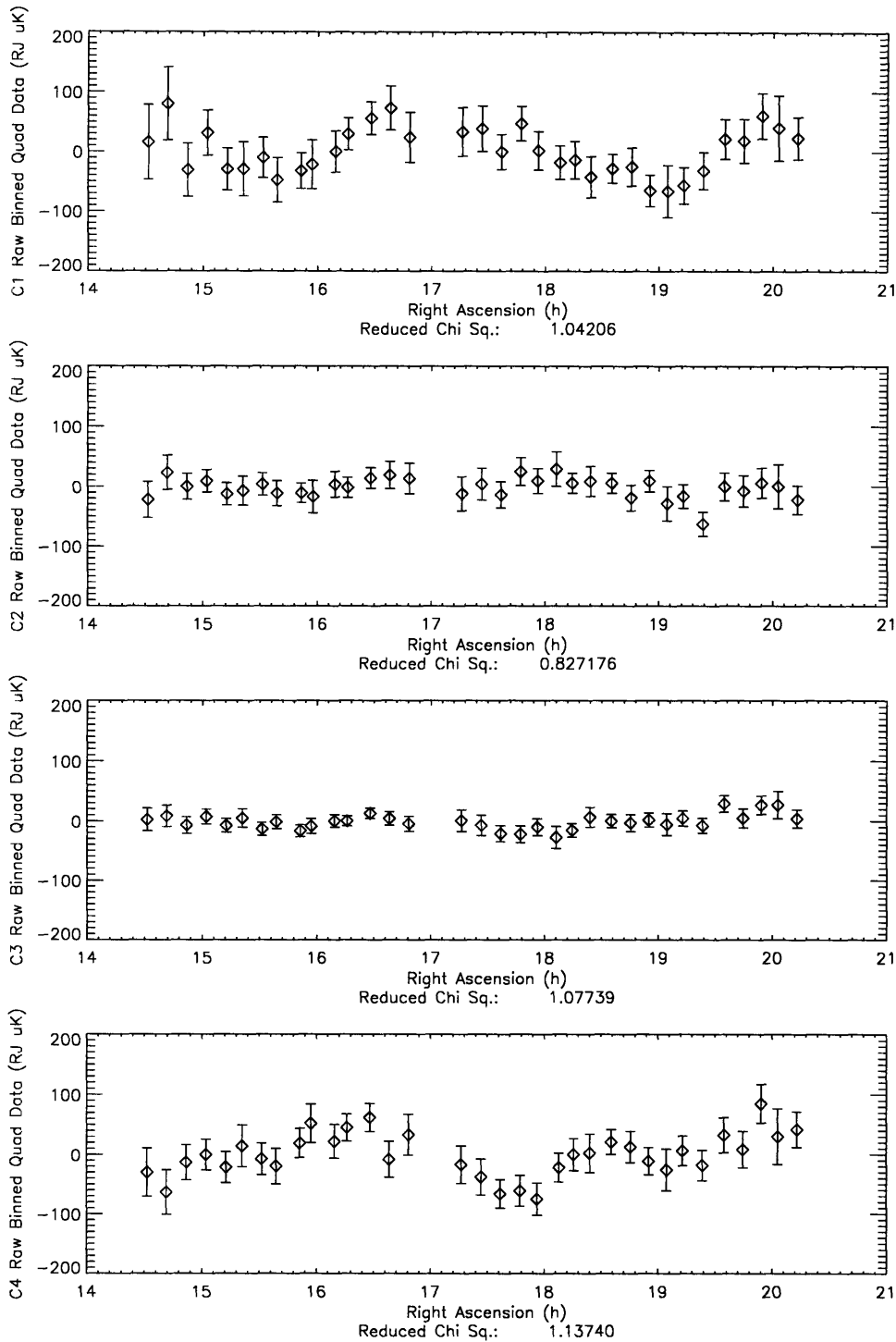


Figure 4-12: The MSAM I (1992) single difference quadrature data binned in sky coordinates but smoothed and plotted in RA . Channel 1 (5.6cm^{-1}) is plotted first followed by the other channels. The y-axis is in units of Rayleigh-Jeans temperatures.

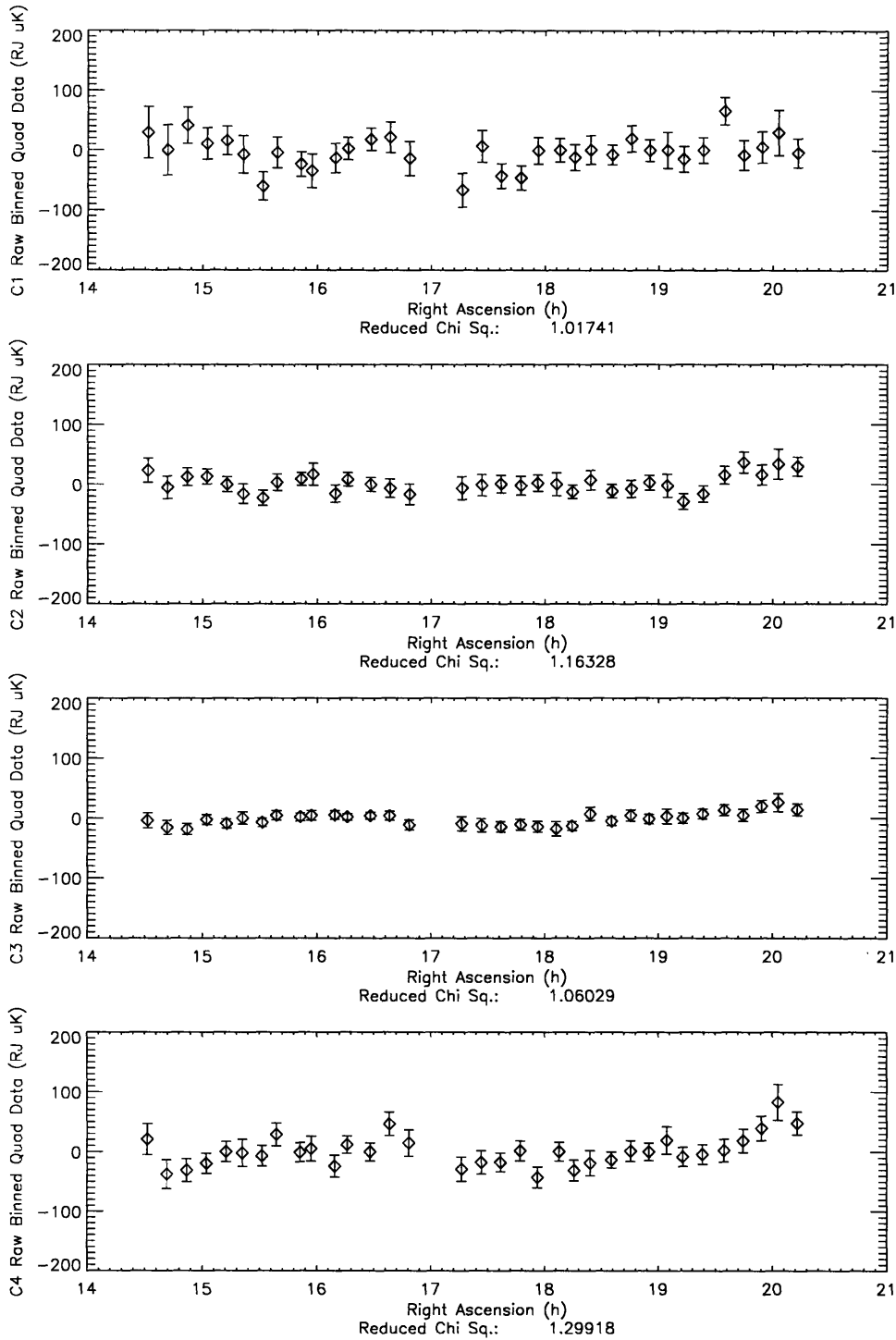


Figure 4-13: The MSAM I (1992) double difference quadrature data binned in sky coordinates but smoothed and plotted in RA . Channel 1 (5.6cm^{-1}) is plotted first followed by the other channels. The y-axis is in units of Rayleigh-Jeans temperatures.

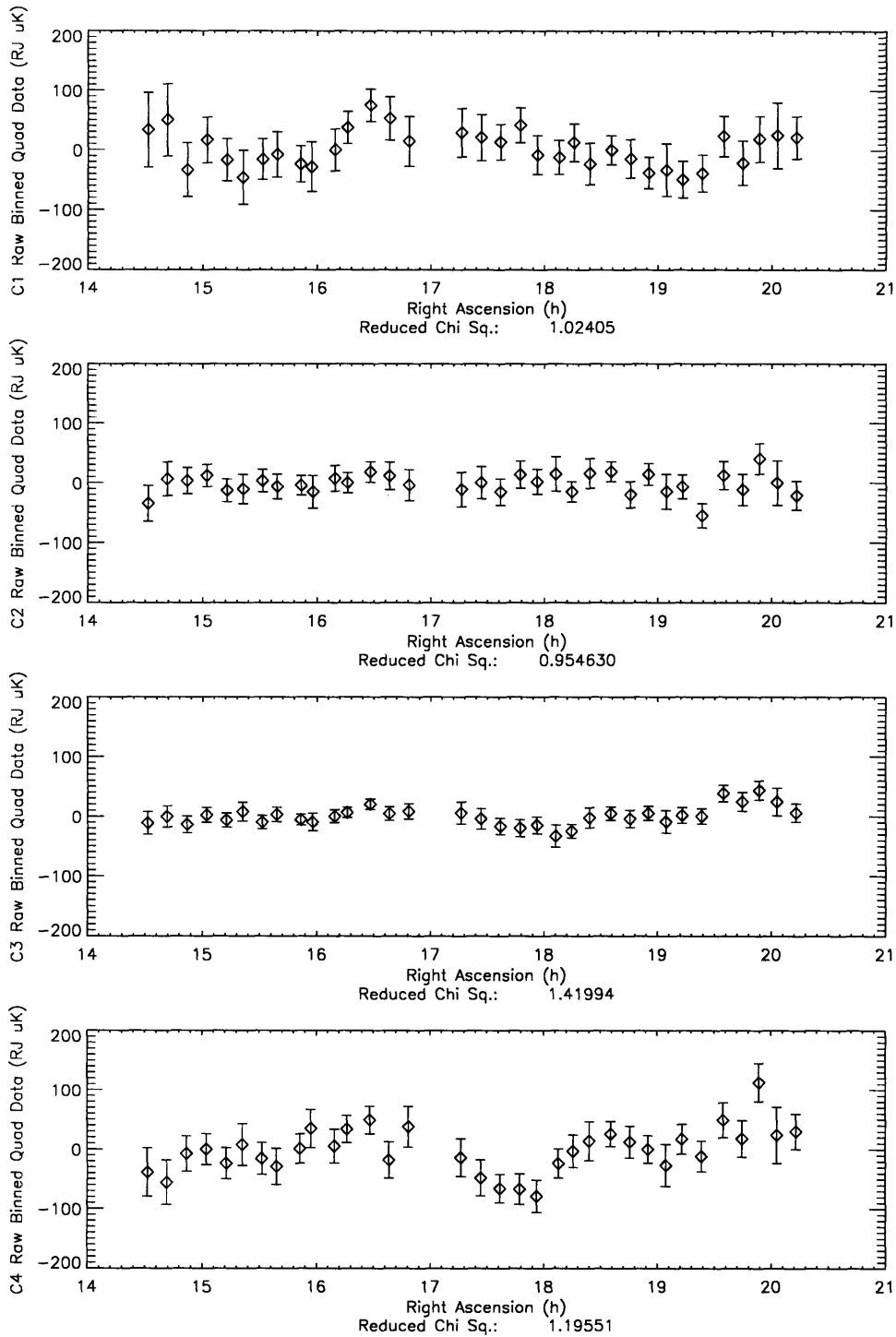


Figure 4-14: The MSAM I (1992) single difference quadrature data shifted by 15 degrees binned in sky coordinates but smoothed and plotted in RA . Channel 1 (5.6cm^{-1}) is plotted first followed by the other channels. The y-axis is in units of Rayleigh-Jeans temperatures.

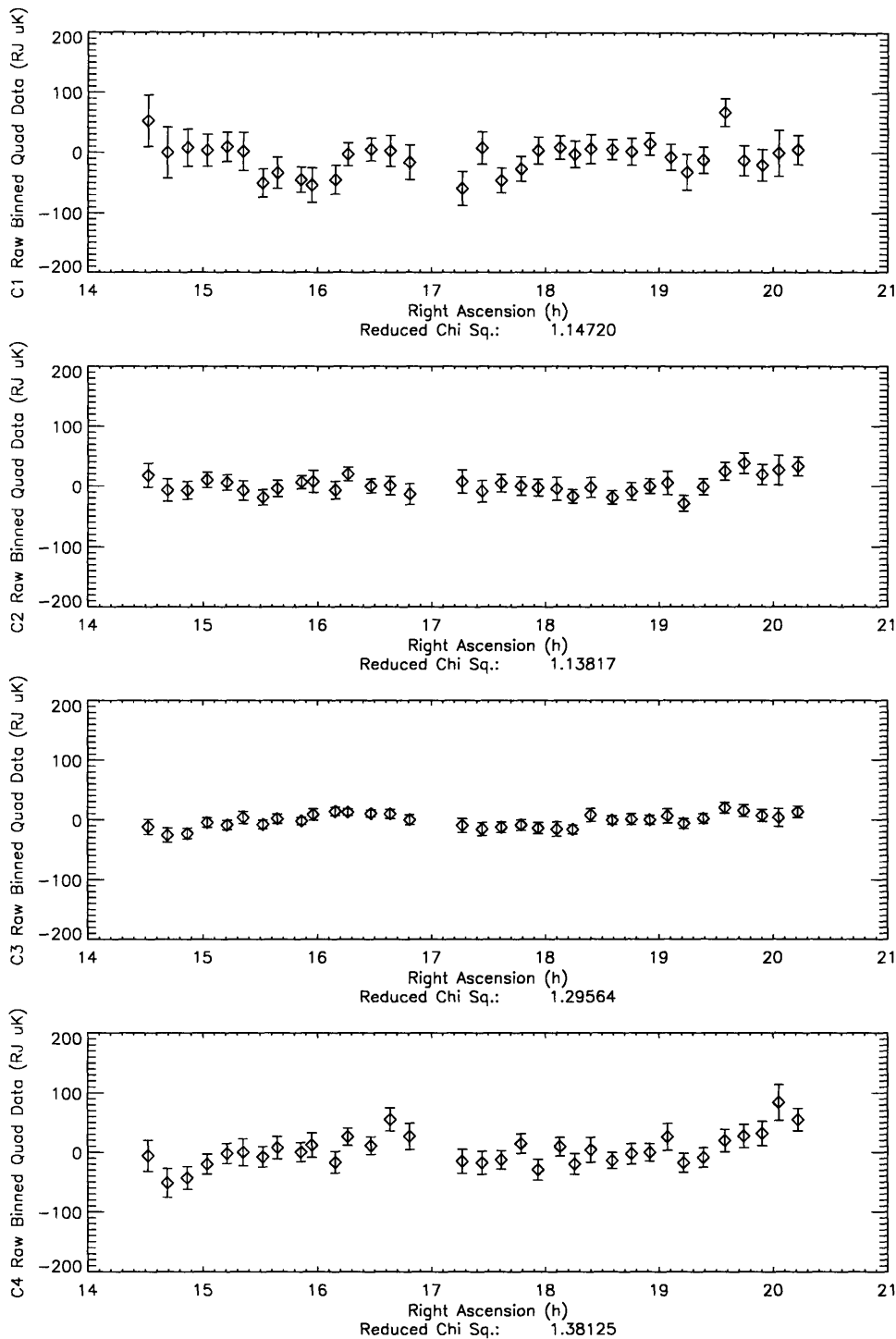


Figure 4-15: The MSAM I (1992) double difference quadrature data shifted by 15 degrees binned in sky coordinates but smoothed and plotted in RA . Channel 1 (5.6cm^{-1}) is plotted first followed by the other channels. The y-axis is in units of Rayleigh-Jeans temperatures.

and 22.5 cm^{-1} channels, while the 9 cm^{-1} channel will contain comparable signal from both. Both bremsstrahlung (free-free) and synchrotron emission will also be present in some unknown amount. Figure 4-16 shows expected contributions from warm dust, bremsstrahlung and synchrotron emission superimposed on differential Planck curves of various levels.

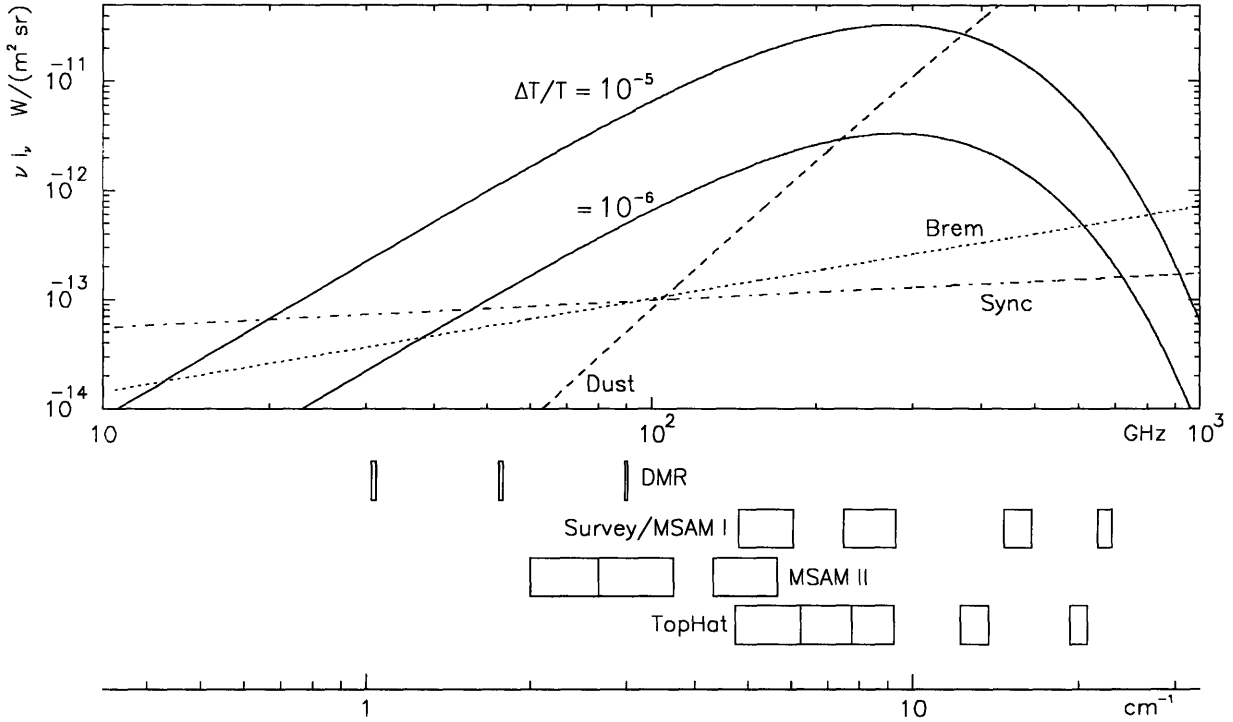


Figure 4-16: Comparison of differential Planckian spectra (solid) to that of expected foreground sources. The boxes denote the radiometer bands of COBE/DMR , FIRS and MSAM I, MSAM II (the MSAM I (1992) gondola with a different radiometer), and TopHAT (a proposed Antarctic long duration balloon experiment).

Warm Galactic dust is well characterized at $100\mu\text{m}$ from large scale survey maps such as IRAS [52], [53], [6]. The contribution at 16.5 and 22.5 cm^{-1} where MSAM I (1992) has placed two of its detectors is, however, not well understood. We compare these channels to power law scaled data produced by convolving IRAS with the MSAM antenna pattern. The assumed model for the intensity is

$$I(\nu) \sim \tau \left(\frac{\nu}{\nu_0}\right)^\alpha B(\nu, T_{\text{dust}}) \quad \text{Watts/cm}^2 \Omega \text{cm}^{-1} \quad (4.10)$$

where τ is the optical depth, B is the Planck function, ν_0 is 22.5 cm^{-1} (the central

frequency of MSAM’s most dust sensitive channel), and $\alpha = 1.5$. It is not clear that a single power law index α can be used to describe dust emission over these frequencies. Nor is it clear that we should expect the same dust index at all locations. Recent two-dust models show much better agreement to COBE maps of lower latitude regions [57], [2]. Temperatures between 4 and 7 K seem to allow for the best 2 component fits. The majority of the MSAM I (1992) MBR data are acquired in low dust regions to avoid contamination.

Full sky maps of synchrotron emission, such as the Haslam 408 MHz map, provide a base from which to extrapolate to higher frequencies. Synchrotron radiation most likely will not be of concern until frequencies below 50 GHz. Moreover, models based on surveys at 408 MHz and 1420 MHz [3] along with some understanding of electron column density in the observation region, provide plausible estimates on synchrotron emission. Estimations predict that associated anisotropies should be less than $1\mu K$ for the MSAM region. The intensity can be modeled as $I(\nu) \sim \nu^{-n}$ where n is the average spectral index, measured to be around 0.8.

Galactic bremsstrahlung emission is also modeled with a power law using an average spectral index of 0.1 ($I_{\text{brem}}(\nu) \sim \nu^{-0.1}$). However, bremsstrahlung radiation can be complicated by Galactic self absorption which leads to spatially varying spectral indices.

Unfortunately, the MSAM I (1992) spectral bands makes bremsstrahlung and MBR nearly degenerate in channels 1 and 2 (the MBR-sensitive channels). The complex nature of self absorbing clouds as well as the rather flat spectrum of bremsstrahlung create large uncertainties in extrapolation from radio measurements. The COBE/DMR maps offer some assistance. The DMR residual maps, after removal of synchrotron and galactic dust, have been spectrally decomposed to produce reasonable estimates of the bremsstrahlung sky brightness [3]. This estimate⁴ predicts that the expected MSAM I (1992) bremsstrahlung signal will be smaller than the peak MBR contribution by a factor of 10.

4.8 Spectral Modeling

To determine that part of the binned data which is spectrally consistent with a MBR Planck spectrum, the data t_{ck} for a given channel c and sky bin k are fit to the following two component model:

$$t_{ck} = \int d\nu F_c(\nu) \left[D_k \left(\frac{\nu}{\nu_0} \right)^\alpha B_\nu(T_D) + t_k \frac{dB_\nu}{dT} \Big|_{T_{\text{MBR}}} \right], \quad (4.11)$$

⁴...along with the assumption that there is about 10% contrast at the 0.5° angular scale.

where $F_c(\nu)$ is the spectral response of the instrument, $B_\nu(T)$ is the Planck function at temperature T , $T_D = 20$ K is the dust temperature, $\alpha = 1.5$ is the spectral index of the dust, $\nu_0 = 22.5 \text{ cm}^{-1}$ is the reference frequency, $T_{\text{MBR}} = 2.73$ K is the temperature of the MBR, and D_k and t_k are free parameters. This fit determines a MBR component and a Dust component. Even though one of the four degrees of freedom is taken up by the unknown offset between channels, there is still the ability to fit for an additional component. The dust and MBR components explain the vast majority of the variance so that a third component has very little discriminating ability. Neither an additional power law nor a cold dust component helps reduce the χ^2 of the spectral fit. The χ^2 for the fit is 237/292 for the single difference data and 454/294 for the double difference data.

4.8.1 Dust Component

Varying T_D and α by reasonable amounts does not significantly affect the MBR component. Hence, the dust temperature T_D is fixed at 20K and the power law index α at 1.5. Figure 4-17 displays the dust component for both demodulation types. Like the MBR data figures, these plots use a binning which is about four times more coarse than the binning used for the analysis.

The region in which MSAM I (1992) observes is not free of warm ($T \sim 20$ K) dust. Channels 3 and 4 are increasingly sensitive to dust. The overplotted line in Figure 4-17 represents the IRAS 100 μm measurements [52], [53] convolved with the MSAM I (1992) antenna pattern then scaled via a simple power law. The scaling index α is determined by a least squares best fit between the mean subtracted IRAS and MSAM I (1992) channel 3 data. The free parameter is $g = (\nu_3/\nu_{\text{IRAS}})^\alpha$. Each demodulation scheme is processed separately. The χ^2 for the fits are 303/145 for the double difference data and 224/144 for the single difference data. The uncertainty in the fit parameters g_{sd} and g_{dd} is rather high at $\frac{\delta g_{dd}}{g_{dd}} = 1.4$ and $\frac{\delta g_{sd}}{g_{sd}} = 1.3$. There is an unexplained factor of 2 difference between g_{sd} and g_{dd} . Since the spectral decomposition folds in the antenna pattern, the factor of 2 difference in normalization is not the cause of the difference. It may not be valid to assume that one spectral index can describe the 70 cm^{-1} span from IRAS to MSAM I (1992) or that α is uniform over all angular scales and locations.

The implied dust spectral index α is not the same for both demodulation types since the fit parameters are different. For the single difference demodulation $\alpha = 1.3$ and for the double difference $\alpha = 1.65$. We chose an index of $\alpha = 1.5$ for the spectral decomposition which agrees reasonably well with these results.

There is a significant spatial correlation between the IRAS data and the fit dust component. Long term drift in the MSAM I (1992) data may be effecting the first half of the double difference data since its morphology resembles IRAS except for a slope.

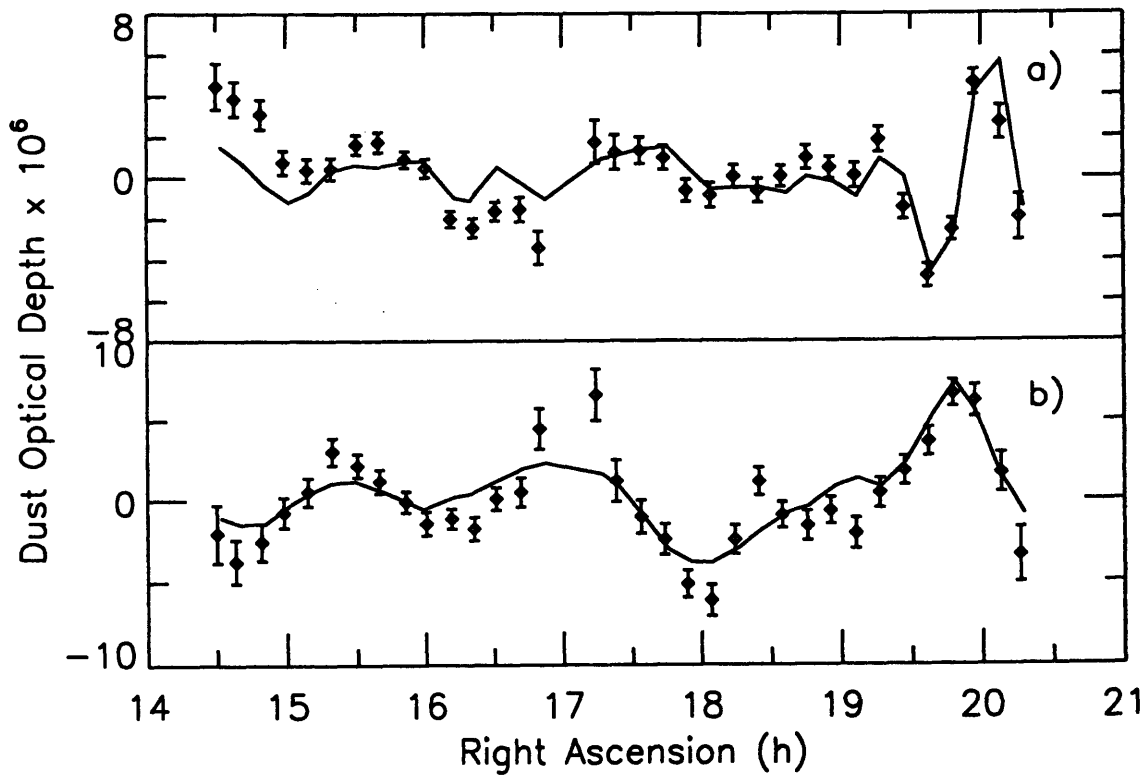


Figure 4-17: The dust component in terms of optical depth D_k referred to 22.5 cm^{-1} . Data has been smoothed for this plot. The IRAS 100 micron data convolved with our beam pattern is superimposed. (a) Double Difference (b) Single Difference.

4.8.2 MBR Component

A substantial fraction of the variance in the raw data set can be attributed to signal which is spectrally consistent with a 2.73 K blackbody as would be expected for detection of the MBR. Figure 4-18 demonstrates several statistically significant features. Most notable is a prominence (hereafter MSAM15+82) at an RA of $14^{\text{h}}.92 \pm 0^{\text{h}}.03$. This is a rather dust-free region, unlike the region observed at the end of the flight. The feature is seen in both demodulation schemes with similar magnitudes. The measured flux density is 4.5 ± 0.7 Jy at 5.6 cm^{-1} , including calibration uncertainty. The morphology resembles the MSAM I (1992) point spread function (PSF). The constraint on the signal region is less than 20 arcminutes.

An additional feature (MSAM19+82) at an RA of $19^{\text{h}}.29 \pm 0^{\text{h}}.03$ is also detected. Here, the single difference data also displays the PSF shape though there is confusion due to a nearby dusty region. The measured flux density is 3.6 ± 0.6 Jy at 5.6 cm^{-1} .

The declination of these regions is not well constrained since we do not scan in elevation. Bounds are placed by the beam width and pointing information at $82.00^\circ \pm 0.25^\circ$. Discussion of our attempts to understand the nature of these source-like features will be covered in the next chapter. There is other structure in this data set. Even if these regions are rejected as unknown foreground sources, statistically significant signal remains. Cheng et al. (1994) also reports the results of analyzing the *source-free* data.

4.9 MBR Fluctuation Limits

Limits are placed on anisotropy [13] in the observed MBR component by assuming that a Gaussian random field model describes the sky temperature deviations $\Delta T(\mathbf{x})$. Under this assumption the sky can be completely described by the two point correlation function

$$C(|\mathbf{x}_1 - \mathbf{x}_2|) = \langle \Delta T(\mathbf{x}_1) \Delta T(\mathbf{x}_2) \rangle. \quad (4.12)$$

The k th measurement of the sky, t_k is comprised of the sum of the actual sky signal s_k and the noise contribution from the instrument n_k . For each observation, the antenna pattern has a particular orientation on the sky denoted as $H_k(\mathbf{x})$. Since the pattern is independent of time, each $H_k(\mathbf{x})$ is equivalent up to a translation and a rotation. If we consider the sky signal in the appropriate coordinate system for the k th observation, we can write

$$s_k = \int d\mathbf{x} H_k(\mathbf{x}) \Delta T(\mathbf{x}) \quad (4.13)$$

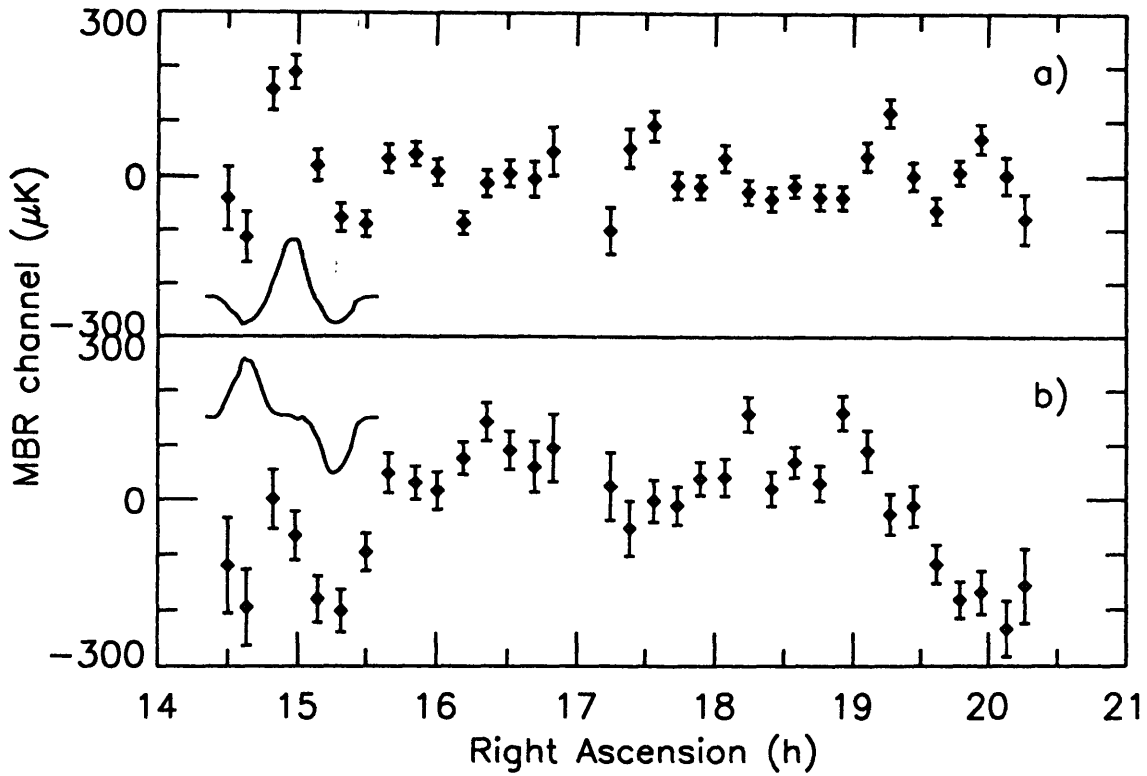


Figure 4-18: The MBR spectral component t_k smoothed and plotted in RA: (a) Double Difference (b) Single Difference. The beam pattern is also overlotted for scale.

making the sky covariance

$$\langle s_k s_l \rangle = \int dx_1 dx_2 H_k(x_1) H_l(x_2) C(|x_1 - x_2|). \quad (4.14)$$

The noise covariance can be approximated by $\langle n_k n_l \rangle = \delta_{kl} \sigma_k^2$. The current analysis of the MSAM I 1994 data includes the correlation effects due to dedrifting and shows that the effect on the binned data is minimal.

Since the sky signal and instrument noise are uncorrelated we may write $\langle t_k t_l \rangle = \langle s_k s_l \rangle + \delta_{kl} \sigma_k^2 \equiv (W_{kl})^{-1}$.

There are two favored methods of finding bounds on the amount of variance in the data: the Bayesian approach [4] and the Maximal Likelihood Ratio test [31],[1]. We have chosen to use the MLR test. Suppose we had N flights with p observations in each. If the observations are drawn from a normal distribution, the likelihood function is

$$L = \frac{1}{(2\pi)^{\frac{pN}{2}} |\mathbf{W}^{-1}|^{\frac{N}{2}}} \exp \left[\frac{-1}{2} \sum_{\alpha=1}^N \mathbf{t}_\alpha \mathbf{W} \mathbf{t}_\alpha \right]. \quad (4.15)$$

In this case $N = 1$ and p is the number of observations. Denoting the null sky signal hypothesis with $(W_{kl}^0)^{-1} = \delta_{kl} \sigma_k^2$, we form the likelihood ratio statistic λ where

$$\lambda = \left(\frac{\det \mathbf{W}}{\det \mathbf{W}^0} \right)^{1/2} \exp \left(-\frac{1}{2} \mathbf{t} (\mathbf{W} - \mathbf{W}^0) \mathbf{t}^T \right). \quad (4.16)$$

We assume the primordial fluctuations are also Gaussian and generate a probability density function $\rho_C(\lambda)$ for λ . Call λ^* the likelihood ratio for our particular observation. For some minimal amplitude, 95% of the evaluations of λ with data drawn from the model distribution will be greater than the observed measurement of λ^* . This is called the 95% confidence lower bound. Alternatively, for some maximal amplitude, 95% of the λ evaluations will be lower than λ^* (the 95% confidence upper bound). The limits demark a 90% confidence interval. The 95% confidence limits to the amplitude of fluctuations are placed by integrating the probability density function:

$$\int_0^{\lambda^*} d\lambda \rho_C(\lambda) = 0.95 \quad \text{Upper Bound} \quad (4.17)$$

$$\int_0^{\lambda^*} d\lambda \rho_C(\lambda) = 0.05 \quad \text{Lower Bound} \quad (4.18)$$

The evaluations are determined by Monte-Carlo integration [40]. Table 4.4 lists the upper and lower bounds on MBR component anisotropy for the entire flight.

Table 4.4: Upper and lower bounds on MBR component anisotropy. Bounds are also placed on the isolated source-like regions.

	θ_c	RA (h)	Upper (μK)	Lower (μK)	Comment
Single	0.5°	14.44–15.69	221	39	MSAM15+82 region
Diff.		14.44–20.33	116	53	Full flight
		15.69–18.55	61	16	Source-free region
Double	0.3°	14.44–15.69	336	91	MSAM15+82 region
Diff.		14.44–20.33	97	50	Full flight
		15.69–18.55	85	30	Source-free region

Figure 4-19 shows the upper and lower bounds to the total rms anisotropy ($C_0^{\frac{1}{2}}$) as a function of correlation angle for a Gaussian correlation model. For this model,

$$l(l+1)C_l = 2\pi C_0 l^2 \theta_c^2 e^{-1/2l^2\theta_c^2} \quad (4.19)$$

where the power through our observation window W_l is

$$Power = (\Delta T/T)^2 = \frac{1}{4\pi} \sum_{l=2}^{\text{inf}} (2l+1)C_l W_l \quad (4.20)$$

These bounds on $C_0^{\frac{1}{2}}$ can be approximately converted to the flat spectrum power referred to the quadrupole Q_{flat} by noting that $Q_{flat} \sim 0.46C_0^{\frac{1}{2}}$ for the single difference demodulation and $Q_{flat} \sim 0.50C_0^{\frac{1}{2}}$ for the double difference demodulation [55].

The double difference is most sensitive at $\theta_c = 0.3^\circ$ and the single difference at $\theta_c = 0.5^\circ$. At these angles, the 90% single difference confidence interval is $1.8 \times 10^{-5} < \Delta T/T < 4.2 \times 10^{-5}$. For the double difference data, the result at the most sensitive angle is $1.8 \times 10^{-5} < \Delta T/T < 3.5 \times 10^{-5}$.

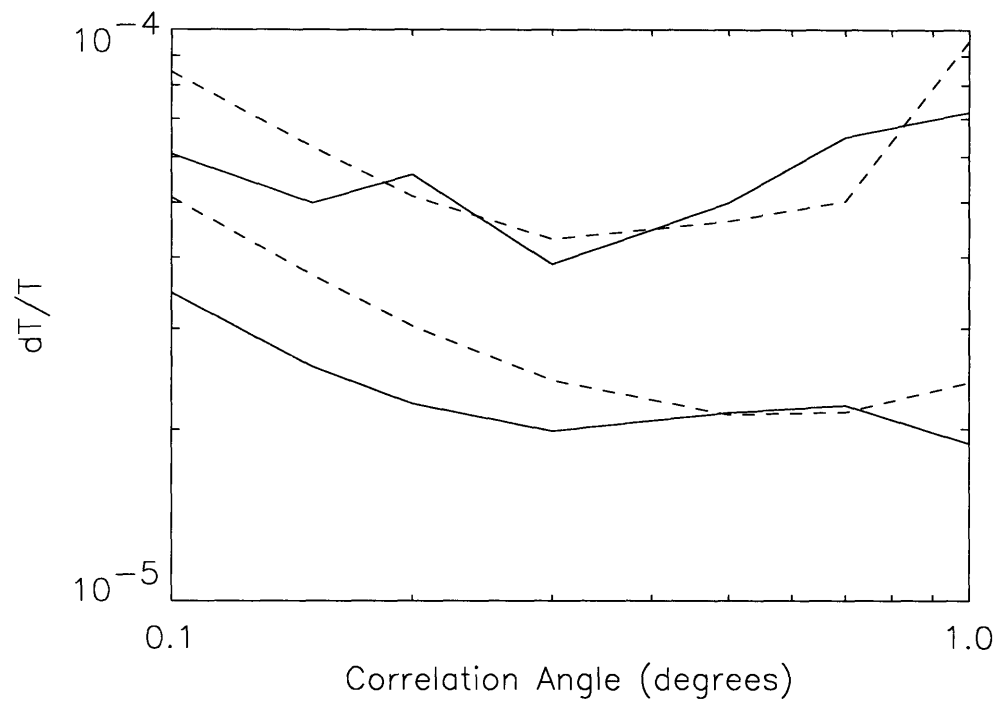


Figure 4-19: Upper and lower bounds for a Gaussian auto correlation function (GACF) model as a function of the correlation angle θ_c for the entire flight. Shown are the 95% confidence upper and lower limits for double difference (solid) and single difference (dashed).

4.10 Summary

MSAM I has detected variations in the MBR which are spectrally consistent with a 2.735 K Planck function as would be expected for anisotropy in the MBR. The four channel spectral lever arm of the radiometer allows for reliable removal of dust emission which would normally confuse the MBR signature. Galactic synchrotron emission is also considered an unlikely source based on radio survey extrapolations. We can not, in general, rule out bremsstrahlung radiation as a contributing source in the MBR component signal, though extrapolation from COBE/DMR measurements would imply it has a negligible effect in our passbands. There is insufficient sky sensitivity to rule out cold dust in general.

The unresolved features resembling the MSAM I (1992) point spread function have been investigated further. Due to their brightness and the additional observations of the MSAM15+82 region by other experiments, stronger constraints have been placed on their spatial extent and spectral characteristics.

Chapter 5

Discussion of Results

5.1 MBR Source-like Features

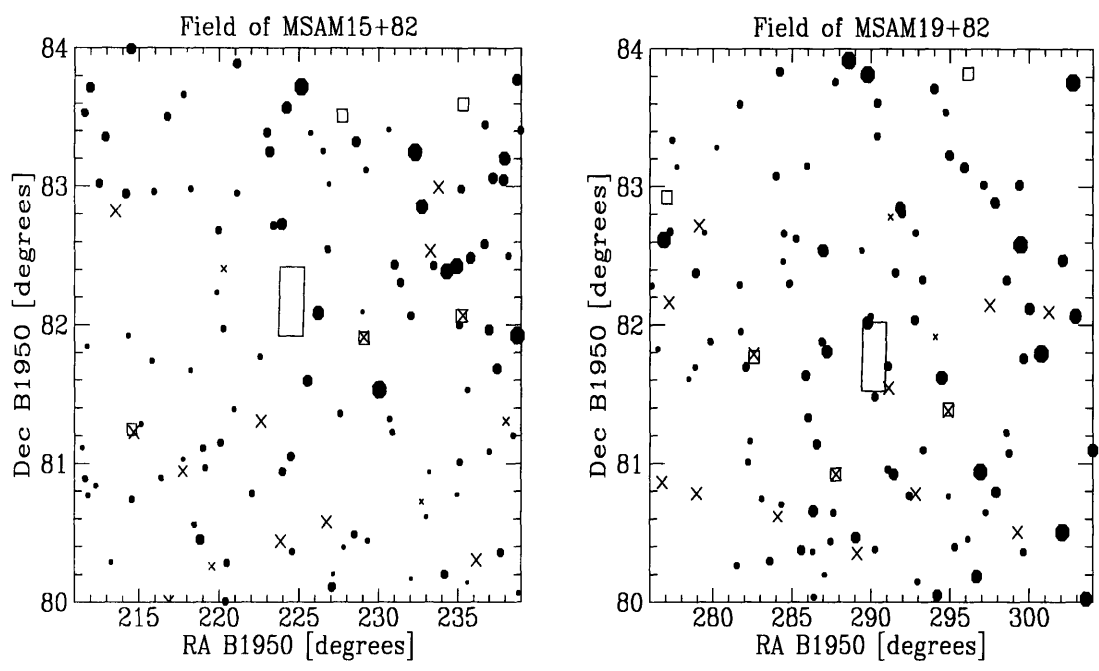
The most striking regions of the MSAM data set are the two source-like features MSAM15+82 and MSAM19+82. The details of the analysis of these regions will be published in a paper in preparation [29]. A search through several source catalogs reveals no likely foreground candidates at either location. In addition to those catalogs listed in Figure 5-1, there are also no plausibly correlated objects found in the Abell Cluster Catalog or the Brightest Galaxy Catalog.

Since sky surveys at a few hundred GHz are difficult due to atmospheric emission, there are no full sky maps on half degree angular scales for comparison. We cannot rule out the possibility that these regions are the signature of a previously unsuspected class of foreground object.

Because of the brightness of MSAM15+82 and MSAM19+82, it is possible to analyze their spectral characteristics, constrained by both demodulation schemes and by frequency. The channel 4 binned data is used to remove an estimate of the dust signal from the binned data of the other three channels. A power law scaling index of 1.5 is assumed. Channels 1 through 3 are searched for spatially unresolved sources as follows.

The amplitude of a source in bin i is estimated by fitting the sky binned data to a constant times the telescope point spread function centered on bin i . The amplitude which maximally decreases the χ^2 of the whole data set is then determined for each sky bin. This fit is done for each bin i to place limits on the position and amplitude of the unresolved features.

To create a sensible χ^2 , it is necessary to fit the point PSF only to the local region about a source-like feature. Using the locations found from the χ^2 -decrement technique, Table 5.1 lists the χ^2 for the 1.5° region centered on each of the two



- 4.9 GHz Kuehr et. al., Polar Cap Survey
- × 1.4 GHz Becker and White, Northern Sky Survey
- 100 micron IRAS Faint Source Catalog

Jul 5 15:00:39 1993

Figure 5-1: The sky fields associated with MSAM15+82 and MSAM19+82 in regressed to 1950 coordinates. The size of the symbol is proportional to its flux.

features. Channel 3 shows no appreciable detection.

Table 5.1: χ^2 for the isolated source-like regions MSAM15+82 and MSAM19+82 before and after removal of a best fit PSF.

MSAM15+82		
Channel	Before	After
1	124 / 35 dof	78.3 / 34 dof
2	95.4 / 33 dof	68.1 / 32 dof

MSAM19+82		
Channel	Before	After
1	110 / 49 dof	41.3 / 48 dof
2	135 / 51 dof	118 / 50 dof

Figures 5.1 and 5.1 show the flux density in the first three channels as well as the best fit spectral predictions for CMBR, bremsstrahlung, synchrotron and cold dust. Since there is no detection in channel 3, the statistical uncertainty of the fit is substantial. This frequency cutoff allows discrimination between several possible physical models. The case is stronger for MSAM15+82. The reduced χ^2 for the various models seem to indicate that CMBR consistent signal is the most likely candidate. The data on MSAM19+82 do not rule out synchrotron emission.

Numerical simulations [28],[24] indicate that isolated 0.5° features of substantial amplitude are not uncommon in standard CDM. While these COBE-normalized simulations seem to favor slightly smaller amplitude structures, the predicted mean number per beam solid angle of features with the amplitude measured by MSAM I (1992) is in agreement.

5.2 Additional Observations and Recent Results

Observations with the BIMA Hatcreek Interferometer have placed strong constraints on the MSAM15+82 region [10]. BIMA operates at 90 GHz with a FWHM beam size of 2.33 arcminutes. The instrument response is cusped to favor the detection of point sources. Calibration is claimed to be internally accurate to 20% using 3C345 as the calibration source. Chernin and Scott report noise limited upper limits of 16mJy at 90 GHz. The BIMA measurement does not rule out a substantial brightness at 90 GHz if MSAM15+82 is an extended source larger than about 5 arcminutes.

The SUZIE bolometer array at CSO operates at 4.7 cm^{-1} ($\sim 140 \text{ GHz}$) with a 1.7 arcminute beam and has also observed the MSAM15+82 region [11]. The SUZIE

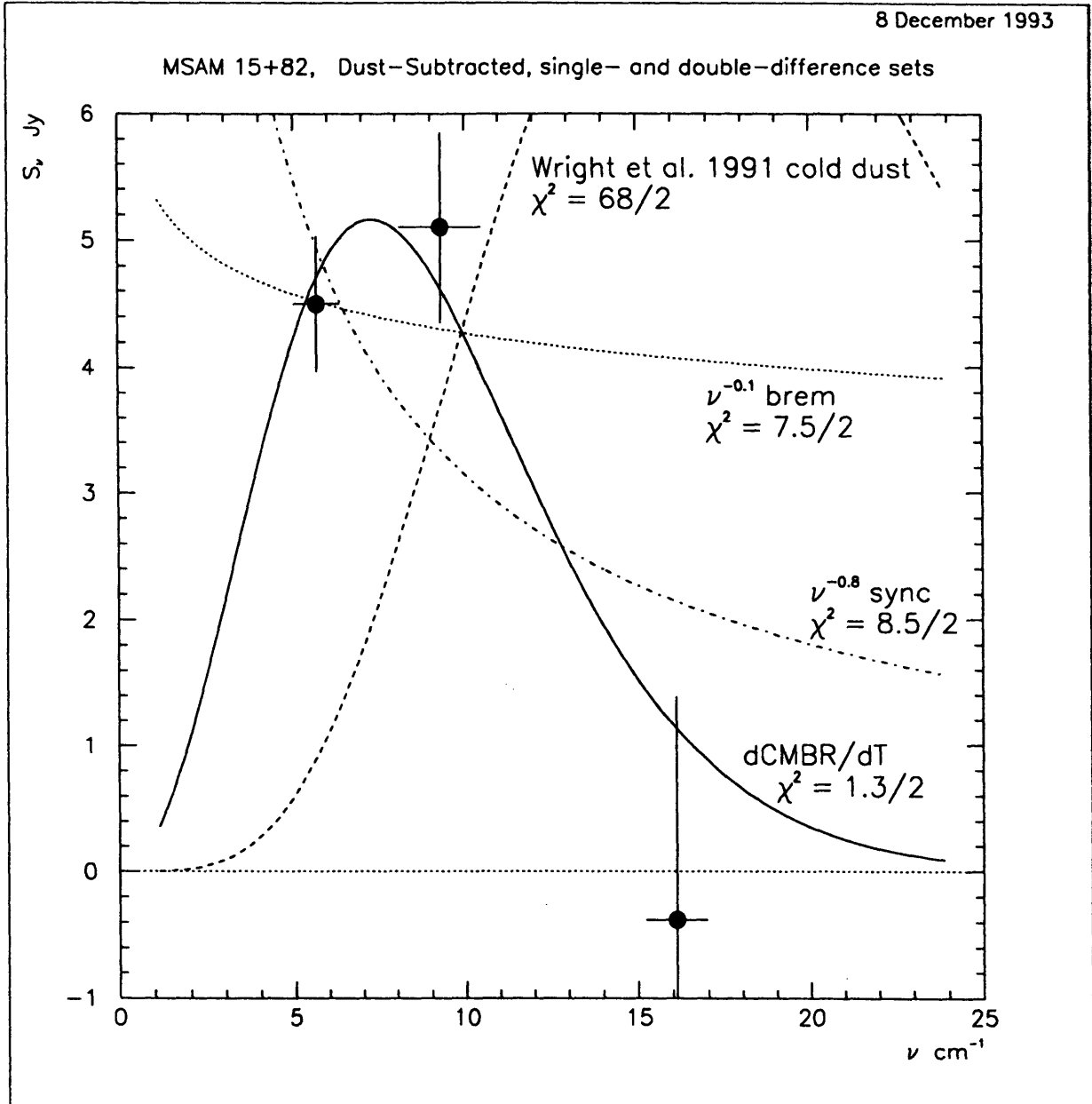


Figure 5-2: The measure flux density for MSAM15+82 at 5.6, 9.0, and 16.5 cm^{-1} . Overplotted are four best fit models.

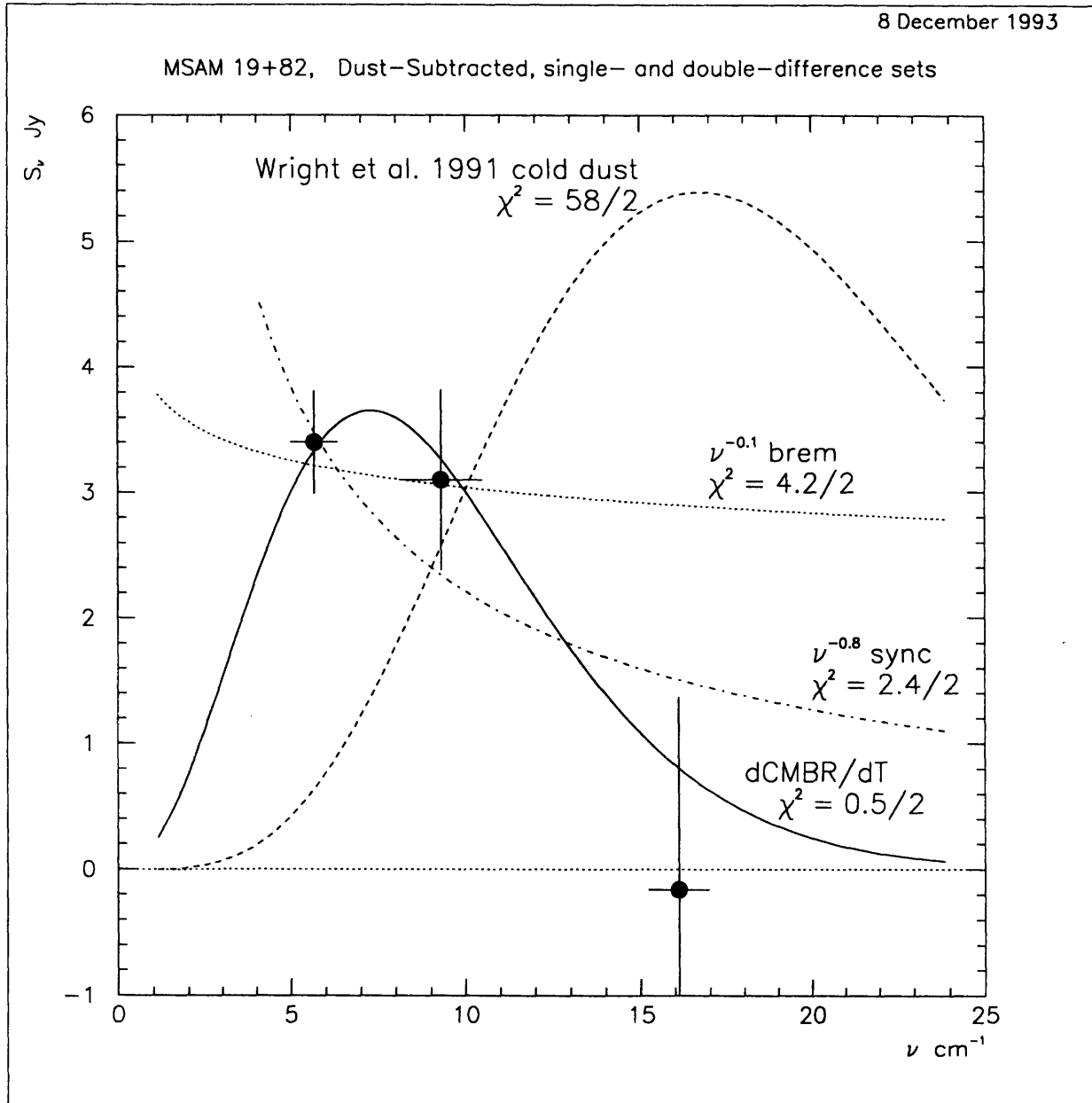


Figure 5-3: The measure flux density for MSAM19+82 at 5.6, 9.0, and 16.5 cm^{-1} . Overplotted are four best fit models.

sensitivity is $\leq 200 \text{ mJy}/\sqrt{\text{Hz}}$ at 4.7 cm^{-1} . The rms noise of a single scan is 0.5 Jy. A 3 Jy source as observed by MSAM would have been detected if its angular extent were less than a few arcminutes. Because the bandpass is so close to the MSAM radiometer, the null result reported for objects less than 2 arcminutes in angular extent implies that the MSAM15+82 region is most likely an extended feature. Several arcsecond sized, sub-Jy sources are also not ruled out, although the BIMA measurement makes this unlikely. If we assume a flat spectrum between 4.7 and 5.6 cm^{-1} then the SUZIE data place a 3σ lower limit of 2.8 arcminutes on MSAM15+82.

MSAM I was successfully flown again in the spring of 1994 from Palestine, Texas. Significant pointing overlap was achieved. Details of these results as well as the cross-correlation between the two flights will be published shortly. Preliminary results indicate that MSAM15+82 has been detected again. Since major modifications to the upper structure of the gondola were made before this last flight, sidelobe contamination is considered unlikely as a possible creation mechanism.

5.3 Summary and Future Plans

The MSAM I (1992) experiment detected statistically significant fluctuations in the MBR at the 0.5° angular scale. Using a GACF analysis, the double difference is most sensitive at $\theta_c = 0.3^\circ$ and the single difference at $\theta_c = 0.5^\circ$. At these angles, the 90% single difference confidence interval is $1.8 \times 10^{-5} < \Delta T/T < 4.2 \times 10^{-5}$. For the double difference data, the result at the most sensitive angle is $1.8 \times 10^{-5} < \Delta T/T < 3.5 \times 10^{-5}$. Much of the signal is due to two prominent regions of the sky binned data which are spectrally consistent with small but extended ($3' < \theta_{\text{diam}} < 20'$) MBR sources. They are not correlated with known foreground sources.

An additional successful of MSAM I in June of 1994 is currently being analyzed. Significant pointing overlap with the 1992 flight was attained. A publication detailing the results of this flight as well as the cross-correlation with the 1992 data is in preparation. One more flight of MSAM I is planned for June of 1995 during which the MSAM15+82 region will be observed again.

Appendix A

Conversion of MSAM's Demodulated Signal to a Rayleigh-Jeans Temperature Difference

A.1 Preliminaries

The following is an attempt to clarify part of the demodulation procedure and to understand how to convert MSAM's measured demodulated signal in counts to an equivalent temperature in Kelvin. The process of this conversion uses what could be called an *effective* beam size. In so far as we wish to talk about Rayleigh-Jeans sky temperature of the demodulated signal, it is necessary to define what is meant by the effective beam size.

The single difference demodulated output of MSAM is a measure of the difference in flux from two regions of sky separated by approximately 1.4 degrees. It is a measure of the gradient in the sky on that angular scale. The double difference demodulation subtracts the average flux of two regions 0.7 degrees on either side of a central region from the flux of that central region. The double difference is then a measure of curvature and is insensitive to gradients.

As a baseline for symbols and units, define the power P in ergs/sec detected by a telescope of effective area A and spatial antenna response B as:

$$P = A \int I_\nu F_\nu B_\nu d\nu d\Omega \quad (\text{A.1})$$

where I_ν is the spectral radiance in $\text{erg/s/cm}^2/\text{Hz/str}$ and F_ν is the frequency filter function. Note that B is dimensionless and represents the antenna pattern with the secondary mirror in a fixed position.

In applying this to MSAM, we note that power P is proportional to volts across a specific detector which is proportional to the number of counts stored in the archive. Equation (A.1) can be made to reflect this by considering B to have the units of $\text{counts}/\frac{\text{ergs}}{\text{s}}$. Then P represents what is stored in the archive when the telescope is fixed observing a position in the sky. F_ν is still a dimensionless transmission function since its value is not derived from archive values like the beam profile B .

We would like to find an expression relating the Rayleigh-Jeans single or double difference temperature and the demodulated signal produced by our analysis. Since the two types of demodulation yield similar results, only the single difference will be handled in detail.

A.2 Ideal Demodulation

A.2.1 Assumptions

Consider first the ideal single difference demodulation. The following will be assumed at some point in the next subsection:

- The calibration source, Jupiter, is much hotter than the sky and, hence, the difference in temperature between adjacent regions of the sky is also much smaller than the temperature of Jupiter.
- The angular size of Jupiter is small compared to the angular size of the telescope antenna response.
- The telescope antenna pattern is circularly symmetric about its centroid and is independent of chopper position. Unless otherwise noted, "beam" refers to the static chopper telescope response (as opposed to the chopped beam response).
- All equations, when Jupiter is a contributing factor, assume that the center of Jupiter is at the centroid of the telescope beam.
- The temperature of the sky is constant over the entire antenna pattern and hence there is no overlap in the beams when displaced by the chopper. This is definitely not true. The beam overlap is ~ 10 percent.
- The antenna pattern is not a function of frequency over the bandpass for a specific channel. This is approximately true for MSAM.

A.2.2 Demodulated Signal

The single difference demodulated signal for a given channel can be expressed as

$$\Delta_2 P = A \int d\nu F_\nu \int d\Omega [I(\nu, T_l) B_l(\theta, \phi) - I(\nu, T_r) B_r(\theta, \phi)] \quad (\text{A.2})$$

where B_l and B_r denote the beams when the telescope is looking to the left or right of the center. The sky temperatures at these locations are T_l and T_r .

For the double difference case

$$\Delta_3 P = \frac{A}{2} \int d\nu F_\nu \int d\Omega [2I(\nu, T_c) B_c(\theta, \phi) - (I(\nu, T_l) B_l(\theta, \phi) + I(\nu, T_r) B_r(\theta, \phi))] \quad (\text{A.3})$$

where the factor of $\frac{1}{2}$ provides that a signal of 1 Jupiter in the center beam gives the same magnitude double difference power value as a signal of 1 Jupiter in one of the side beams for the signal difference demodulation.

Using the assumption that the telescope beam is circularly symmetric and is independent of chopper position, we can then write

$$\Delta_2 P = A \int d\nu F_\nu \int d\Omega [\partial_T I(\nu, T) \Delta_2 T B(\theta, \phi)] \quad (\text{A.4})$$

where $\Delta_2 T = (T_l - T_r)$

Consider now when Jupiter is in one of the beams, say the left one. Define $H(\theta, \phi)$ as the unit step function which delimits Jupiter. Then

$$\Delta_2 P_j = A \int d\nu F_\nu \int d\Omega [I(\nu, T_l) B_l(\theta, \phi)(1 - H(\theta, \phi)) + I(\nu, T_j) B_l(\theta, \phi) H(\theta, \phi) - I(\nu, T_r) B_r(\theta, \phi)] \quad (\text{A.5})$$

Again, by evoking the similarity of the left and right beam and remembering that the angular size of Jupiter is small compared to the beam, we see that the differenced sky contribution is small compared to the signal from Jupiter. Note that the beam filling factor for Jupiter is close to 1600 which makes its contribution to the power less than that of the 2.735 K sky by a factor of 10. However, ΔT_{sky} is less than 0.001 K so, evoking beam similarity, the following should hold to a few percent:

$$\Delta_2 P_j = A \int d\nu F_\nu \int d\Omega I(\nu, T_j) B(\theta, \phi) H'(\theta, \phi) \quad (\text{A.6})$$

where $H'(\theta, \phi)$ is the unit step function in the beam centroid coordinates.

Now make a Rayleigh-Jeans approximation (worry about converting to CMBR

temperatures later). For the sky observation:

$$\Delta_2 P = \frac{2k}{c^2} A \Delta_2 T^{rj} \int d\nu \nu^2 F_\nu \int d\Omega B(\theta, \phi) \quad (\text{A.7})$$

For observations of Jupiter:

$$\begin{aligned} \Delta_2 P_j &= \frac{2k}{c^2} A T_j \int d\nu \nu^2 F_\nu \int d\Omega B(\theta, \phi) H'(\theta, \phi) \\ &\sim \frac{2k}{c^2} A T_j \Omega_j B(0, 0) \int d\nu \nu^2 F_\nu \end{aligned} \quad (\text{A.8})$$

I have assumed the the beam profile B does not change over the spatial extent of Jupiter. To remove the dependence on common constants, take the ratio :

$$\frac{\Delta_2 P_j}{\Delta_2 P} = \frac{T_j}{\Delta_2 T^{rj}} \frac{\Omega_j B(0, 0)}{\int B(\theta, \phi) d\Omega} \quad (\text{A.9})$$

The analogous double difference equation is found by placing Jupiter in the center beam and using the definition $\Delta_3 T^{rj} = (2T_c - T_l - T_r)$. Note that the value of the beam profile at the center is present as a multiplicative factor.

A.3 Software Demodulation

The above needs to be compared to what is done in software. For each chopper position, there are 4 samplings of the detector signal. I will assume that the electronic transfer function has been removed from the data. This is part of the analysis of the 1992 MSAM data. The removal of this transfer function is valid only to 8 Hz. However, the primary signal is at 2 or 4 Hz implying that this level of accuracy is sufficient.

Each of the 4 detector samples (units of counts) is proportional to the power incident upon the dectector from the sky plus foreground power. In general, this foreground power is non-negligable. One way to isolate the sky signal (to some level) is to construct a lockin which is phase synchronous with the chopper position signal. This locked-in signal will be the measured demodulated value which is proportional to the ideal demodulated power.

If the experiment had symmetric, non-overlapping beams, a measured demodulated signal could be calculated by:

$$\Delta_2 P^{meas} = \sum_{i=1}^4 C_i^i B_i^i(0, 0) - \sum_{i=1}^4 C_r^i B_r^i(0, 0) = D_2 \quad (\text{A.10})$$

$$\Delta_3 P^{meas} = 2 \sum_{i=1}^4 C_c^i B_c^i(0,0) - \sum_{i=1}^4 C_l^i B_l^i(0,0) - \sum_{i=1}^4 C_r^i B_r^i(0,0) = D_3 \quad (\text{A.11})$$

where C^i is the counts at one of the 4 samplings of the chopper position. B' denotes the dimensionless vector of length 4 representing the response (minus any offset) at each point in one of the three chopper positions when Jupiter is located at the center of that beam. All four values of B' would be the same if the complete electronic transfer function had been removed and the chopper executed a perfect square wave chop.

Provided the beam is reasonably symmetric and we neglect information beyond 8 Hz, the above is approximated by making a lockin at 4 Hz for the double demodulation case and a linear combination of 2 and 6 Hz for the single demodulation case. The actual demodulation deals with all 16 points in a chopper cycle at one time such that $D_3 = \sum_{i=1}^{16} B_3^i C^i$ and $D_2 = \sum_{i=1}^{16} B_2^i C^i$ where B_2 and B_3 are vectors constructed from a lengthwise cut through the chopped beam profiles. The lockin is constructed by removing all but the desired frequencies from B_2 and B_3 as was described in a previous note.

Eventhough this is not the total modulated power we can assume that it is proportional to it. Then

$$\frac{\Delta_2 P_j}{\Delta_2 P} = \frac{D_2^j}{D^2} \quad (\text{A.12})$$

$$\frac{\Delta_3 P_j}{\Delta_3 P} = \frac{D_3^j}{D^3} \quad (\text{A.13})$$

To link the ideal case to the software analysis, we need one other bit of information. When Jupiter is in the center of either the left or right beam (let's say the left), we measure

$$\begin{aligned} B(0,0) &= \sum_{i=1}^4 C_l^i B_l^i(0,0) \\ &= \sum_{i=1}^4 (B_l^i(0,0))^2 \\ &= D_2^j \end{aligned} \quad (\text{A.14})$$

Now place Jupiter in the center beam

$$B(0,0) = \sum_{i=1}^4 C_c^i B_c^i(0,0)$$

$$\begin{aligned}
&= 2 \sum_{i=1}^4 (B_c^i(0,0))^2 \\
&= D_3^j
\end{aligned} \tag{A.15}$$

If, as we would hope, $B_c^i \sim B_l^i \sim B_r^i$ for each i , then $D_3^j = 2D_2^j$. Thus, we chose to normalize the chopped beam profile such that the center beam centroid value is 1 and the side beam centroid values is 0.5 .

A.4 Formulae for Temperature Conversion

Using (A.12) and (A.13) with equation (A.9), we find

$$\Delta_2 T_{sky}^{rj} = \frac{D_2}{D_2^j} T_j \frac{\Omega_j B(0,0)}{\int d\Omega B(\theta, \phi)} \quad \text{where } B(0,0) = 0.5 \tag{A.16}$$

$$\Delta_3 T_{sky}^{rj} = \frac{D_3}{D_3^j} T_j \frac{\Omega_j B(0,0)}{\int d\Omega B(\theta, \phi)} \quad \text{where } B(0,0) = 1.0 \tag{A.17}$$

Notice that the normalization is at the centroid of the beam due to what was assumed about the location of Jupiter during the measurements. The value of $B(0,0)$ doesn't matter; only the ratio of the single difference chopped beam peak to the double difference chopped beam peak matters.

Taking this a step farther

$$\Delta_2 T_{sky}^{rj} = 2D_2 T_j \frac{\Omega_j}{\int d\Omega B^1(\theta, \phi)} \tag{A.18}$$

$$\Delta_3 T_{sky}^{rj} = D_3 T_j \frac{\Omega_j}{\int d\Omega B^1(\theta, \phi)} \tag{A.19}$$

where B^1 is the unchopped beam pattern normalized to one at the centroid.

These equations imply that when a signal of 1 Jupiter is in the center beam, the magnitude of the measured Rayleigh-Jeans temperature difference is the same as when 1 Jupiter appears in either the left or right beam. One can use $\int d\Omega B^1(\theta, \phi)$ to find an effective beamsize. The units of this integral are steradians since the units of B have been normalized away.

Appendix B

1992 Flight Timeline

Timeline of MSAM I 1992 Flight		
<i>Record</i>	<i>Event</i>	<i>Observation</i>
4540	start hold	Moon Raster (gains all 1)
4558	start raster	
4802	stop raster	
4820	end hold	
4896	start spin	Spin
4898	beginning of constant velocity	
4933	start changing gains to 1024	
4937	done changing gains to 1024	
4950	log claims spin data start	
5081	switch to inertial mode	
5183	start changing gains to 32	
5186	done changing gains to 32	
5342	stop spin	
5474	start scan	
5609	stop scan	
5946	start hold	Jupiter (gains all 32)
5960	start raster 1	
6204	stop raster 1	
6220	end hold	
6333	start scan	
6488	stop scan	

Timeline Continued ...		
<i>Record</i>	<i>Event</i>	<i>Observation</i>
6613	start hold	
6626	start raster 2	
6870	stop raster 2	
6895	end hold	
7483	start scan	CMBR Position 1
8032	stop scan	(gain 1,2 512; gain 3 128; gain 4 1024) (known as nominal)
8058	start scan	CMBR Position 2
8606	stop scan	
8632	start scan	CMBR Position 3
9244	stop scan	
9271	start scan with mistake	CMBR Position 4
9352	start good scan	
9875	stop scan	
9901	start scan	CMBR Position 5
10482	stop scan	
10509	start scan	CMBR Position 6
11123	stop scan	
11697	start scan	Coma Cluster1 (center)
11762	stop scan 1	
11766	start scan 2	(below)
11805	stop scan 2	
11827	start scan 3	(center)
11893	stop scan 3	
11895	start scan 4	(above)
11959	stop scan 4	
11962	start scan 5	(center)
12092	stop scan 5	

Timeline Continued ...		
<i>Record</i>	<i>Event</i>	<i>Observation</i>
12335	start scan	CMBR Position 7
12981	stop scan	
13007	start scan	CMBR Position 8
13620	stop scan	
13648	start scan	CMBR Position 9
14227	stop scan	
14254	start scan	CMBR Position 10
14867	stop scan	
14895	start scan	CMBR Position 11
15509	stop scan	
15536	start scan	CMBR Position 12
16117	stop scan	
16144	start scan	CMBR Position 13
16756	stop scan	
16783	start scan	CMBR Position 14
17387	stop scan	
17550	start hold	Saturn (gain 1,3,4 32; gain 2 512)
17572	start raster 1	
17815	stop raster 1	
17830	end hold	
17970	start hold	
17992	start raster 2	
18235	stop raster 2	
18250	end hold	
18415	start hold	
18438	start raster 3	
18680	stop raster 3	
18695	end hold	

Timeline Continued ...		
<i>Record</i>	<i>Event</i>	<i>Observation</i>
18705	start scan	
18935	stop scan	
19071	start scan	Elevation Scans
19251	stop scan	(Gains nominal)
19270	start spin	Sunrise Spin
19928	start shutter close	(gains nominal)
19934	shutter close	
19980	stop spin	
20029	start scan	Shutter closed scan
20675	start shutter open	(gains all at 1024)
20754	start scan	Sunlight Scans
20855	stop scan	(gains nominal)

Appendix C

Flight Statistics for MSAM I 1992

FILE CHARACTERISTICS

Total records 20959 or 11.6 hours of data.

Launch is at flight record number 1450 (+0/-10) or 05-Jun-92 00:59:26 UT (04-Jun-92 19:59:26 local).

Package shutdown occurred at 11:49:47 UT (05-Jun-92 6:49:47 local).

BALLOON/FLIGHT TRAIN INFO

Johnny-Mac claims that it is 330 feet from base of balloon to the Tim fitting, then another 4 feet from Tim fitting to the truck plate. I recall about 6 feet from the truck plate to the top of the gondola, and another 6 feet from the top of the gondola to the center of the main beam.

Net distance from the center of the beam to the base of the balloon is 346 feet (+/- a few feet).

Inflated dimension of the balloon is 348 ft high and 480 ft wide (from as-built spec sheet for Winzen (543)W39.96-3-11, model SF3-480.10-080-NSCH-04-ST S/N 11.

SUNSET/SUNRISE

Using 02:00 UT and 11:00 UT positions as approximate sunset and sunrise positions. GPS positions are used because they are available for the times involved, and because we would like to believe that they are 'more correct', even though the differences from the LORAN positions are not too significant (see GONDOLA POSITION section).

Sunset: 31d 39m N 95d 10m W 49Kft 05-Jun-92 01:47 (UT) Sunrise: 31d 55m N 100d 01m W 126Kft 05-Jun-92 10:56 (UT)

TIME REGISTRATION WITH UT

Archive record 1, frame 0 time: 00:11:07.65 (05-Jun-92) record 20959, frame 0 time: 11:49:44.42 (05-Jun-92)

To convert from records to UT, use:

$$UT = \text{RECORD}/1800.0 + 0.1850 \text{ (hours)}$$

To convert from UT to records, use:

$$\text{RECORD} = (\text{UT} - 0.1850) * 1800.0 \text{ (records)}$$

Appendix D

Correlation Coefficients for MSAM I Sensors

The correlation coefficients of the demodulated data, before and after drift subtraction is performed, are shown in the following contour plots. The shading is such that anti-correlated signals are white and correlated signals are black. The single difference *sd* and the double difference *dd* demodulated data are for channels 1 through 4 (*c1* through *c4*) are considered in each plot. The following sensor signals are considered:

TSTRONG: Strongback temperature

TSHLDR: Right ground shield temperature

TSHLDL: Left ground shield temperature

TSECMR: Temperature of right side of secondary mirror

TSECML: Temperature of left side of secondary mirror

TM0–TM9: Temperature sensors on primary mirror. TM0 is in the center. The others are arranged around the edge of the primary perimeter.

TMAVG: Average primary mirror temperature

M1X,M1Y,M1Z: Strongback-mounted magnetometers. M1X points along the telescope optical axis.

G1P,G2P,G1R,G2R: The two gondola-mounted gyroscopes (roll and pitch)

PLO: Pressure sensor

SPLO: Sensitive pressure sensor

INCLIN: Inclinometer mounted on strongback

ELENC,ELPOT: Strongback elevation monitors

XLPOS: Cross-elevation gyroscope signal

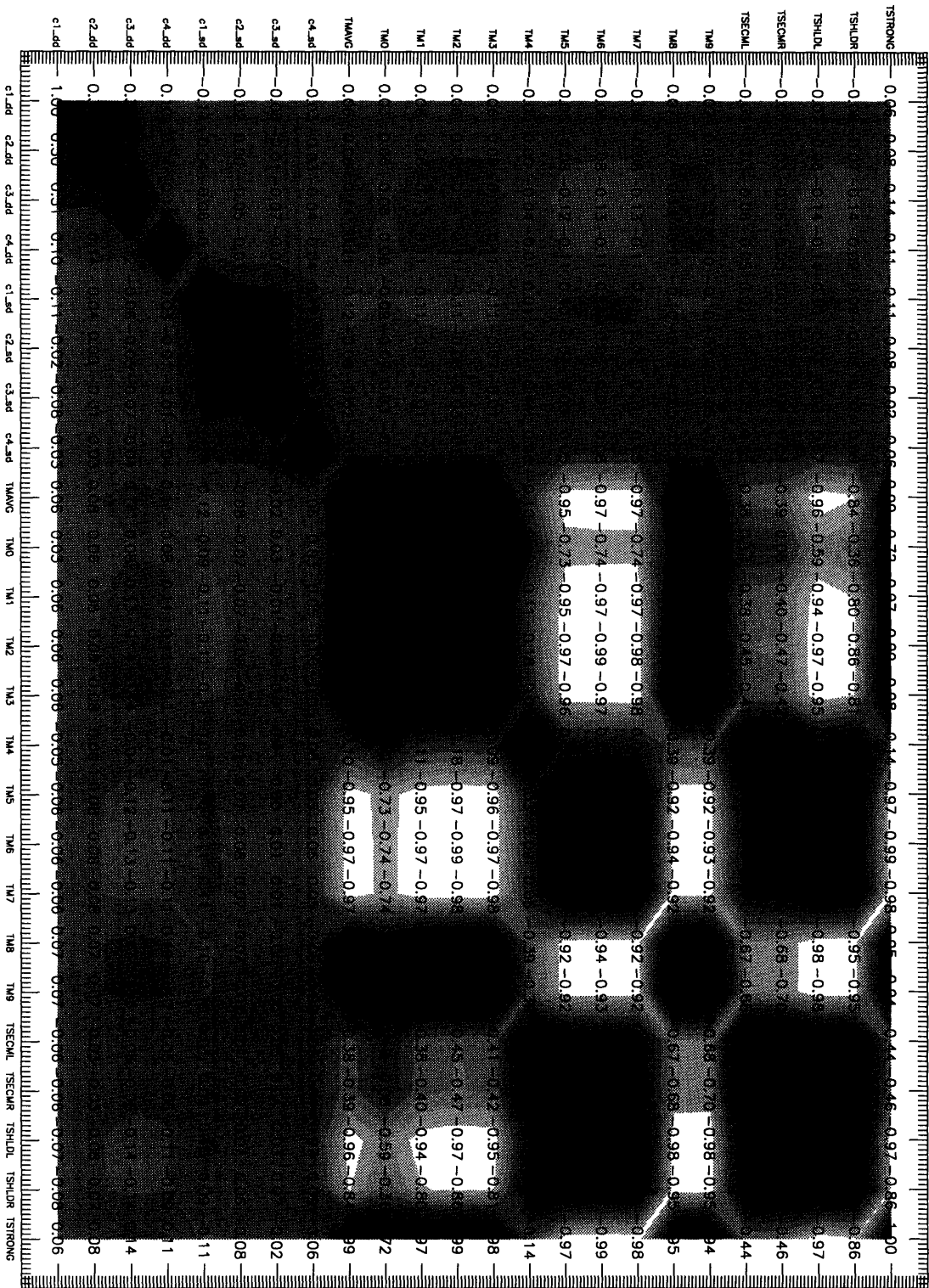
ELPOS: Elevation gyroscope signal

Correlation Coefficient for Temperature Sensors and Undecrypted Demodulated Data

	c1.d1d	c2.d1d	c3.d1d	c4.d1d	c1.s4d	c2.s4d	c3.s4d	c4.s4d	TMANG	TMO	TM1	TM2	TM3	TM4	TM5	TM6	TM7	TM8	TM9	TSECWL	TSECUR	TSHDLR	TSHDR	TSRONG
TSRONG	0.11	0.15	0.19	0.16	0.01	0.13	0.08	0.11	0.00	0.72	0.07	0.00	0.08	0.14	0.97	0.99	0.98	0.94	0.44	0.46	0.97	0.86	1.00	
TSHDR	0.17	0.17	0.28	0.18	0.01	0.14	0.12	0.12	-0.84	-0.36	-0.80	-0.86	-0.81	0.38	0.92	0.93	0.92	0.95	0.95	0.95	0.98	0.98	0.86	
TSHDLR	0.13	0.16	0.20	0.17	0.02	0.16	0.11	0.12	-0.96	-0.59	-0.94	-0.97	-0.95	0.39	0.92	0.93	0.92	0.95	0.95	0.98	0.98	0.97	0.86	
TSECUR	0.15	0.12	0.12	0.14	0.09	0.14	0.16	0.16	-0.38	0.04	-0.48	-0.47	-0.42	0.38	0.92	0.93	0.92	0.95	0.95	0.98	0.98	0.97	0.86	
TSECWL	0.13	0.12	0.12	0.14	0.09	0.13	0.19	0.12	-0.38	0.13	-0.28	-0.45	-0.41	0.38	0.92	0.93	0.92	0.95	0.95	0.98	0.98	0.97	0.86	
TMO	0.19	0.17	0.19	0.17	0.03	0.15	0.11	0.11	-0.84	-0.36	-0.80	-0.86	-0.81	0.38	0.92	0.93	0.92	0.95	0.95	0.98	0.98	0.97	0.86	
TM9	0.16	0.12	0.09	0.16	-0.02	0.15	-0.19	-0.11	-0.39	-0.92	-0.94	-0.92	-0.92	0.39	0.92	0.94	0.92	0.95	0.95	0.98	0.98	0.97	0.86	
TM7	0.09	0.14	0.16	0.15	0.02	0.13	0.07	0.09	-0.97	-0.74	-0.97	-0.98	-0.98	0.39	0.92	0.93	0.92	0.95	0.95	0.98	0.98	0.97	0.86	
TM6	0.10	0.14	0.16	0.16	0.01	0.13	0.02	0.09	-0.97	-0.74	-0.97	-0.99	-0.97	0.39	0.92	0.93	0.92	0.95	0.95	0.98	0.98	0.97	0.86	
TM5	0.09	0.13	0.13	0.16	0.03	0.14	0.09	0.10	-0.95	-0.73	-0.95	-0.97	-0.96	0.39	0.92	0.93	0.92	0.95	0.95	0.98	0.98	0.97	0.86	
TM4	0.17	0.10	0.12	0.09	0.07	0.07	0.02	0.00	-0.91	-0.16	-0.95	-0.96	-0.96	0.39	0.92	0.93	0.92	0.95	0.95	0.98	0.98	0.97	0.86	
TM3	0.07	0.13	0.13	0.16	0.02	0.12	-0.07	-0.11	-0.99	-0.96	-0.97	-0.97	-0.97	0.39	0.92	0.93	0.92	0.95	0.95	0.98	0.98	0.97	0.86	
TM2	0.11	0.13	0.14	0.16	0.01	0.14	-0.07	-0.16	-0.99	-0.96	-0.97	-0.97	-0.97	0.39	0.92	0.93	0.92	0.95	0.95	0.98	0.98	0.97	0.86	
TM1	0.07	0.12	0.13	0.14	0.02	0.13	-0.07	-0.05	-0.99	-0.96	-0.97	-0.97	-0.97	0.39	0.92	0.93	0.92	0.95	0.95	0.98	0.98	0.97	0.86	
TMO	0.05	0.07	0.07	0.14	0.09	-0.07	-0.02	0.00	-0.99	-0.96	-0.97	-0.97	-0.97	0.39	0.92	0.93	0.92	0.95	0.95	0.98	0.98	0.97	0.86	
TMANG	0.06	0.14	0.21	0.15	0.01	0.13	0.08	0.11	-0.99	-0.96	-0.97	-0.97	-0.97	0.39	0.92	0.93	0.92	0.95	0.95	0.98	0.98	0.97	0.86	
c4.s4d	0.17	0.02	0.02	0.04	0.25	0.01	0.00	0.11	-0.03	0.08	-0.10	0.00	0.10	0.09	0.09	0.11	0.11	0.11	0.11	0.11	0.11	0.11	0.11	
c3.s4d	0.08	0.06	0.08	-0.03	0.00	0.00	0.00	-0.08	-0.02	-0.07	-0.07	0.02	0.02	0.02	0.02	0.02	0.02	0.02	0.02	0.02	0.02	0.02	0.02	
c2.s4d	0.11	0.05	0.09	-0.01	0.00	0.00	0.00	-0.13	-0.02	-0.13	-0.14	-0.12	0.07	0.14	0.13	0.13	0.13	0.13	0.13	0.13	0.13	0.13	0.13	
c1.s4d	0.20	0.05	0.13	0.00	0.00	0.00	0.00	0.07	0.00	0.02	0.01	0.02	0.07	0.00	0.00	0.02	0.02	0.02	0.02	0.02	0.02	0.02	0.02	
c4.d1d	0.18	0.02	0.02	0.03	0.10	0.03	0.15	0.11	0.14	0.16	0.14	0.09	0.16	0.16	0.16	0.16	0.16	0.16	0.16	0.16	0.16	0.16	0.16	
c3.d1d	0.22	0.01	0.01	0.01	0.01	0.02	0.21	0.07	0.18	0.19	0.19	0.19	0.19	0.19	0.19	0.19	0.19	0.19	0.19	0.19	0.19	0.19	0.19	
c2.d1d	0.14	0.01	0.01	0.02	0.06	0.00	0.02	0.14	0.07	0.12	0.15	0.15	0.10	0.13	0.14	0.14	0.14	0.14	0.14	0.14	0.14	0.14	0.14	
c1.d1d	1.00	0.40	0.29	0.10	0.20	0.11	0.08	0.07	0.09	0.03	0.07	0.11	0.07	0.07	0.09	0.10	0.09	0.10	0.10	0.10	0.10	0.10	0.10	

White = anti-correlated ; Black = correlated

Correlation Coefficients for Temperature Sensors and Dedicated Demodulated Data



White = anti-correlated ; Black = correlated

Correlation Coefficient for Other Sensors and the Demodulated Data



White = anti-correlated ; Black = correlated

Correlation Coefficient for Other Sensors and the Detrited Demodulated Data



White = anti-correlated ; Black = correlated

Bibliography

- [1] T.W. Anderson. *An Introduction to Multivariate Statistical Analysis*. John Wiley and Sons, New York, second edition, 1984.
- [2] W.J. Barnes. *A Model of Galactic Dust and Gas from FIRAS*. PhD dissertation, Massachusetts Institute of Technology, 1994.
- [3] C. Bennett et al. *ApJ Letters*, 396:L7, 1992.
- [4] J.O. Berger. *Statistical Decision Theory and Bayesian Analysis*. Springer-Verlag, New York, 1985.
- [5] P.R. Bevington. *Data Reduction and Error Analysis for the Physical Sciences*. McGraw-Hill Book Company, New York, second edition, 1969.
- [6] F. Boulanger and M. Perault. *ApJ*, 330:964, 1988.
- [7] Charakhch'yan et al. *Cosmic Rays in the Stratosphere and in Near Space during Solar Activity Cycles 19 and 20*. Consultants Bureau, New York, 1978.
- [8] E. S. Cheng et al. A measurement of the medium-scale anisotropy in the cosmic microwave background radiation. *ApJ Letters*, 422:L37, 1994. MSAM I (1992).
- [9] E. S. Cheng, S. S. Meyer, and L. A. Page. A high capacity 0.024k ³he refrigerator for balloon-borne observations. *In preparation*.
- [10] L.M. Chernin and D. Scott. Bima observations of possible microwave background source. *Astronomy and Astrophysics*, Submitted.
- [11] S.E. Church et al. An arcminute resolution search at 4.7cm^{-1} for point sources in msam and max fields. *ApJ Letters*, Submitted 1994.
- [12] A. Clapp et al. *ApJ Letters*, submitted 1994. MAX4.
- [13] D. Cottingham. *A Sky Temperature Survey at 19.2 GHz Using a Balloon Borne Dicke Radiometer for Anisotropy Tests of the Cosmic Microwave Background Radiation*. PhD dissertation, Princeton University, 1987.
- [14] P. de Bernardis et al. *ApJ Letters*, 422:L33, 1994. ARGO.
- [15] M. Devlin et al. *ApJ Letters*, submitted 1994. MAX4.

- [16] P.M. Downey, A.D. Jeffries, S.S. Meyer, R. Weiss, F.J. Bachner, J.P. Donnelly, W.T. Lindy, R.W. Mountain, and D.J. Silversmith. *App. Opt.*, 23(6):910, 1984.
- [17] P.. Dragovan et al. *ApJ Letters*, submitted 1994. PYTHON.
- [18] T. Gaier et al. *ApJ Letters*, 398:L1, 1992. SP91.
- [19] M.J. Griffin and P.A.D. Ade. Submillimeter and millimeter observations of jupiter. *Icarus*, 65:244–256, 1986.
- [20] J. Gunderson et al. *ApJ Letters*, 413:L1, 1993. MAX3.
- [21] S. Hancock et al. *Nature*, In press, 1994. Tenerife.
- [22] T. Herbig et al. *Bull. Am. Aston.*, 24:421, 1992.
- [23] R.H. Hildebrand et al. Far-infrared and submillimeter brightness temperatures of the giant planets. *Icarus*, 64:64–87, 1985.
- [24] G. Hinshaw et al. Simulated cmb maps at 0.5° resolution: Basic results. *ApJ Letters*, accepted 1995.
- [25] C.J. Hogan. *ApJ Letters*, 284:L1, 1984.
- [26] P. Horowitz and W. Hill. *The Art of Electronics*. Cambridge University Press, New York, second edition, 1990.
- [27] W. Hu and N. Sugiyama. *CfPA preprint; submitted to Phys. Rev. D*, 94-th-55, 1994.
- [28] A. Kogut et al. Simulated cmb maps at 0.5° resolution: Unresolved features. *ApJ Letters*, accepted 1995.
- [29] M. Kowitt et al. A detection of unresolved features in the microwave background. *In Preparation*, 1995.
- [30] D. Lancaster. *Active Filter Cookbook*. Howard W. Sams and Co., Indianapolis, 1979.
- [31] B.R. Martin. *Statistics for Physicists*. Academic, London, 1971.
- [32] J.C. Mather et al. *ApJ*, 420:439, 1994.
- [33] P. Meinhold et al. *ApJ Letters*, 409:L1, 1993. MAX3.
- [34] S. S. Meyer, E. S. Cheng, and L. A. Page. A different title. *ApJ Letters*, 371:L7, 1991.
- [35] Denise E. Miller. *NSBF User's Manual*. National Scientific Balloon Facility, Palestine, Tx, 1985.
- [36] L.A. Page. *A Measurement of the Cosmic Microwave Background Radiation Anisotropy*. PhD dissertation, Massachusetts Institute of Technology, 1989.

- [37] L.A. Page, E.S. Cheng, and S.S. Meyer. *ApJ Letters*, 355:L1, 1990.
- [38] Piccirillo et al. *Infrared Physics*, 27:215, 1987.
- [39] L. Piccirillo and P. Calisse. *ApJ*, 411:529, 1993. IAB.
- [40] W.H. Press et al. *Numerical Recipes: The Art of Scientific Computing*. Cambridge University, Cambridge, 1986.
- [41] A.C.S. Readhead et al. *ApJ Letters*, 346:L56, 1989. Owens Valley.
- [42] R.K. Sachs and A.M. Wolfe. *ApJ*, 147:73, 1967.
- [43] J. Schuster et al. *ApJ Letters*, 412:L47, 1993. SP91.
- [44] J. Silk. *Ap.J.*, 151:459, 1968.
- [45] G. Smoot et al. *ApJ Letters*, 396:L1, 1992.
- [46] P. Steinhardt. *Proceedings of the 1994 Snowmass Summer Study*, 1994.
- [47] M.U. SubbRao et al. *ApJ*, In press, 1994.
- [48] R.A. Sunyaev and Ya.B. Zel'dovich. *Astrophys. Sp. Sci.*, 7:1, 1970.
- [49] R.A. Sunyaev and Ya.B. Zel'dovich. *ARAA*, 18:537, 1980.
- [50] Tsao et al. Cosmic ray effects on microelectronics, part iii: Propagation of cosmic rays in the atmosphere. *NRL-MR-5402*, 1984.
- [51] G.S. Tucker et al. *ApJ Letters*, 419:L45, 1993. White Dish.
- [52] S. Wheelock et al. *IRAS Sky Survey Atlas, $|\beta| > 50$ degrees, Explanatory Booklet*. JPL, Pasadena, 1991.
- [53] S. Wheelock et al. *Explanatory Supplement to the IRAS Sky Survey Atlas*. JPL, Pasadena, 1994.
- [54] M. White et al. Anisotropies in the cosmic microwave background. *CfPA preprint*, 93-th-35, 1993.
- [55] M. White and D. Scott. Quoting experimental information. *CfPA preprint*, 94-th-28, 1994.
- [56] E.J. Wollock et al. Don't know. *ApJ Letters*, 419:L49, 1993. Big Plate.
- [57] E.L. Wright et al. *ApJ*, 381:200, 1991.